Scalable Micro/Nanostructured Surfaces for Thin-Film Condensation Heat Transfer Enhancement in Steam Power Plants

by

Yajing Zhao

S.M., Mechanical Engineering (2018)
Massachusetts Institute of Technology
B.E., Energy and Power Engineering (2016)
Xi'an Jiaotong University, China

Submitted to the Department of Mechanical Engineering in
Partial Fulfillment of the Requirements for the Degree of
Doctor of Philosophy in Mechanical Engineering
at the
Massachusetts Institute of Technology
September 2022

Signature of Author:……..
Department of Mechanical Engineering
Aug 31, 2022

Certified by:……...
Evelyn N. Wang
Ford Professor of Engineering and Department Head
Thesis Supervisor

Accepted by:……..
Nicolas Hadjiconstantinou
Professor of Mechanical Engineering
Chairman, Department Committee on Graduate Theses

Intentionally blank page

Scalable Micro/Nanostructured Surfaces for Thin-Film Condensation Heat Transfer Enhancement in Steam Power Plants

by

Yajing Zhao

Submitted to the Department of Mechanical Engineering on Aug 31st, 2022,

in Partial Fulfillment of the Requirements for the Degree of Doctor of Philosophy

Abstract

Steam power plants, which contribute to over 50% of energy production globally, rely on condensers to control system-level energy efficiency. Due to the high surface energy of common heat exchanger materials, the vapor condenses by forming a continuous liquid film with low thermal conductivity (filmwise condensation), hindering heat transfer from the vapor side to the condenser surface. Hydrophobic surfaces achieved by either chemical methods (e.g., coating treatment) or physical methods (e.g. structures design) have shown great promise in enhancing condensation heat transfer by promoting dropwise condensation. However, the short lifetime and high fabrication cost of most of these hydrophobic surfaces remain a challenge for long-term and large-scale industrial applications. A promising solution to enhancing condensation heat transfer in a robust and scalable manner is to control the thickness and thermal conductivity of the condensate film, which we term thin-film condensation. This can be achieved by sandwiching a thin layer of porous metal wick between a hydrophobic membrane and the condenser surface to confine the condensed liquid, forming a thin liquid-metal composite film that significantly improves the effective thermal conductivity of the condensate-filled porous media.

In this work, we designed, fabricated, tested, and demonstrated thin-film condensation heat transfer using commercially available materials and scalable approaches. First, we proved the concept using biphilic, microchannel-assisted hierarchical copper surfaces made of commercially available copper foams and copper meshes. Condensation heat transfer on the hierarchical copper surfaces was characterized to be up to 2x as compared to the conventional filmwise condensation, even with flooding on the surface due to the defects on the mesh and the coating. Then, we investigated electrospinning as a potential approach to customize hydrophobic membranes for the thin-film condenser surfaces. The key benefit of the hydrophobic membrane in the surface design is to generate capillary pressure through micro/nanoscale pores, which acts as the driving force for the condensate flow in the metal wick. We conducted a parametric study on the effects of several key fabrication parameters on the pore size of the electrospun membrane, with the help of the fractional factorial design. Solution feeding rate was found to be the most impactful parameter on the membrane pore size and should be considered the most during membrane optimization. A heat and mass transfer model was developed to predict the heat transfer performance of the thin-film condenser surfaces made of electrospun membranes and porous copper wicks. Upon careful design of the surface structures, an over 5x heat transfer enhancement is expected on these thin-film condensers, which is comparable to the state-of-the-

art dropwise condensation. Finally, a techno-economic analysis was conducted on the thin-film condensers. The result shows that the additional material for the condenser tube modification costs less than 10% of the condenser cost. However, with the expected 5x steam-side condensation heat transfer performance, thin-film condensers will be able to increase power plants' output by 2-6%, which is equivalent to over $10B of the value proposition for steam power plants across the globe.

Thesis Committee:

Professor Evelyn N. Wang (Thesis Advisor/Chair), Department of Mechanical Engineering

Professor Rohit Karnik, Department of Mechanical Engineering

Professor John H. Lienhard V, Department of Mechanical Engineering

Professor Borivoje Mikic, Department of Mechanical Engineering

Acknowledgements

I am extremely honored to have Evelyn as my advisor. She is a role model for me as a woman in STEM, and she is the reason I came to MIT back in 2016. I thank her for giving me the chance to work with her, and the encouragement and patience she gave me when I was struggling for months if not years to get my chamber to work. Resilience is the best thing that I have ever learned in grad school through her. I am still not resilient enough in front of challenges, but I know I have grown much stronger through my chamber experience. I also thank Evelyn for her tremendous support for my PhD research and my career development. No matter how busy she gets, she is always responsive and just one email away. This thesis would not be possible without Evelyn's guidance and support during the past six years.

My thanks also go to my committee members: Prof. Karnik, Prof. Lienhard, and Prof. Mikic. My thesis would not be complete without their guidance and input along the way. I would also like to thank the following people and organizations who provided me with essential facilities that I used in the completion of this thesis: Kurt and Jorg at MIT Nano, Shaymus at CMSE METLab, Patrick at MIT MRSEC, Adam at Harvard CNS, Nicole at MIT ISN, and Prof. Rutledge in the department of Chemical Engineering.

It is people that make MIT a magical place. I am incredibly blessed to be part of this incredible community and to get to know every single person I came across in the past six years. I would like to thank my wonderful labmates at the DRL. I am deeply grateful for having Dr. Daniel Preston as my mentor during my early days in DRL. Dan took me under his wings and immersed me into the U.S. culture and environment from Day 1. He is the best mentor I have ever seen, and all my mentorship skills were passed onto me from his daily interactions with me. My thanks also go to Dr. Kyle Wilke and Dr. Solomon Adera, who mentored me along the way towards the later stage of my PhD. I would like to thank my other colleagues and friends in the DRL as well: Yangying, Dion, Lin, David, Elise, Jay, Arny, Colin, Youngsup, Lenan, Samuel, Geoff, Hyeongyun, Carlos, Bachir, Xiangyu, …this list gets very long when I have spent 6+ years in the lab! Additionally, my UROPs are amazingly smart, hardworking, and supportive. I appreciate the experience of working with them and I wish them success in whatever future adventure they choose. There are certainly people outside of my research lab that are equally important to me and make my graduate journey colorful: my 3-year-long roommate Qian, my friends from MEGAWomen, labmates from the RK lab, and teammates and mentors from various entrepreneurial programs.

Last but not least, my deepest acknowledgment goes to my family. I thank my mom and dad for allowing me to follow my heart and pursue whatever way I am passionate about, even if this means that I as the only child could be far away from them for years. COVID has made the trip back home extremely hard, but my heart is never far. I would also like to thank Popo and Rifle for going through ups and downs with me during my PhD journey, especially the last year of it when things piled up crazily.

Time is never enough. Research seems to never end. I always wish that I can do better in time management, but I have always been chased by deadlines. Struggling with 2.25 seems to be just yesterday, but now I cannot believe that I am at the finishing line of the PhD journey, certainly with more unknowns, struggles, and lessons to come. People say that getting an education from MIT is like to take a drink from the firehose. I will always deeply appreciate and miss this firehose experience at MIT, and be fearless to embrace future adventures.

Intentionally blank page

Table of Contents

Intentionally blank page

List of Figures

Intentionally blank page

1. Introduction and Background

1.1 Motivation

Global energy demand is expected to increase about 50% over the next 30 years, driven by population and economic growth[1]. Energy production has to keep up with the growing energy demand in both the short term and the long run. Right now, the majority of the global energy is produced by thermal power plants, mostly steam cycles, where water is used as the working fluid to absorb heat from various types of heat sources (e.g., fossil fuels, geothermal, nuclear, waste heat, solar thermal, etc.) and convert that heat to electricity through a turbine. In the United States, over 80% of energy production is currently contributed by thermal power plants, among which roughly three quarters are driven by steam cycles[2]. Despite being the major contributor to energy production, thermal power plants account for the largest amount (40% share) of fresh water withdrawls[3] and one of the largest source (25% share) of greenhouse gas (GHG) pollution[4] in the United States.

With demands for electrification, water saving, and reduced GHG emissions colliding, the world needs more efficient steam power plants. The energy efficiency of steam power plants is determined by thermodynamics. Figure 1 shows a diagram for the Rankine cycle, which is the typical thermodynamic cycle of a steam power plant. Upon heat exchange with the heat source through the boiler, water vaporizes into a high temperature and high-pressure vapor flow, which then enters the turbine to generate power. The exhaust vapor coming out of the turbine is cooled down to the liquid phase by a condenser and pumped back to the boiler to complete the cycle.

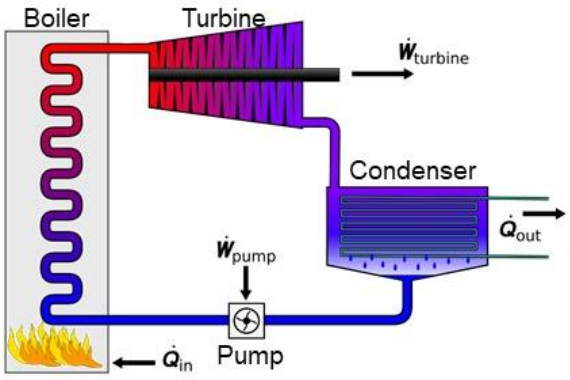

Figure 1: Thermodynamic cycle of a steam power plant.

Thermodynamically, condensers hold the key to improving power plant efficiency. The energy efficiency of a steam power plant is determined by the temperature difference between

the hot side T_{H} (boiler) and the cold side T_{C} (condenser), with a theoretical limit given by the Carnot efficiency $\eta_{\mathrm{Carnot}} = 1 - \frac{T_{\mathrm{C}}}{T_{\mathrm{H}}}$. It is generally difficult to increase the hot side temperature due to limitations on the materials (e.g., materials for boilers or turbines in high-temperature natural gas power plants) or the heat source temperature (e.g., the temperature of geothermal fluids or waste heat). In contrast, lowering the cold side temperature by having a more efficient condenser is more approachable, and can significantly enhance energy efficiency. Figure 2 shows the effect of condenser terminal temperature difference (TTD) on the system level efficiency, water consumption, and CO_2 emission of a steam power plant. TTD is defined as the temperature difference between the turbine exhaust vapor temperature and the condenser cooling water outlet temperature. With a more efficient condenser, turbine exhaust vapor temperature will be lower and the TTD will become smaller. Figure 2 shows that, as the condenser TTD drops about 17°C, the system efficiency will increase roughly 2%, with a reduction in the water consumption rate of roughly 35 gal/MWh and a reduction in the CO2 emission of 16 kg/MWh.

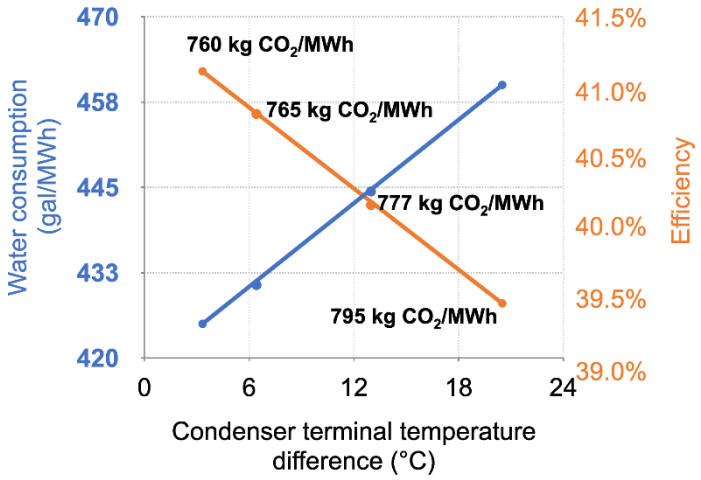

Figure 2: The effect of condenser terminal temperature difference on the system level efficiency, water consumption, and CO_2 emission of steam power plants[5].

Numerous surface coatings and structures have been developed to enhance condensation heat transfer of steam over the past century. However, most of these surfaces are limited to lab-scale prototype and rarely applied to industrial condensers. Here, we introduce state of the art surface engineering for condensation heat transfer and the key challenges remained in this field that this thesis is aiming to address.

1.2 State of the Art Research in Condensation Heat Transfer

1.2.1 Dropwise Condensation

A milestone in the long-term exploration of condensation heat transfer enhancement is the discovery of dropwise condensation[6]. In dropwise mode, the condensed water stays as discrete drops on the cold condenser surface, grows up to a critical size near the capillary length (~2.7mm for water), and finally sweeps off the surface. In this way, the drops keep refreshing the cold surface and continuously creating bare surfaces for vapor to condense on. Therefore, the dropwise mode has a much lower thermal resistance compared to the conventional filmwise mode where the cold surface is covered with a thermal barrier of the water film. As a result, dropwise condensation has been demonstrated to exhibit up to an order of magnitude higher heat transfer efficiency as compared with filmwise condensation[7], as shown by the experimental data summarized in Figure 3.

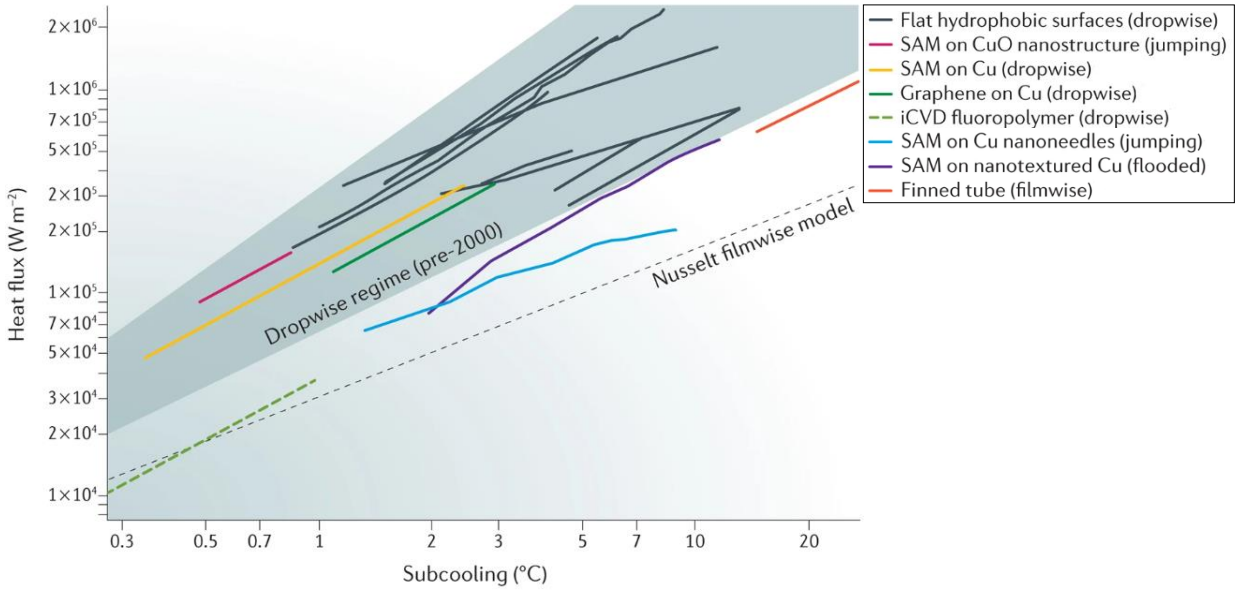

Figure 3: Recent development in surface engineering for condensation heat transfer enhancement. Dropwise condensation has shown up to an order of magnitude higher heat transfer performance as compared to the conventional filmwise condensation[8].

Surface hydrophobicity, a property that enables surfaces to repel water with a contact angle beyond 90°, has been widely applied for promoting dropwise condensation. Self-assembled monolayers (SAM)[9-15] and thin-film of polymer coatings[16-22] have been frequently used as a chemical treatment technique to achieve surface hydrophobicity and promote dropwise condensation. These SAM and polymeric coatings are composed of thermally insulating

materials and as a result, have to be ultra-thin (≪1 μm). However, at this thickness limit, these SAM and thin polymer coatings typically degrade within days if not hours during condensation of water vapor[8,23-27], which prevents them from being applied in industrial settings. Figure 4 gives an example of the degradation of dropwise condenser coating over time: heat transfer performance of the hydrophobic coated surface drops to a similar level as filmwise condensation after 6 days of condensation.

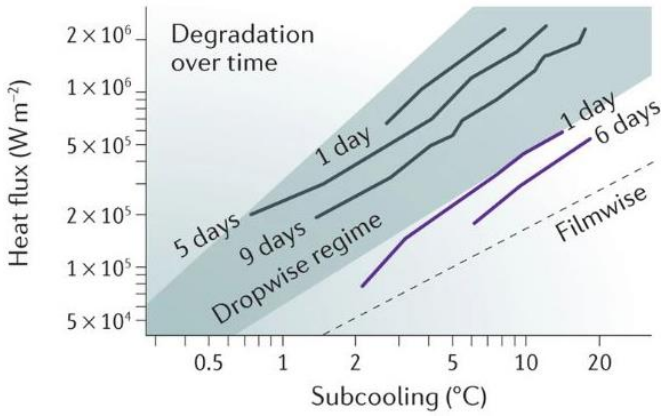

Figure 4: Dropwise-condenser coatings degrade over time[8].

Micro/Nanoscale surface structures have been incorporated with surface hydrophobicity to achieve superhydrophobic surfaces, on which "jumping droplet" was observed and as a result of enhanced droplet mobility, further heat transfer enhancement as compared to dropwise condensation on hydrophobic surfaces was demonstrated[28-34]. However, these surfaces could only sustain the exceptional heat transfer performance under relatively low surface subcooling; under high surface subcooling, flooding would occur and instead of jumping, droplets would pin on the surface, significantly degrading heat transfer performance[35-38]. Furthermore, most of these superhydrophobic surfaces rely on non-robust coatings, which suffer from a short lifetime in the pure vapor environment and would not survive in industrial condensers for more than a week.

Plasma treatment[39], initiated chemical vapor deposition (iCVD) [40], and fluorine−carbon based lipid-like coating-substrate interface[41] have shown great promise to improve the robustness of hydrophobic coatings, but the feasibility and cost-effectiveness of applying these techniques to large-scale condenser surfaces are yet to be demonstrated. Recent studies demonstrated that dropwise condensation could be achieved on hydrophilic surfaces without any hydrophobic coatings in cases where the contact angle hysteresis of the surface becomes substantially low

(<3°)[42,43]. However, achieving such a low contact angle hysteresis on a large-scale condenser surface remains challenging.

Re-entrant surfaces and double re-entrant surfaces have been recently demonstrated to achieve water repellency on intrinsically hydrophilic materials with a careful design of surface structures[44-50]. These surfaces eliminate the dependency on hydrophobic coatings, providing a durable solution to achieve surface hydrophobicity. However, in order to realize dropwise condensation, the characteristic pitch of these re-entrant structures needs to be smaller than the spacing of the condensate nucleation sites, which can be on the order of hundreds of nanometers[51,52]. Dropwise condensation on re-entrant surfaces has been successfully demonstrated on a re-entrant surface consisting of isolated reentrant cavities with a pitch on the order of 100 nm [53]. However, these delicate structures are costly to fabricate and hard to scale up.

Lubricant infused surfaces (LIS)[54-60], where low surface tension lubricants are embedded into micro/nanostructured substrates to enable ultra-low contact angle hysteresis and therefore formation and removal of water droplets, have been studied extensively to promote dropwise condensation as an alternative to hydrophobic coatings. However, lubricant drainage[61-66] remains a concern that inhibits the application of LIS in the high-purity water environment in steam power plants. As a similar idea to LIS, polymer-infused porous surfaces (PIPS)[67-69] were recently proposed as another strategy to achieve dropwise condensation in a robust manner. In PIPS, a porous metal network is used to enhance the effective thermal conductivity of the polymer coating and as to help hold the polymer coating in place, enabling heat transfer enhancement as well as coating longevity. However, the thickness of the polymer coating on PIPS needs to be carefully controlled in order to avoid being insulating while in the meantime ensuring low enough contact angle hysteresis on the surface to avoid droplet pinning. To date, PIPS has been proven at lab scale to improve the condensation heat transfer of steam to over 750% as compared to filmwise condensation[67], but its application to large-scale condensers has yet to be demonstrated.

1.2.2 Thin-film Condensation

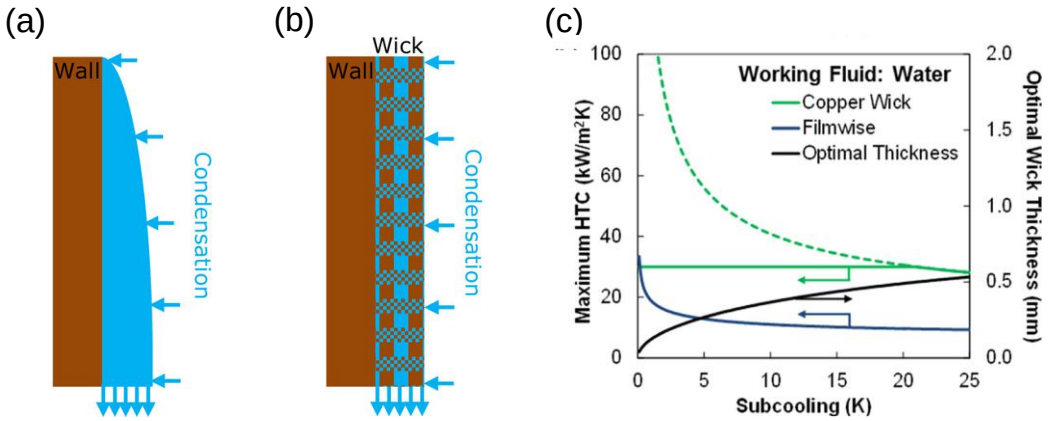

Figure 5: Wicking condensation vs, filmwise condensation[70]. (a): During filmwise condensation, water condensed onto the flat hydrophilic surface in the format of a liquid film with thickness increasing in the direction of gravity. (b) During wicking condensation, water condensed into the pores of the metal wick substrate, forming a thermally conductive water-metal composite film with water drainage in the direction of gravity. (c) Projected maximum heat transfer coefficient on a wicking condensation surface with a characteristic pore size of 0.5 mm.

A completely different concept, termed wicking condensation[70,71], was proposed to enhance condensation heat transfer in the format of filmwise, eliminating the need for hydrophobic coating or lubricant. In wicking condensation, the condenser surface is decorated with a highly permeable, highly thermally conductive porous metal wick that serves as the condensing surface. When the vapor condenses onto the wicking condenser surface, it fills into the pores of the metal wick due to surface hydrophilicity, and drains out of the wick under the gravity force, as shown in the schematic in Figure 5 (b). As compared to the conventional filmwise condensation on a flat hydrophilic surface as shown in Figure 5 (a), the liquid film formed during wicking condensation has a higher effective thermal conductivity due to the existence of the metal wick and therefore can generate more efficient heat transfer. One caveat, particularly in the case of water condensation, is that wicking condenser surfaces can flood, in which case the gravitational pressure becomes insufficient to drive fluid flow throughout the wick, resulting in some of the fluid exiting the front surface of the wick and forming a falling fluid film on the surface of the combined wick–condensate composite, thereby degrading heat transfer performance. An optimal wick thickness can be derived from the force balance between the gravitational driving force and the viscous pressure loss of the fluid flowing through the wick, at which point flooding is imminent. This optimal thickness increases with the surface

subcooling, reducing heat transfer enhancement at high subcooling. However, this thickness cannot be infinitely small and is limited by the characteristic length of the wick (i.e., pore size). As a result, only marginal heat transfer enhancement can be achieved at subcooling higher than 5°C, as shown in Figure 5 (c).

Capillary-enhanced wicking condensation has been proposed and modeled in a previous study where an external pump is used in wicking condenser surfaces to provide a capillary driving force to assist with condensate flow[72]. However, the pump consumes extra energy and the implementation of the pump with appropriate pumping force at the exit port of the wick structure is non-trivial.

Hydrophobic pores provide a solution to generate capillary pressure in a passive way. Several recent studies have explored the use of hydrophobic porous structures for capillary-driven thin film condensation, where a hydrophobic porous top layer is generating a capillary pressure that can hold the condensed liquid film within a controlled thickness until a certain amount of surface subcooling. Wen *et al*.[73] experimentally demonstrated film-to-droplet sucking flow condensation on a hydrophobic hierarchical copper mesh with an enhanced condensation heat transfer that is even superior to dropwise condensation over a wide range of surface subcooling. On such a hydrophobic hierarchical copper surface (as shown in Figure 6(a)-(b)), water droplets coalesced and filled into the porous copper mesh layer, and eventually came out of the mesh pore in the format of mobile droplets following the film-to-droplet sucking flow driven by capillary pressure. Despite the exiting droplets, the whole surface maintained a thin film of water-copper composite, which contributed to the enhanced heat transfer. With a similar concept, Oh *et al*. demonstrated thin-film condensation on a biphilic nickel inverse opal surface[74] (as shown in Figure 6(c)-(d)). Condensed water was constrained within the thin layer of nickel inverse opals under the capillary pressure generated by the hydrophobic layer and filmwise condensation was confined to thicknesses <10 μm was demonstrated with a predicted heat transfer coefficient of 50 kW/m^2K, which is comparable to dropwise condensation.

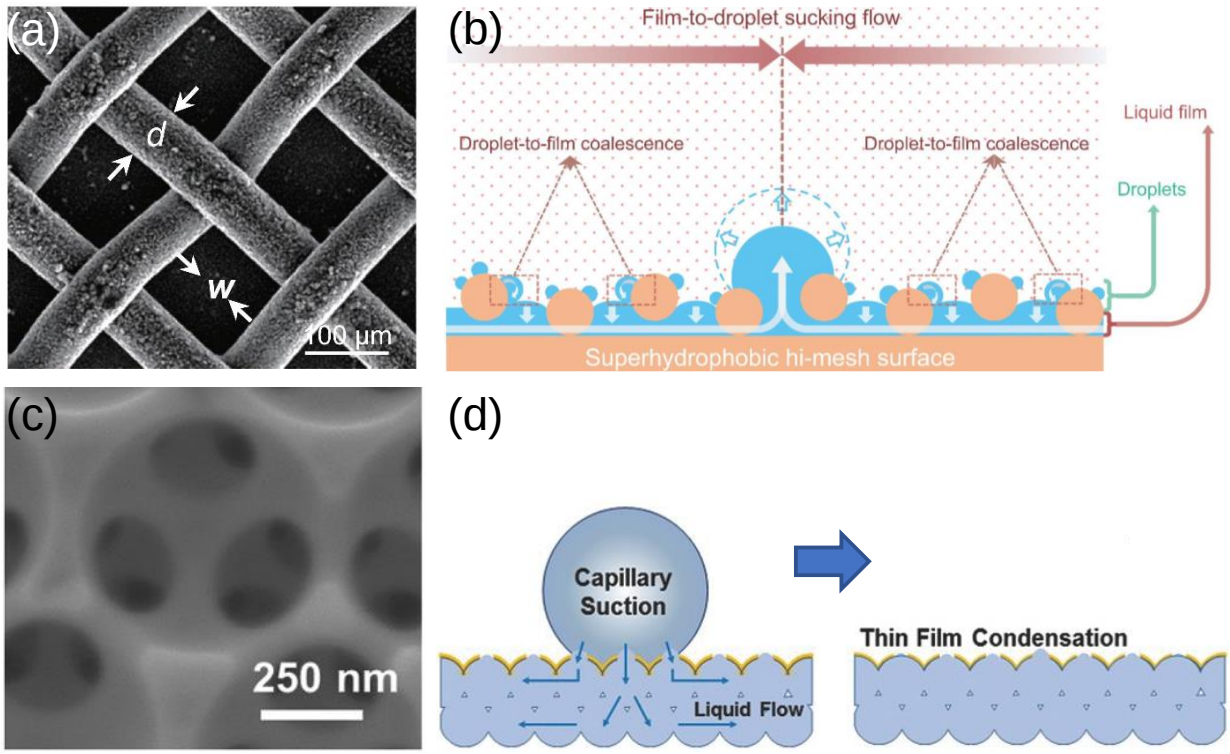

Figure 6: Hydrophobic porous structures for capillary-enhanced thin-film condensation. (a) and (b)[73]: Hierarchical copper mesh coated with hydrophobic coating shows sucking-flow condensation where the condensed droplets coalesce into the condensate film, maintaining a thin film until being sucked by a draining droplet coming out of the mesh pore. (c) and (d)[74]: a porous biphilic nanostructure made of nickel inverse opals (NIO) and a thin (<20 nm) hydrophobic top layer coating shows thin-film condensation, where condensed water is maintained within the NIO by capillary pressure.

Other biphilic structures such as micropillar arrays with PTFE coatings on the top[75] and an anodic aluminum oxide (AAO) membrane with a hydrophobized top layer have been fabricated to explore capillary-driven thin-film condensation[76], as shown in Figure 7(a) and (c), respectively. Under an environmental scanning electron microscope (ESEM), condensed water film was observed to form beneath the hydrophobic PTFE-coated top layer, as shown in Figure 7(b)[75]. Continuous condensation caused the liquid film to eventually flooded onto the top of the PTFE coating layer through local bursting sites, while the rest of the condensing surface maintained a thin film. Liu *et al*. modified an AAO membrane with a top layer of hydrophobic coating, as shown in the schematic in Figure 7(c)[76]. In a humid-air environment, this biphilic AAO membrane was able to absorb condensed water into the hydrophilic bottom layer, achieving "dry" surface atop the hydrophobic layer, as shown in the circle area in Figure 7(d)[76].

A 2x heat transfer enhancement compared with filmwise condensation was estimated based on the condensation rate measured on the surface.

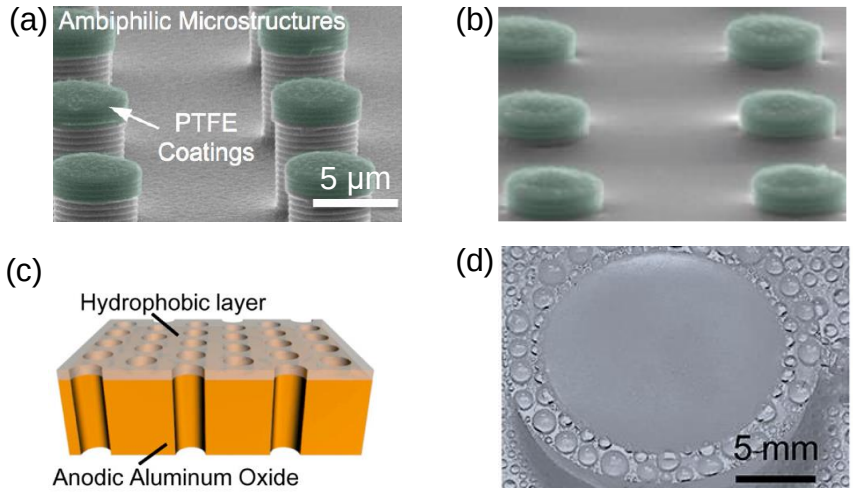

Figure 7. Biphilic porous structures for promoting thin-film condensation[75,76]. (a) Hydrophilic silicon micropillar arrays with hydrophobic PTFE coatings on top. (b) Under an environmental scanning electron microscope (ESEM), condensed water film was observed to be formed beneath the hydrophobic PTFE-coated top layer. (c) Anodic aluminum oxide (AAO) membrane with a hydrophobized top layer. (d) In a humid-air environment, the biphilic AAO membrane was able to absorb condensed water into the hydrophilic bottom layer, achieving "dry" surface atop the hydrophobic layer.

1.3 Challenges and Opportunities in Condensation Heat Transfer of Steam

While dropwise condensation has been developed for almost a century for condensation heat transfer enhancement, its application to industrial steam condensers remains challenging due to concerns about the coating delamination (especially in the case of SAM and thin polymer coatings), lubricant drainage (in the case of lubricant-infused surfaces), material and fabrication cost (especially in the case of re-entrant structures), and scalability of the surface structures/coatings (e.g., polymer infused porous surfaces).

On the other hand, enhanced filmwise condensation enabled by thermally conductive wicking structures has shown promises to enhance condensation heat transfer without the use of hydrophobic coatings, providing a pathway to enhance the condensation of steam in a robust and cost-effective manner. However, in wicking condensation, when the driving force for the condensed water to exit the wick layer is purely gravity, condensed water can easily flood the

wicking structures; otherwise, the wick becomes so thick that the heat transfer enhancement is marginal. Additional driving forces are required to assist gravity with pushing the condensed water out and maintaining a flooding-free surface for wicking condensation. Recent studies have proposed and demonstrated the use of a hydrophobic porous layer to generate capillary force as a driving force to achieve enhanced filmwise condensation by sustaining a thin liquid film during condensation. Combining capillary-driven thin-film condensation with wicking condensation is a promising approach to enhancing the condensation heat transfer of steam, but the following research is missing in the current literature:

1. Existing capillary-driven thin-film condensers rely on hydrophobic coatings[73-76]. Although these coatings may experience less shear force from the condensed water than the shear force the coatings would experience in dropwise condensation, delamination of these coatings over time remains a concern for their industrial applications. A capillary-driven thin-film condenser made of intrinsically hydrophobic materials could address the longevity concern.
2. Most capillary-driven thin-film condensers that have been studied do not have a thermally conductive wicking layer[75,76], or the dimension of the wicking layer and the hydrophobic layer are coupled[73]. However, the wicking layer and the hydrophobic layer carry different functionalities. The wicking layer needs to be highly permeable and thermally conductive, while the hydrophobic layer should contain small pore sizes to generate high enough capillary pressure. A separately designed wicking layer could better improve the thin-film condensation heat transfer performance.
3. There have been few direct heat transfer measurements for capillary-driven thin-film condensers in pure steam environments. And for the existing heat transfer measurements[73], there have been very few design guidelines for the structure of the capillary-driven thin-film condensers.

1.4 Description of the Concept

We propose to combine wicking condensation with capillary-driven thin-film condensation to enhance the condensation of steam, as illustrated in the schematic shown in Figure 8. The condenser surface is composed of a layer of robust hydrophobic membrane on top of a layer of high-thermal-conductivity, high-porosity, and high-permeability metal wick. In the process of

condensation, water condenses from the vapor environment surrounding the condenser tube onto the condenser surface, fills into the porous wick, and drains out through the designated shedding port as discrete droplets. The thin water-wick composite film, which is confined by the capillary pressure generated by the top layer hydrophobic membrane, enhances condensation heat transfer by minimizing the thermal resistance of the liquid film. This proposed approach has several key advantages as compared to what has been available in the literature:

1. Having separate layers of structures for the wick and the hydrophobic membrane decouples the driving force for the condensate drainage (i.e., capillary pressure generated by the membrane layer) and the viscous pressure resistance (i.e., viscous pressure loss occurring inside the wick layer). This opens up great opportunities for surface design. For example, we can have a nanoscale membrane pore size that generates an enormous capillary pressure while having a millimeter scale wick pore size that allows for low-friction condensate flow.
2. The use of a robust, intrinsically hydrophobic membrane eliminates the need for ultra-thin hydrophobic coatings, which addresses the concerns about coating delamination over time. Since the hydrophobic membrane is used for generating capillary pressure to hold the condensed liquid film beneath the membrane rather than for serving as a condensing surface, the membrane layer can be relatively thick as long as it is porous enough for vapor to travel through with minimal pressure loss.
3. Both the hydrophobic membranes and the high-thermal-conductivity metal wicks are commercially available and have great potential for scaling up. For example, intrinsically hydrophobic membranes such as poly(tetrafluoroethylene) (PTFE) and polyvinylidene fluoride (PVDF) membranes have been frequently used in the membrane distillation and water treatment industries[77-81]. Porous metal wicks such as sintered metal powders, metal meshes, metal foams, microscale metal grooves and fins have been fabricated on a large scale in the heat pipe industry and the condenser industry[82-85].

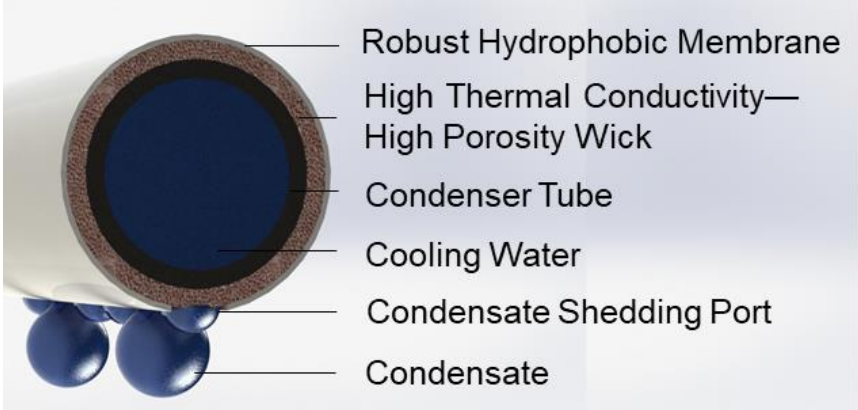

Figure 8: Rendering of the proposed capillary-driven thin-film condensation on a condenser tube. Water condenses from the vapor environment surrounding the condenser tube onto the condenser surface, fills into the porous wick, and drains out through the designated shedding port as discrete droplets. The thin water-wick composite film, which is confined by the capillary pressure generated by the top layer hydrophobic membrane, enhances condensation heat transfer by minimizing the thermal resistance of the liquid film. Robust materials are used for long-term applications.

1.5 Thesis Objective and Outline

The objective of this thesis is to improve the condensation heat transfer of steam via novel surface engineering designs based on capillary-driven thin-film condensation. Scalable materials and fabrication approaches are adopted for the potential application in industrial condensers.

In Chapter 1, the motivation for enhancing condensation heat transfer of steam was discussed. State-of-the-art surface designs, remaining challenges, and opportunities in the field were explained.

In Chapter 2, we developed a heat and mass transfer model to predict the heat transfer performance and flooding scenario for capillary-driven thin-film condensers which advises the selection of several key parameters of the membrane and the wick layer structures.

In Chapter 3, we fabricated a proof-of-concept sample based on commercially available copper foams and meshes. Condensation heat transfer performance of the sample was characterized in an environmental vacuum chamber and an up to 2x heat transfer enhancement

was demonstrated on the hierarchical copper sample even when the surface was flooded. Strategies to prevent flooding were discussed.

In Chapter 4, we investigated the scalable fabrication of hydrophobic membranes using electrospinning. We built an electrospinning setup and conducted a parametric study on the effects of several key fabrication parameters on the membrane morphology using fractional factorial design. The future direction for optimizing the electrospun membrane for the capillary-driven thin-film condenser was discussed. We explored the preliminary fabrication of a capillary-driven thin-film condenser surface made of electrospun fibrous membranes and porous copper wicks. An electrospun membrane-covered copper foam was characterized during vapor condensation under an ESEM. The remaining challenges in large-scale fabrication and the potential solutions are discussed.

In Chapter 5, we conducted a techno-economic analysis on the capillary-driven thin-film condensers based on the material cost, installation and shipping cost, and the value proposition for a steam power plant. We segmented the steam power plant market into different types based on the heat sources and the thin-film condensers were found to be most impactful on geothermal power plants.

In Chapter 6, perspectives on future work are presented.

2. Modeling

In this chapter, we developed a heat and mass transfer model to predict the heat transfer performance and flooding scenario for capillary-driven thin-film condensers which advises the selection of several key parameters of the membrane and the wick layer structures in the capillary-driven thin-film condenser surfaces.

A capillary-driven thin-film condenser is composed of two main parts, as shown in **Error! Reference source not found.**(a). First, a highly permeable, high-thermal-conductivity metal wick is placed on the condenser substrate. Second, a robust, intrinsically hydrophobic membrane is attached to the top of the wick. The porous metal wick serves as the structural support for the hydrophobic membrane and allows the passage of condensed water within its structure while enhancing the effective thermal conductivity of the liquid film. The hydrophobic membrane serves to confine the condensed water inside the hydrophilic wick layer and to

generate capillary-driving pressure to push the condensed water through the wick to the designated exit port.

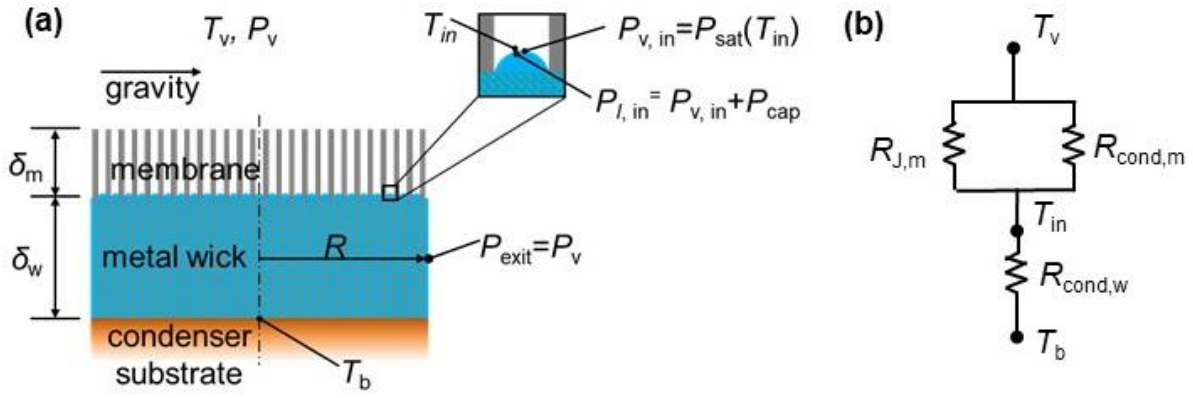

Figure 9: System schematics for the capillary-driven thin-film condenser (a) and system-level thermal resistance network (b).

Several assumptions are made in the system-level model:

(1) The system reaches steady state heat and mass transfer.

(2) Vapor at the top surface of the membrane has the same temperature as the far field vapor temperature T_v.

(3) Liquid-vapor interface is pinned at the membrane-wick boundary.

(4) Neglect heat loss on the sidewalls and assume heat transfer occurs in one dimension.

(5) The hydrophobic membrane has straight hole geometry and is characterized by constant permeability.

(6) Neglect disjoining pressure at the liquid-vapor interface so that Young-Laplace equation arrives at $P_{l,\text{in}} - P_{v,\text{in}} = 2\gamma H$.

(7) Neglect gravity in the porous wick, i.e., capillary force is the dominated driving force.

(8) Neglect convection and radiation heat transfer in the system.

2.1 Heat and Mass Transfer

Heat and mass transfer through the capillary-driven thin-film condenser can be divided into two processes in series, as illustrated by the thermal resistance network shown in **Error! Reference source not found.**(b). The first process is the heat and mass transfer through the

hydrophobic membrane, which occurs in two pathways[86]: (1) release of the latent heat associated with the condensed water vapor traveling through the membrane pores, as denoted by the thermal resistance $R_{\mathrm{J,m}}$; (2) conduction heat transfer through the membrane layer, as denoted by the thermal resistance $R_{\mathrm{cond,m}}$. After the condensation heat flux travels through the membrane layer, it passes through the porous metal wick to the condenser substrate through conduction heat transfer, as denoted by the thermal resistance $R_{\mathrm{cond,w}}$ in Figure 9(b).

The thermal resistance $R_{\mathrm{J,m}}$ is determined by the mass transfer of vapor through the membrane pores. The vapor can flow through the membrane pores in two major regimes. First, the vapor molecules can travel through a pore with minimal collisions between molecules, and most collisions with the membrane walls. This type of flow is named free-molecule flow or Knudsen flow. In the other regime, molecule-molecule collisions dominate over wall-molecule collisions. This is called viscous flow, or Poiseuille flow, and the equations for this type of flow are well developed[87]. There is a regime called the transition regime which considers molecule behavior from both the Knudsen and the Poiseuille flow regime[88]. To determine which regime we are in, the mean free path is compared against the pore diameter. The mean free path is the average distance that a molecule travels before it collides with another molecule. The mean free path is given by the following relation[89]

$$\lambda = \frac{k_{\mathrm{B}}T}{\sqrt{2}P\pi d_{\mathrm{c}}^2} \tag{1}$$

where k_{B} is the Boltzmann constant 1.3806485×10^{-23} J/K, T is the absolute temperature of the vapor, P is the vapor pressure, and d_{c} is the collision diameter for water molecules, 2.641×10^{-10} m.

The ratio between the mean free path and the pore diameter d_{p} is called the Knudsen number, $K_{\mathrm{n}} = \lambda/d_{\mathrm{p}}$, which gives a measure of the flow regime. If $K_{\mathrm{n}} > 10$ there is free-molecule or Knudsen flow. If $K_{\mathrm{n}} < 0.01$, Poiseuille flow ensues. If we are in between, $0.01 < K_{\mathrm{n}} < 10$, we are in the transition region where both effects should be included.

One of the most well-known models that describe the flow through porous media is the dusty-gas model[90]. This model can describe free-molecule flow, viscous flow, and continuum

diffusion as part of its development. Our system consists of single water molecules, which simplifies the equations significantly.

At a vapor saturation temperature of 35 ºC (which is within the typical range of the condensation temperature in steam power plants[91,92]), the resultant mean free path is around 2.4 μm. Thus, different flow types can occur below and above a 2 μm diameter. Pore diameters below 200 nm can be said to be in the Knudsen flow regime and those above 200 μm in the Poiseuille flow regime. We consider pore diameters between 0.1μm to 10μm, which is in the transition regime. For the transition regime, we must account for both the Knudsen and the Poiseuille flow contribution.

The pure, vapor-pressure-driven mass flux in the transition region can be described by

$$J = \overline{K}\Delta P \tag{2}$$

where ΔP is the pressure drop across the membrane pore, given by

$$\Delta P = \left(P_{\mathrm{v}} - P_{\mathrm{v,in}}\right) = \left(P_{\mathrm{v}} - P_{\mathrm{sat}}(T_{\mathrm{in}})\right) \tag{3}$$

where P_{v} is the vapor pressure at far field, and $P_{\mathrm{v,in}}$ is the saturation pressure at the vapor outlet (bottom) of the membrane pore, here approximated as the saturation pressure right outside the liquid-vapor interface.

$\overline{K}$ in equation (2) is the mean flow permeability for a pure gas given by

$$\overline{K} = \frac{1}{RTt_{\mathrm{m}}}\left(D_{iK} + \frac{\bar{P}B_{\mathrm{o}}}{\mu_{\mathrm{v}}}\right) \tag{4}$$

where t_{m} is the membrane thickness, R is the gas constant 8.3144598 J/mol/K, T is the absolute temperature, $\bar{P}$ is the average vapor pressure in the pore, D_{iK} is the Knudsen diffusion coefficient, B_{o} is the viscous flow parameter, and μ_{v} is the dynamic viscosity for pure vapor. The Knudsen diffusion coefficient can be shown to be proportional to the mean molecular speed from the kinetic theory of gasses,

$$D_{iK} = \frac{4}{3}K_{\mathrm{o}}\bar{v} \tag{5}$$

where K_{o} is the Knudsen flow parameter or permeability coefficient in the free molecule or Knudsen flow regime, and $\bar{v}$ is the mean molecular speed and is given by,

$$\bar{v} = \left(\frac{8RT}{\pi M}\right)^{\frac{1}{2}} \tag{6}$$

where M is the molar mass. For the simple case of a porous membrane consisting of cylindrical pores of length $\mathrm{t_m}$ and diameter $\mathrm{d_p}$, the Knudsen and Poiseuille flow parameters are simply related as $K_\mathrm{o} = d_\mathrm{p}/4$ and $B_\mathrm{o} = d_\mathrm{p}^2/32$ respectively. Thus, the mean flow permeability becomes[93]

$$\bar{K} = \frac{1}{RTt_\mathrm{m}}\left(\frac{1}{3}d_\mathrm{p}\left(\frac{8RT}{\pi M}\right)^{\frac{1}{2}} + \bar{P}\frac{d_\mathrm{p}^2}{32\mu_\mathrm{v}}\right) \tag{7}$$

The first term inside the brackets is the Knudsen flow permeability, which is directly proportional to the pore radius. The second term is the viscous or Poiseuille flow permeability, which is proportional to the pore diameter squared. As such, we can note that with increasing pore radius, the permeability increases faster in the Poiseuille regime than in the Knudsen regime. Equation (7) above is for the transition region, and through the dusty-gas model, simple additivity of both effects is implemented to account for both contributions. Usually, it is up to individual experiments to determine how good this approximation is, though previous work is stated to have shown excellent agreement. Critiques of this assumption can be found in the literature[90].

The unit in equation (2) is moles/m^2/s. To convert this to a mass flow rate, we multiply by the molar mass M in kg/mol. This quantity refers to the mass flux in one pore, so we multiply by the total frontal surface area A_T and the membrane porosity ϕ_m to obtain the total mass flow rate through the membrane. The mass flow rate through the pore is then given by

$$\dot{m} = \bar{K}\Delta P M A_\mathrm{T}\phi_\mathrm{m} \tag{8}$$

Assuming a circle shape to the frontal condensing surface of radius R, $A_\mathrm{T} = \pi R^2$. The mass flow rate is proportional to the porosity of the membrane. Maximizing membrane porosity can increase the vapor mass flow rate across the membrane. The membrane pore size determines both the membrane mass flux and the driving force for condensate flow (capillary pressure). Therefore, optimizing the pore diameter is crucial.

An enthalpy balance yields the following equation, accounting for condensation in each pore through the frontal surface area,

$$q_{\mathrm{J}} A_{\mathrm{T}} = \dot{m} h_{\mathrm{fg}} \tag{9}$$

Here, q_{J} is the surface-area-averaged condensation heat flux contributed by the vapor mass transfer through the membrane pores.

The other branch of heat flux through the membrane layer, i.e., conduction heat flux through the membrane layer, can be calculated by[86]

$$q_{\mathrm{cond,m}} = \frac{k_{\mathrm{eff,m}}}{t_{\mathrm{m}}} \Delta T_{\mathrm{m}} = \frac{(\phi_{\mathrm{m}} k_{\mathrm{v}} + (1 - \phi_{\mathrm{m}}) k_{\mathrm{m}})}{t_{\mathrm{w}}} (T_{\mathrm{v}} - T_{\mathrm{in}}) \tag{10}$$

where $k_{\mathrm{eff,m}}$ is the effective thermal conductivity of the vapor filled membrane layer; k_{v} and k_{m} are the thermal conductivity of the vapor and the membrane material, respectively; T_{in} is the temperature at the liquid-vapor interface.

Total condensation heat flux that's flowing through the membrane layer is the sum of the two components described above:

$$q = q_{\mathrm{J}} + q_{\mathrm{cond,m}} \tag{11}$$

Assuming 1D heat transfer, this total condensation heat flux is identical to the conduction heat flux flowing through the porous metal wick layer, which can be described by

$$q_{\mathrm{cond,w}} = \frac{k_{\mathrm{eff,w}}}{t_{\mathrm{w}}} \Delta T_{\mathrm{m}} = \frac{k_{\mathrm{eff,w}}}{t_{\mathrm{w}}} (T_{\mathrm{in}} - T_{\mathrm{b}}) \tag{12}$$

where $k_{\mathrm{eff.w}}$ are the effective thermal conductivity of the water-filled wick layer, and T_{b} is the wall temperature at the interface between the porous metal wick layer and the condenser substrate as shown in Figure 9(a).

2.2 Flooding Criterion

Flooding is an undesirable scenario for the capillary-driven thin-film condensation where the viscous pressure loss for the condensed liquid to exit through the wick layer becomes so large that the capillary driving force generated by the membrane cannot hold the condensed water inside the wick layer anymore. When flooding occurs, condensed water would burst out of the

membrane pores instead of maintaining a thin liquid film inside the wick layer, significantly adding thermal resistance to the system and therefore deteriorating the heat transfer performance.

Careful consideration should be taken in the surface design to prevent flooding. Figure 10(a) shows the direction of vapor and liquid flow through a capillary-driven thin-film condenser in an ideal scenario, where a thin liquid-metal wick composite film is confined by the hydrophobic layer and all condensed water would exit out of the wick through designated exit ports. To ensure such a scenario, the viscous pressure loss experienced by the condensed water through the porous metal wick needs to be compensated by the driving face provided by the capillary pressure generated by the membrane pores. Figure 10 (b) shows the pressure profile of the condensate flow in the case of a flat, circular condenser surface with radius *R*. Pressure at the liquid side of the liquid-vapor interface $P_{\mathrm{l,in}}$ can be calculated by adding the capillary pressure generated by the liquid-vapor interface curvature P_{cap} to the pressure at the vapor side of the liquid-vapor interface $P_{\mathrm{v,in}}$, as shown in Figure 9(a) and Figure 10(b):

$$P_{\mathrm{l,in}} = P_{\mathrm{v,in}} + P_{\mathrm{cap}} = (P_{\mathrm{v}} - \Delta P_{\mathrm{p}}) + P_{\mathrm{cap}} \tag{13}$$

where ΔP_{p} is the vapor pressure drop across the membrane layer and P_{cap} is limited by the pore size of the membrane d_{p} and the advancing water contact angle on the membrane material θ_{adv}:

$$P_{\mathrm{cap}} \leq \frac{-4\gamma \cos\theta_{\mathrm{adv}}}{d_{\mathrm{p}}} \tag{14}$$

Here, we compare the maximum viscous pressure loss (viscous pressure loss at the exit port) to the maximum driving force (contact angle at the vapor-liquid interface approaching $\cos\theta_{\mathrm{adv}}$), and utilize the following criterion for flooding prediction:

$$0 < P^{*} = \frac{P_{\mathrm{vis,max}}}{P_{\mathrm{l,in}} - P_{\mathrm{v}}} < 1 \tag{15}$$

Flooding would occur if P^{*} is out of the (0,1) range. In the case of a flat, circle shape condenser surface as shown in Figure 9(b), P_{vis} can be derived as following using 1D Darcy's law[94],

$$\frac{\dot{V}(r)}{2\pi r t_{\mathrm{w}}} = -\frac{\kappa dP}{\mu dr} \tag{16}$$

where $\dot{V}(r)$ is the volumetric flux at radius r, and can be expressed in terms of condensation heat flux q by mass conservation:

$$\dot{V}(r) = \frac{\pi r^2 q}{\rho_l h_{fg}} \tag{17}$$

where ρ_l is the density for liquid water, h_{fg} is the latent heat of the water. Note that gravity is neglected here since we expect the capillary pressure to be the dominant driving force.

Assuming the side wall of the wick layer to be the exit port of the capillary-driven thin-film condenser, the maximum viscous pressure loss that the condensed water would experience in the ideal scenario should be the viscous pressure loss from the center of the condenser surface to the edge of the condenser surface (i.e., $r = R$). Integrating the viscous pressure loss along the radius of the condenser surface, the maximum viscous pressure loss can be obtained as follows:

$$P_{vis,max} = P_{vis}(r = R) = \frac{\mu R^2 q}{4\rho_l h_{fg} \kappa t_w} \tag{18}$$

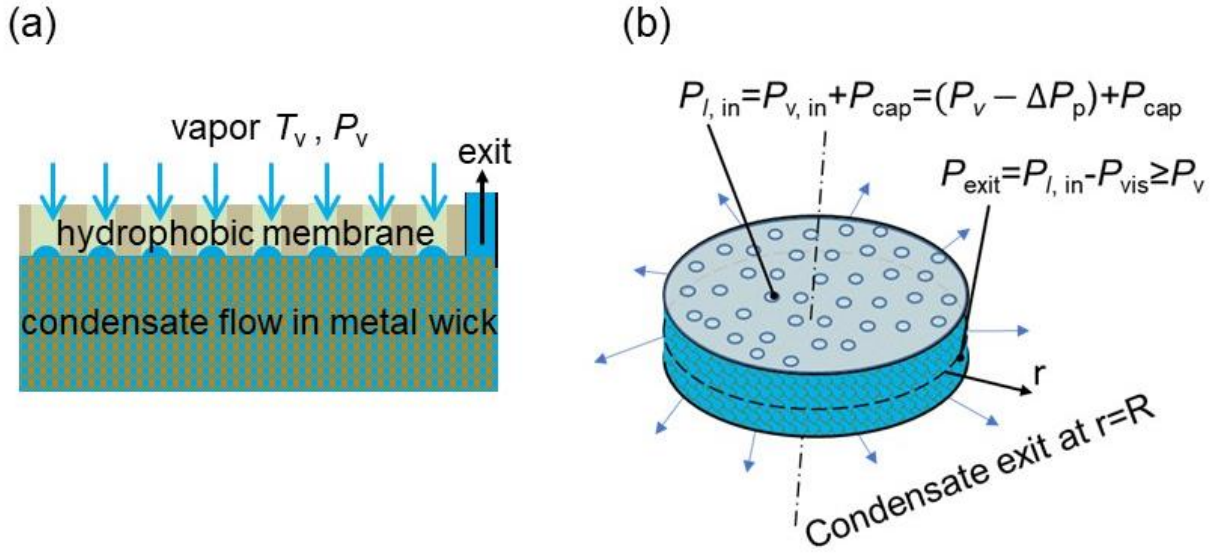

Figure 10: Direction of condensate flow in the capillary-driven thin-film condenser (a) and the pressure profile of the condensate flow in the case of a flat, circular condenser surface with radius *R*.

2.3 Parametric Study

In order to maximize heat transfer performance and to prevent flooding from occurring, both the structures of the metal-wick and the hydrophobic membrane must be designed. Important parameters for the porous wick layer are the wick permeability κ, the effective thermal conductivity of the wick-water composite $k_{\mathrm{eff,w}}$, and the wick thickness t_{w}. Important parameters for the hydrophobic membrane layer are the membrane pore size d_{p}, the membrane porosity ϕ_{m}, water contact angle (advancing) θ_{adv}, and the membrane thickness t_{m}. These seven parameters are chosen to investigate their effects on the system-level heat transfer performance. When one parameter is varied, the other seven parameters are kept as constant as listed in Table 1.

Table 1: Default values for the parametric study.

Item	Value
Membrane pore size d_{p} [μm]	5
Water contact angle (advancing) on membrane θ_{adv} [°]	100
Membrane porosity ϕ_{m} [/]	0.8
Membrane thickness t_{m} [μm]	100
Wick thickness t_{w} [μm]	200
Wick permeability κ [m^2]	5×10^{-11}
Wick effective thermal conductivity $k_{\mathrm{eff,w}}$W/mK]	100
Thermal conductivity of membrane materials [W/mK]	0.2[95]
Far-field vapor temperature T_{v} [°C]	35
Condenser wall temperature T_{b} [°C]	30
Diameter of the circular-shape, flat condenser R [m]	0.0127

Figure 11 shows the modeling strategy for calculating the temperature profile and the corresponding heat flux during the capillary-driven thin-film condensation. For a given vapor temperature T_{v} (35 °C) and a prescribed liquid-vapor interface temperature $T_{\mathrm{in,1}}$, through the membrane model discussed in equations (2)-(11), total heat flux q can be calculated by adding

the heat flux components contributed by the vapor mass transfer and the conduction heat transfer. Plugging in the derived heat flux and the given wall temperature T_b (30 °C) into the wick model (equation (12)), a new liquid-vapor interface temperature $T_{in,2}$ can be derived. The two temperatures $T_{in,1}$ and $T_{in,2}$ are iterated until a converged value is found.

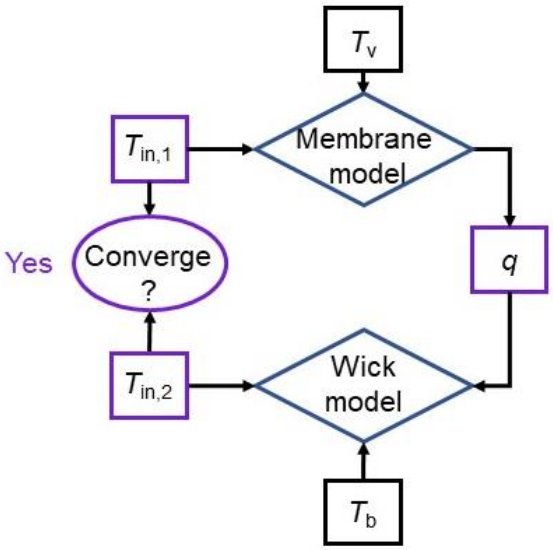

Figure 11: Modeling strategy for calculating the temperature profile and the corresponding heat flux during the capillary-driven thin-film condensation.

Once the temperature profile is solved, we can derive the pressure profile following equations (13)-(18) and determine if flooding would occur. In our model, we calculate the heat flux assuming that the thin-film condensation is achieved without flooding. However, when the

flooding criterion *P** is out of the required range of (0,1), we know that flooding would occur and the heat flux predicted by the model would not reflect the actual heat transfer performance.

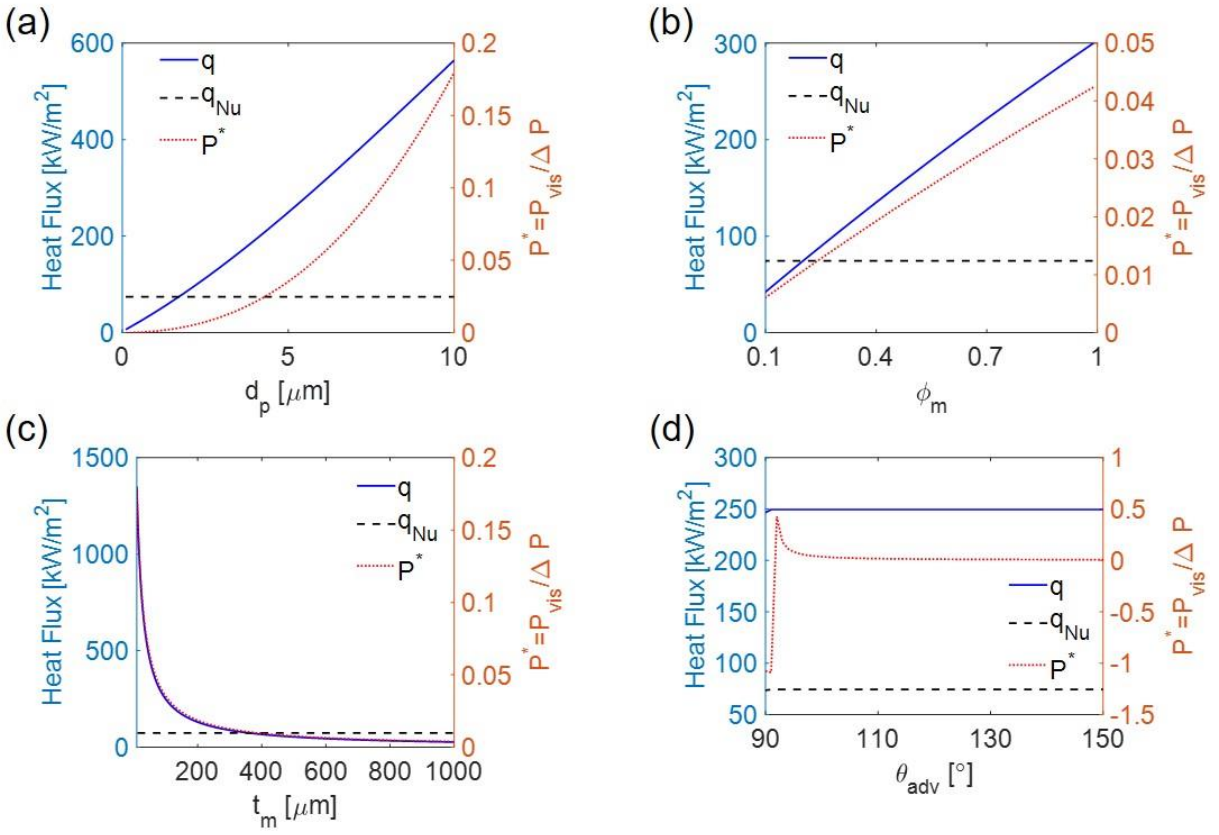

Figure 12: Parametric study on the effects of key membrane parameters on the heat transfer performance and the flooding criterion, assuming these parameters are independent of each other. Black dashed line shows the baseline filmwise condensation heat flux for the given vapor temperature (35 °C) and surface subcooling (5 °C), as predicted by the Nusselt model. The blue line shows the heat transfer performance of the capillary-driven thin-film condenser assuming no flooding occurs. The orange dotted line shows the flooding criterion P^* which needs to be in the range of (0,1) to prevent flooding. (a) Membrane pore size varies from 0-10 µm. (b) Membrane porosity varies from 0.1-1. (c) Membrane thickness varies from 10-1000 µm. (d) The advancing contact angle of water on membrane materials varies from 90-150°.

Figure 12 shows the parametric study on the effects of key membrane parameters on the heat transfer performance and the flooding criterion, assuming these parameters are independent of each other. Black dashed line shows the baseline filmwise condensation heat flux for the given vapor temperature (35 °C) and surface subcooling (5 °C), as predicted by the Nusselt model. The blue line shows the heat transfer performance of the capillary-driven thin-film condenser

assuming no flooding occurs. The orange dotted line shows the flooding criterion P^* which needs to be in the range of (0,1) to prevent flooding.

Figure 12(a) shows that the heat transfer performance of the thin-film condenser gets enhanced almost linearly with the increase in the membrane pore size. This is due to the enhanced vapor flow through the membrane pores and the reduced mass transport resistance given by the larger membrane pore size. When membrane pore size is extremely small (i.e., below 1.7 μm), heat transfer through the membrane layer becomes so poor that the overall heat transfer performance of the thin-film condenser becomes worse than a conventional filmwise condensation, even though flooding is prevented. Meanwhile, P^* increases significantly with increasing membrane pore size, although it keeps within the non-flooding regime (0,1) for the range of membrane pore size considered. It is worth noting that the rate of the increase in P^* also increases as membrane pore size gets larger. The major reason for this is that the capillary driving force is inversely proportional to the pore size. As pore size gets larger, the capillary pressure (which determines the denominator in the expression for P^*) decreases dramatically, leading to an increasingly larger P^*. Therefore, membrane pore size is crucial for balancing the tradeoff between the heat transfer enhancement and flooding development. A maximized membrane pore size that is within the non-flooding regime is desired.

Figure 12(b) shows that higher membrane porosity will enhance the heat transfer performance of the system and simultaneously increase the P^*. As membrane porosity increases, more vapor can travel through the membrane holes, and therefore resistance to mass transfer is lower. Consequently, heat flux transferred through the membrane increases. As a result of the increased heat flux, viscous pressure loss within the wick layer also increases. Thus, P^* also increases. In order to get at least 2x heat transfer enhancement as compared to the filmwise condensation, a membrane porosity of at least 45% is needed. Although higher porosity could increase P^*, the effect of porosity on the P^* is not as significant as the effect of pore size on the P^*. P^* remains in a safe range (<0.05) throughout the parametric sweep of the membrane porosity from 10% to 100%.

Figure 12(c) shows that as membrane thickness gets larger, the heat transfer performance of the condenser degrades significantly, and P* decreases correspondingly. A thicker membrane increases both the thermal resistance related to the conduction heat transfer through the

membrane layer and the resistance to vapor transport through the membrane pores. Therefore, when increasing membrane thickness, heat transfer performance declines. However, the reduced heat flux will generate less viscous pressure loss inside the porous wicks. As a result, P^* gets smaller when the membrane gets thicker, which means it is less likely to flood. The effect of membrane thickness on the thin-film condenser's heat transfer performance and flooding development is most significant when the membrane is thin (i.e., below 100 μm). This is because the heat transfer rate (both the mass transfer part and the conduction heat transfer part) through the membrane layer is inversely proportional to the membrane thickness. At a small membrane thickness, this heat transfer rate drops dramatically as the membrane gets thicker. Figure 12(c) also shows that, in order to obtain at least 2x heat transfer enhancement as compared to the filmwise condensation, the membrane needs to be thinner than 175 μm. An ideal membrane thickness should be minimized while ensuring that P^* is in the non-flooding regime.

Figure 12(d) shows that the hydrophobicity of the membrane material does not have an impact on the thin-film condenser's heat transfer performance when the surface is not flooded. However, at a low advancing contact angle of water (i.e., less than 92°), the membrane pore may not be able to generate enough capillary pressure to even compensate for the pressure loss experienced by the vapor traveling through the membrane pore, as indicated by the negative P^* regime shown in Figure 12(d). Once θ_{adv} is higher than 95°, P^* drops to below 0.1 and the effect of θ_{adv} on the flooding development becomes a minor concern.

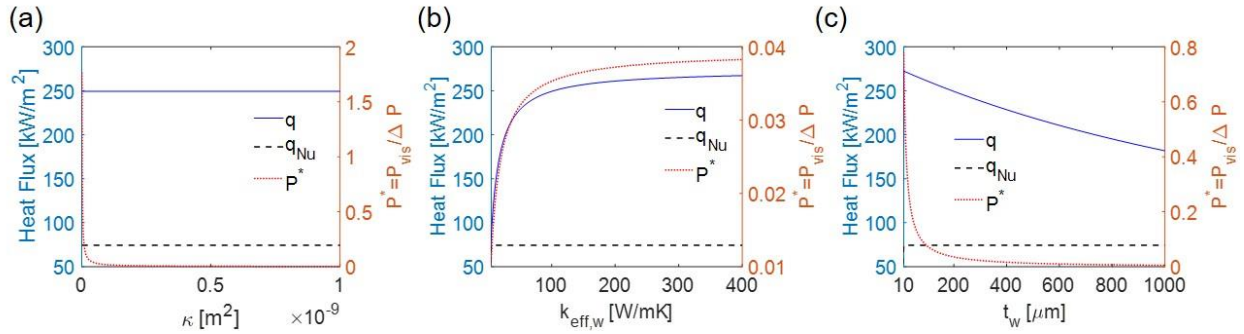

Figure 13: Parametric study on the effects of key wick parameters on the heat transfer performance and the flooding criterion.

Figure 13 shows the parametric study on the effects of key wick-layer parameters on the heat transfer performance and the flooding criterion, assuming these parameters are independent of each other. Like Figure 12, here the black dashed line represents the baseline filmwise condensation heat flux for the given vapor temperature (35 °C) and surface subcooling (5 °C);

the blue line shows the heat transfer performance of the capillary-driven thin-film condenser assuming no flooding occurs; the orange dotted line shows the flooding criterion P* which needs to be in the range of (0,1) to prevent flooding.

Figure 13(a) highlights the significant impact of the wick permeability on the flooding development of the thin-film condenser surface especially when the permeability is low. When permeability is below 1.8×10^{-12} m^2, P^* exceeds 1, which means that flooding would occur. When permeability exceeds 1.8×10^{-11} m^2, P^* drops below 0.1, and the effect of permeability on the flooding development becomes minimal. P^* drops the fastest at the smallest permeability. This is because according to equation (18), the viscous pressure loss (the numerator of the expression for P^*) is inversely proportional to the wick permeability. As a result, P^* is most sensitive to the changes in the wick permeability when the permeability is low. The heat transfer performance of the thin-film condenser stays as constant regardless of the change in the wick permeability. This is because of the assumption that the wick permeability is independent of other properties of the wick that could affect its heat transfer performance (i.e., thickness, effective thermal conductivity).

Figure 13(b) shows that increasing the effective thermal conductivity of the wick layer has a significant impact on the heat transfer performance of the thin-film condenser especially when this effective thermal conductivity is low. Here, we sweep the effective thermal conductivity from a lower bound of 5 W/mK to a higher bound of 400 W/mK (thermal conductivity of copper). Increasing the effective thermal conductivity of the wick layer can reduce the thermal resistance associated with the conduction heat transfer through the wick layer and therefore improve overall heat transfer. Once the effective thermal conductivity becomes large enough (in this case, $k_{\mathrm{eff,w}} > 50$W/mK), the dominant thermal resistance in the system becomes the membrane layer and the effects of $k_{\mathrm{eff,w}}$ on the system level heat transfer declines. Increased heat flux generates higher viscous pressure loss inside the wick layer. Consequently, P^* increases with increasing $k_{\mathrm{eff,w}}$, though the increase is negligible as compared to 1.

Figure 13(c) shows the effect of the wick layer thickness on the heat transfer performance and the flooding development on the thin-film condenser. At the given effective thermal conductivity of the wick ($k_{\mathrm{eff,w}}$=100 W/mK) and the given membrane properties, the thermal resistance associated with the wick layer is relatively small as compared to the membrane layer

even when the wick thickness approaches 1 mm. Therefore, the total condensation heat flux only gently decreases with the wick thickness varying from 10 μm to 1000 μm. On the other hand, as shown in equation (18), the viscous pressure loss (the numerator of the expression for P^*) is inversely proportional to the wick thickness. Therefore, P^* drops strikingly with the increase in the wick layer thickness when the wick is thin. Once the wick is thicker than 70 μm, P^* drops below 0.1, and the effect of t_w on the flooding development becomes negligible.

2.4 Conclusions and Guidelines on Material Selections

In this chapter, we developed a heat and mass transfer model to predict the heat transfer performance and the flooding scenarios of the capillary-driven condenser. We performed a parametric study on the effect of the following key design parameters on the system level heat transfer performance and flooding development: membrane pore size d_p, membrane porosity ϕ_m, membrane thickness t_m, membrane water contact angle (advancing) θ_{adv}, wick permeability κ, the effective thermal conductivity of the wick layer $k_{eff,w}$, and the wick layer thickness t_w. Key findings from the parametric study and the guidelines for the material selections for the capillary-driven thin-film condenser surfaces are:

- Membrane thickness and membrane pore size are the top two important parameters for heat transfer enhancement. A minimized membrane thickness with a maximized membrane pore size within the non-flooding regime are highly desired.
- An increase in membrane porosity has a gently positive impact on the heat transfer performance and can marginally develop flooding incidents, while membrane hydrophobicity is less important unless θ_{adv} becomes less than 95°.
- Wick permeability is crucial for flooding prevention especially when the permeability is low. When permeability is below 1.8×10^{-12} m^2, flooding would occur.
- Effective thermal conductivity of the wick layer has minimal impact on the flooding development, but its increase can significantly enhance the heat transfer performance of the thin-film condenser when its value is low. Once the effective

thermal conductivity becomes large enough ($k_{\mathrm{eff,w}} > 50\mathrm{W/mK}$), its impact on the heat transfer becomes gentle.

- Increasing wick thickness will gently decrease the heat transfer performance but will dramatically prevent flooding from occurring especially when the wick is thin. Once the wick is thicker than 70 μm, P^* drops below 0.1, and the effect of t_{w} on the flooding development becomes negligible.

Note that in the parametric study we assumed that the parameters are independent of each other and that we can pick a value for them in a wide range of variations. This is an ideal assumption. In reality, some parameters may be interconnected and cannot vary independently with each other. For example, the wick permeability may affect the effective thermal conductivity of the wick, as these two are commonly affected by the arrangement of the metal network inside the wick layer. In addition, there are practical limitations on what value we can choose for certain parameters. For instance, intrinsically hydrophobic membrane materials we can find on the market such as PTFE, PE and PVDF usually have advancing contact angles of ~ 100°. We do not have much choice about θ_{adv} there. Nevertheless, the model framework we developed and the parametric study we conducted provides a design guideline and optimization direction for the capillary-driven thin-film condenser surfaces with any materials and structures that are available to us.

3. Condensation Experiment on Hierarchical Copper

In this chapter, as a proof of concept study, we experimentally fabricated and tested a capillary-driven thin-film condenser made of commercially available materials. Starting with materials selection guided by the model framework developed in Chapter 2, we down-selected porous copper foams as the wick layer materials and a thin copper mesh as the membrane layer. We chose to modify the thin copper mesh with a hydrophobic coating over to use an intrinsically hydrophobic membrane due to several practical challenges. We observed thin-film condensation on a biphilic, microchannel-assisted hierarchical copper sample, and we experimentally measured an up to 2x heat transfer performance as compared to a filmwise condensation even in the case of flooding on our sample. Achieving a flooding-free condensation on the hierarchical copper sample is challenging due to the fragility of the mesh pores. The design of microchannels into the wick layer can improve the permeability of the wick layer and delay surface flooding.

3.1 Sample Fabrication and Characterization

This section entails the rationale for using copper foams and copper mesh as the wick layer and the membrane layer for the proof-of-concept sample fabrication. We characterized the permeability of the copper wick, which is a critical property that determines flooding incidents. The hierarchical copper sample was fabricated by diffusion bonding under high temperature and pressure followed by a biphilic coating procedure, as detailed below.

3.1.1 Commercially Available Choices and Materials Down Selection

To achieve thin-film condensation with scalable materials, we reviewed commercially available material candidates and down-selected the wick and the membrane materials.

3.1.1.1 Materials Selection for the Wick Layer

The wick layer is a core component of the capillary-driven condenser design, which reduces the thermal resistance through integrating the condensate liquid film with a high-thermal conductivity structured wick of a required thickness. According to the model framework, a wick with higher permeability, higher thermal conductivity, and less thickness is preferable.

Various types of structured wicks are available commercially. Compared to wire cloth, perforated sheets are more rigid and durable for a longer service life in harsh environments. However, both wire cloth and perforated sheets are closed-cell structures that constitute individual enclosures. On the other hand, metal foams consist of cells that are all interconnected, allowing the condensate fluid to pass through the wicking structure. Metal foams also provide a higher porosity than other types of metal wicks, with a potential to be more permeable than other types of wicks.

The thickness of the metal wicks determines the thickness of the condensate film and therefore plays an important role in the condensation heat transfer performance. Pore size or grid size of the porous metals effectively determines the flooding scenarios, mainly through the wick permeability, which usually increases with increasing pore size. Permeability needs to be optimized when considering the pore size of the wick structures.

The metal thermal conductivity and the volumetric porosity are critical to the effective thermal conductivity of the porous metal materials, $k_{\text{eff,w}}$, although $k_{\text{eff,w}}$ not only depends on the relative density and the thermal conductivity of the structure but also on the actual geometry of the porous structure and the contact conditions of the metal network[70,96] A wick structure with higher interconnection such as porous metal foams would allow heat to be conducted through the metal part more easily and thus enable a higher effective thermal conductivity. A disconnected porous metal structure such as channels would have a lower effective thermal conductivity due to the presence of the bulk, low-thermal-conductivity water in between the disconnected metal parts[97]. From an ideal and physical perspective, the maximum value for the effective thermal conductivity of a porous metal wick can be achieved through a parallel arrangement for the heat to flow through the metal part and the liquid-filled void, while a series arrangement would result in the lowest effective thermal conductivity, as shown in

$$k_{\text{eff,max}} = (1-\phi)k_{\text{s}} + \phi k_{\text{l}} \tag{19}$$

$$k_{eff,\text{min}} = \left[\frac{(1-\phi)}{k_{\text{s}}} + \frac{\phi}{k_{\text{l}}}\right]^{-1} \tag{20}$$

where ϕ denotes the volumetric porosity of the porous metal wick, k_{s} and k_{l} are the thermal conductivity of the solid phase (metal) and the liquid phase (water inside the voids) of the water-metal wick composite. A simple comparison of the effective thermal conductivity of commonly

used porous metal wicks and the theoretical upper and lower boundaries for their effective thermal conductivity are shown in Figure 14.

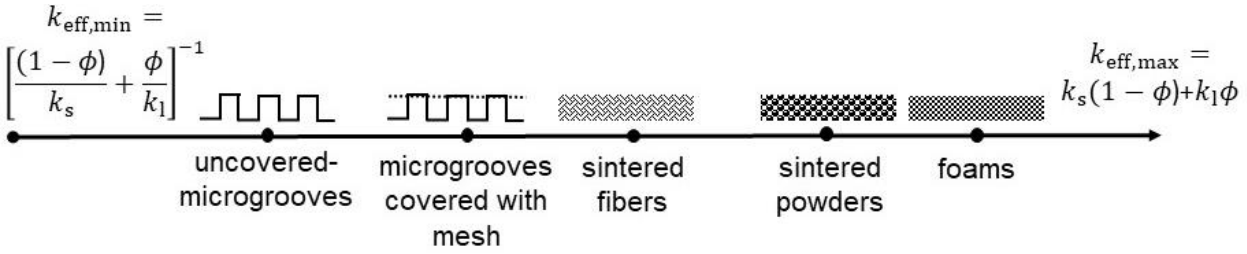

Figure 14: Upper and lower boundaries for the effective thermal conductivity of porous metal wick and a comparison of the effective thermal conductivity of commonly used porous structures made of the same metal material.

As regard to cost-effectiveness, steel wire cloth has a relatively low unit price as compared to other materials, but its thermal conductivity is also relatively low. Copper has the best thermal conductivity among the listed materials and has a mid-range price.

We chose copper foams as sample materials for fabricating the wick structures because of their high scalability, high thermal conductivity, high permeability as compared to other wicking structures, and a wide range of thickness options. According to the modeling results, a thinner wicking structure can reduce the thermal resistance through the liquid-wick composite layer and therefore enhance condensation heat transfer. However, the thickness of the copper foam is limited by its characteristic structure size, lower than which the pores may not be complete and the copper foam structures may not be interconnected anymore — in which case both the effective thermal conductivity and the permeability of the wick structure can be reduced significantly and the heat transfer performance of the thin-film condenser will deteriorate.

Commercially available copper foams usually have a thickness above 0.5 mm, but they can be milled or roller-pressed to be thinner while keeping their functions if pores remain connected. The thinnest copper foams we could find on the market are the ones that were roller-pressed from a high-purity, electrodeposited copper foam. Figure 15 shows an optical image and an SEM image of one of the copper foams we have used. This copper foam has pore sizes ranging from tens of microns to up to ~300 μm with an average pore size of ~200 μm. The copper foam is composed of highly packed layers of copper nets in the direction perpendicular to its surface. The copper nets are well-connected in directions tangential to its surface plant, while the contact between each layer of the copper nets is less tight. Therefore, its effective thermal

conductivity along the x-y plane of its surface can be superior to its effective thermal conductivity along the z-direction. Since it contains multiple layers of identical porous metal nets, it can potentially be machined to be even thinner.

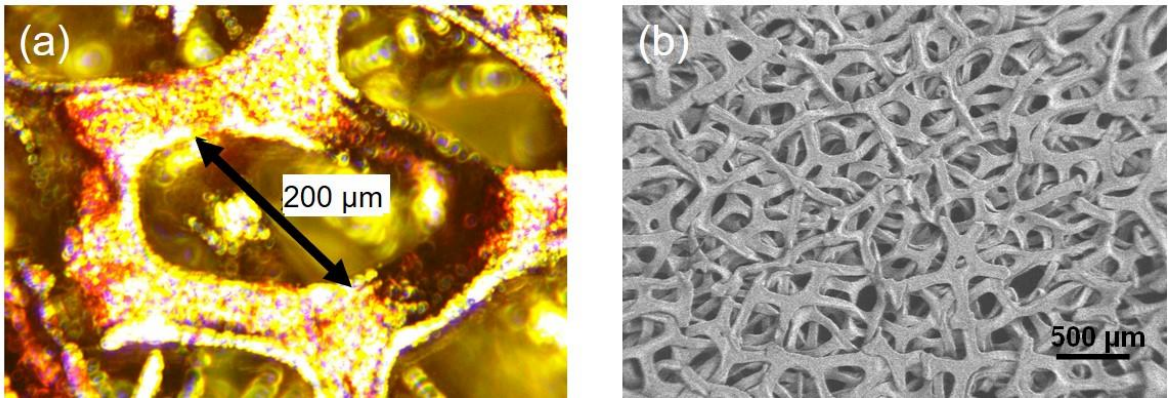

Figure 15: Optical image and SEM image for a porous copper foam with a characteristic pore size of ~220 µm and porosity of ~70%.

A detailed description of the three copper foam structures we have used in this thesis can be found in Table 2. All three copper foams are composed of compressed layers of copper nets as shown in Figure 15(b), with different porosity and thickness measured. Permeability characterization of these copper foam structures will be discussed in Section 3.1.2.

Table 2. The geometry of the three copper foam samples selected as wick layer candidates.

Copper foam ID	Porosity	Thickness	Geometry
1	70%	220 µm	Compressed layers of copper nets as shown in Figure 15(b).
2	85%	180 µm	
3	50%	130 µm	

3.1.1.2 Materials Selection for the Membrane Layer

The hydrophobic membrane is another core component of the capillary-driven thin-film condenser design, which provides capillary pressure to drive the condensate transport into the wick structures below the membrane. Many hydrophobic membrane materials are commercially available, such as polytetrafluoroethylene (PTFE), polycarbonate (PC), polypropylene (PP) and polyvinylidene difluoride (PVDF).

PTFE membranes are intrinsically hydrophobic, chemically stable, and applicable to large scale industrial applications. They have a relatively wide range of pore size (0.1-10 μm) and thickness that are commercially available, and their prices vary from several hundred to several thousands of dollars per meter squared depending on the geometry. The unlaminated PTFE membranes do not have a supportive layer, while the laminated ones have a supportive layer of PP or polyester (PE) to enhance the mechanical performance of the membrane.

Another intrinsically hydrophobic potential membrane material is PP. PP membranes are strong, flexible, and compatible with a broad range of chemicals. They also have a relatively wide range of pore sizes and thicknesses that are commercially available, though for large pore sizes (>0.2 μm) the pores are no longer cylindrical and the nominal pore size is used as a representation. PP membranes have a similar range of costs as PTFE membranes. PVDF membranes are also intrinsically hydrophobic, but they have relatively higher prices as compared to other membrane materials.

Although these commercially available hydrophobic membranes all have water contact angles (advancing) above 100°, which generates a high capillary pressure driving force, there are rare membrane materials that have a large pore size and a small thickness. Membranes with pore sizes no smaller than 5 μm usually come with a thick supportive layer to enhance the mechanical performance of the membrane or have a thickness beyond 150 μm. Only a few membrane options have a thickness below 100 μm and they typically have a pore size smaller than 1 μm. However, according to the design guideline provided by the model framework, the heat transfer performance of the thin-film condenser gets enhanced with increasing membrane pore size and decreasing membrane thickness. A membrane thinner than 175 μm with a pore size larger than 5 μm is desired for heat transfer enhancement.

In addition to the challenge of finding a hydrophobic membrane with an ideal geometry, obtaining a robust bonding between the hydrophobic membranes and the porous metal wicks remains challenging. Therefore, for proof of concept, we chose to use a simpler technique to fabricate the membrane layer: make hydrophobic a thin layer of metal mesh capillary condenser surfaces, which can be diffusion bonded to the copper wick in a robust manner.

Figure 16 shows an SEM image for the copper mesh we selected as the membrane material for the proof of concept study. It has a pore size of 11 μm and a thickness of 5 μm.

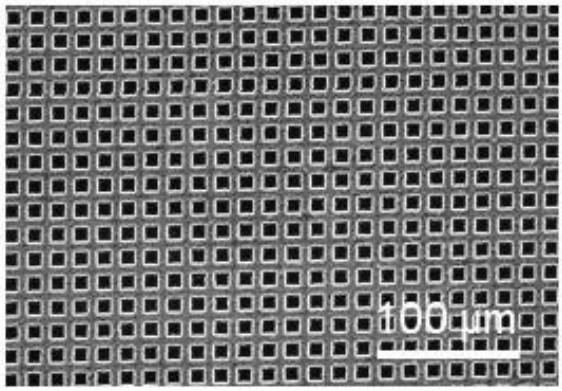

Figure 16: SEM image of the 1500-mesh-size copper mesh selected as the membrane material for the hierarchical copper sample.

3.1.2 Material Characterization

We measured the thickness of the copper foams using a micrometer and the results are shown in Table 2. The porosity of the copper foam is derived by its weight and volume, and the results are listed in Table 2. One key parameter that is unknown is the permeability of the copper foam, which can by measuring the propagation of fluid through the copper foam sample as a function of time following a well-known procedure[70]. Figure 17 shows a schematic of the testing apparatus for measuring the permeability of the copper foam samples. The testing apparatus is comprised of a fluid reservoir filled with deionized water, a copper foam sample that is held stationary by a sample clip, a translation stage to control the vertical location of the sample clip, a light source for supplemental illumination (not shown in the schematic), and a camera for recording the propagation of water inside the copper foam sample.

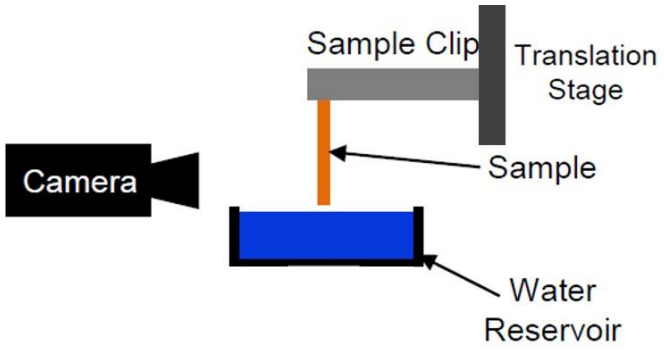

Figure 17: Schematic of the testing apparatus for measuring the permeability of the copper foams.

Prior to the measurement, a rectangular copper foam sample was cleaned with acetone in an ultrasonic cleaner for 5 minutes, followed by ethanol-IPA rinsing, and then dipped into 2 M hydrochloric acid in water for 1 minute, rinsed with water, acetone, ethanol, and IPA, dried with a clean nitrogen stream, and finally, plasma cleaned with argon plasma for 15 minutes, at which point the contact angle on copper was approximately zero degree. After the plasma cleaning process, the sample was immediately mounted on the sample clip, and was lowered slowly until contact was made between the sample and the deionized water in the fluid reservoir, at which point the wicking process was observed with the speed camera. The propagation of the liquid wicking front was quantified by post-processing the videos using Image J.

To determine the permeability of the sample copper foams with the experimental data, we modelled the fluid propagation with the one-dimensional Darcy's law with gravitational effects included to account for liquid propagation against gravity over a distance greater than the capillary length:

$$\frac{dy}{dt} = \frac{-\kappa}{\mu\phi}\left(\frac{-\Delta P_{\text{cap}}}{y} + \rho g\right) \tag{21}$$

where y is the propagation length measured from the liquid wicking front to the water level in the reservoir, t is the propagation time, μ and ρ are the viscosity and density of the testing fluid (water in this case), g is the gravitational acceleration, and ϕ is the porosity of the copper foam sample, which has been determined by measuring the apparent density of the copper foams; κ and ΔP_{cap} are permeability and capillary pressure of the copper foam sample, respectively, which can be determined from fitting the model solution to the experimental data as follows.

The solution to the Darcy's law expressed as equation (21) can be found explicitly for time as a function of the distance over which the fluid has propagated:

$$\mathrm{t} = -\frac{Aln(A-By)+By-Aln(A)}{B^2}, A = \frac{\kappa \Delta P_{cap}}{\mu \phi}, B = \frac{\kappa \rho g}{\mu \varphi} \tag{22}$$

Substituting the values for the physical parameters μ, ϕ, ρ and g into the above solution, and plotting the measured propagation time t versus the measured propagation length y, the two unknown parameters κ and ΔP_{cap} for the copper foam sample can be determined by fitting the experimental data to the solution curve. Note that the permeability of the copper foam κ is a geometric parameter that does not change when using different fluids for the wicking test, while the capillary pressure ΔP_{cap} does change from fluid to fluid. However, if all the fluids considered have the same contact angle (e.g., zero degree), then the ratio of capillary pressure ΔP_{cap} for two different fluids through a given copper foam is equivalent to the ratio of their surface tensions.

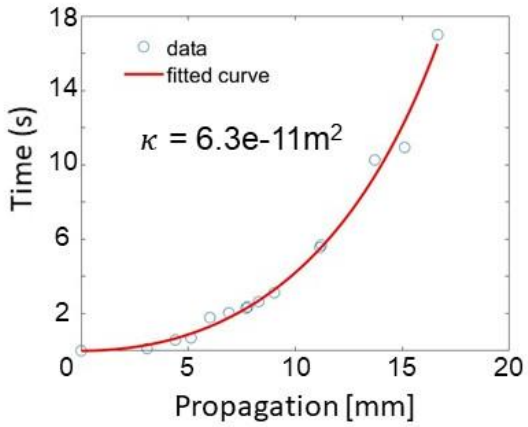

Figure 18: Experimental data (blue dots) and fitted curve (red solid line) showing the propagation time as a function of the distance over which the deionized water has propagated within the first copper foam sample. Permeability was measured to be 6.3×10^{-11} m^2.

Figure 18 shows the experimental data and the fitted curve for the propagation time against the propagation length for the first copper foam sample (thickness ~ 220 μm). By fitting the experimental data to the solution to the Darcy's law (equation (22)), the permeability κ of the first copper foam sample was determined to be 6.3×10^{-11} m^2, which according to the modeling result shown in Figure 13(a) should be high enough to have small impacts on the flooding development of the thin-film condensation.

3.1.3 Diffusion Bonding Procedure

We started fabricating capillary-driven thin-film condensers based on a 1-inch diameter copper block, which was fabricated by mechanically and then chemically polishing the end of a copper block followed by solvent and acid cleaning the surface. In order to obtain good thermal contact between the copper condenser block, the copper foam wick, and the metal mesh membrane, we diffusion-bonded the copper foam and the metal mesh to the block under high temperature and pressure.

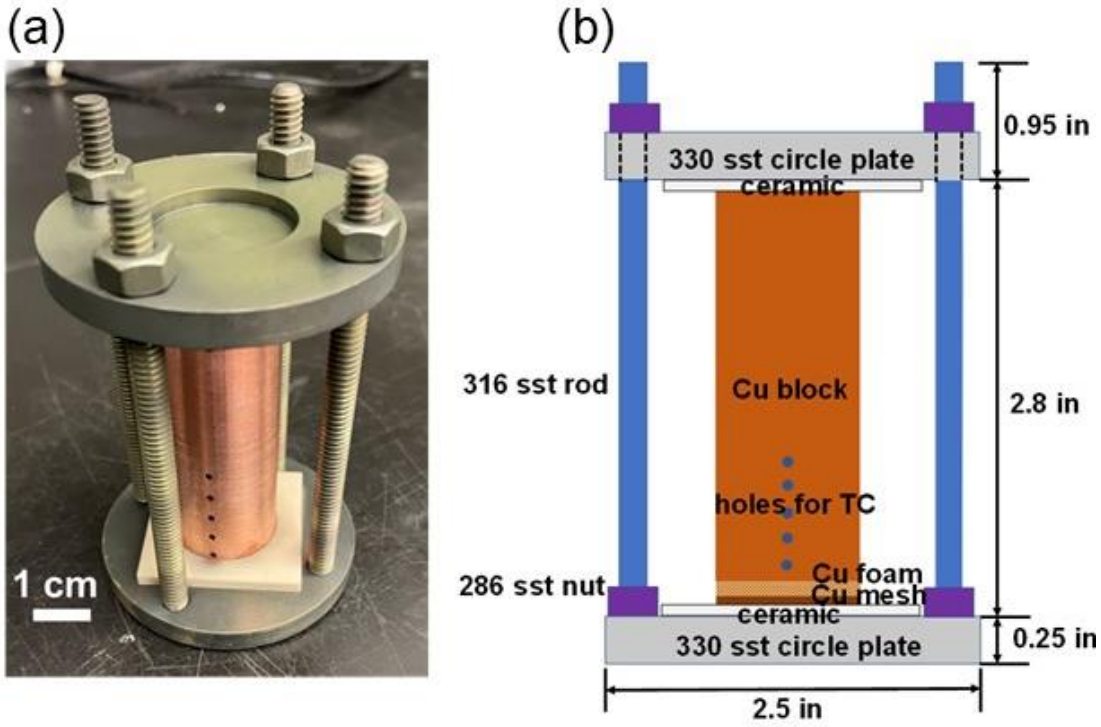

Figure 19: An image (a) and a schematic (b) of the diffusion bonding assembly. The copper block, the copper foam, and the copper mesh are aligned in between two thin ceramic pieces, which are clamped together by two stainless-steel plates in parallel.

A schematic and an image of the diffusion bonding assembly are shown in Figure 19(a) and (b). The copper block condenser substrate, the copper foam, and the copper mesh with the same diameter (1 inch) were aligned one by one in between two thin (0.125 inch-thick) ceramic plates, which have a shallow dent of 1.02-inch-diameter circle in the middle for the copper parts to fit in. The use of the ceramic plates is to prevent possible diffusion bonding from occurring between the stainless steel and the copper. The slightly larger diameter of the dents on the graphite plates is to accommodate the thermal expansion of the copper parts under the high

temperature during the diffusion bonding process. The two ceramic plates with the copper parts between them are clamped together by a pair of customized stainless-steel parallel clamps with a given torque which is equivalent to a pressure of ~14 MPa. Different materials for the parallel plates, the threaded rods, and the nuts were chosen to prevent potential diffusion bonding between parts made of the same materials. Ultra-high-temperature 330 stainless steel parallel plates, super-corrosion-resist 316 stainless steel threaded rods, and high-strength A286 stainless steel hex nuts are used in the diffusion bonding assembly. 20 inch-lbs torque was applied on the nuts, which could generate a uniform clamping pressure (~14 MPa) over the stainless-steel parallel plates, holding the three copper parts together during the diffusion bonding process.

The overall assembly was placed inside a 3.5-in-diameter tube furnace for the diffusion bonding process, as shown in Figure 20(a). The furnace was purged and kept under forming gas (Airgas, 5% hydrogen, 95% argon) throughout the bonding procedure. The furnace was heated from room temperature to a maximum temperature of 780°C at a ramp rate of 6 °C/min and maintained at T_{max} for 5 hours, then allowed to cool to room temperature over the course of ~4 hours. During the diffusion bonding process, the controlled temperature inside the furnace is plotted against time as shown in Figure 20(b).

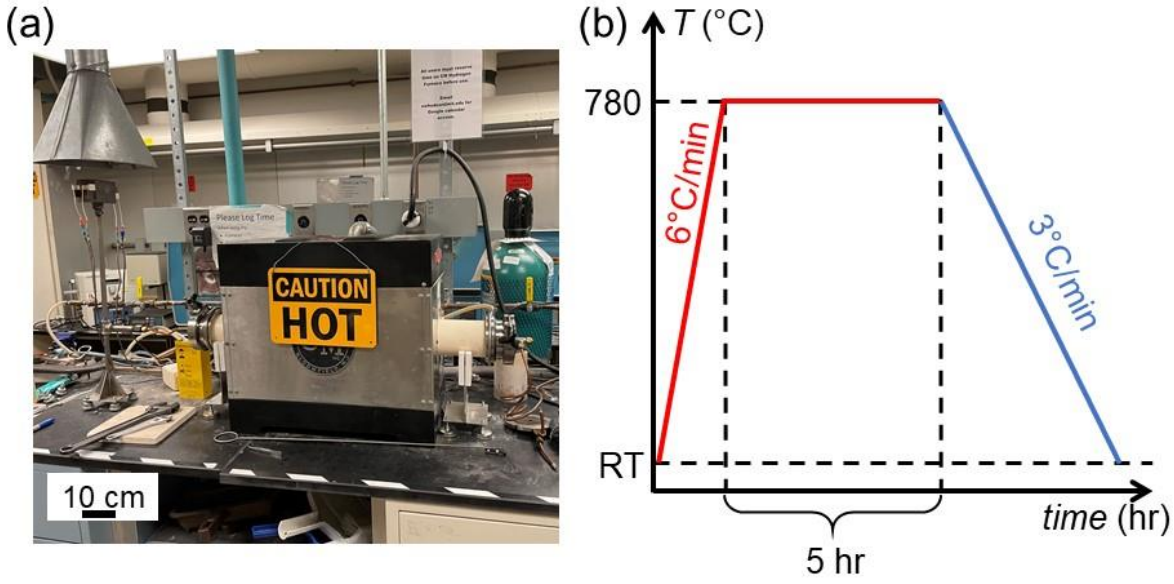

Figure 20: (a) The high-temperature furnace where the diffusion bonding is conducted following a well-controlled ramp-up and ramp-down temperature cycle shown in (b).

An SEM image of a diffusion bonded hierarchical copper composed of a 1500-mesh-size copper mesh and a copper foam with ~200 μm pore size is shown in Figure 21. The structures of

the copper mesh and the copper foam were bonded together without noticeable structure deformation except a few broken pores on the mesh layer. Because the copper mesh is ultra-thin (5 μm, which is great for vapor transport through the mesh), it is almost inevitable that a few of the mesh pores would get damaged during the clamping and the diffusion bonding process. As we will discuss later, these broken pores can shift the flooding scenarios and significantly degrade the heat transfer performance of the thin-film condenser.

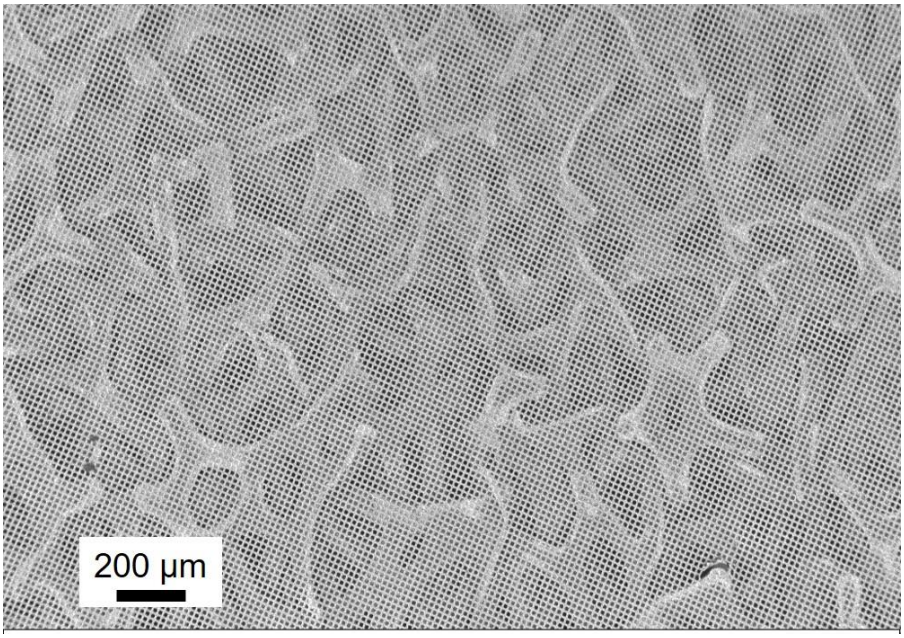

Figure 21: SEM image of a diffusion bonded hierarchical copper composed of a 1500 mesh size copper mesh and a copper foam with ~200 μm pore size.

3.1.4 Coating Procedure

Vapor deposition using FAS ((heptadecafluoro-1,1,2,2-tetrahydrodecyl) trimethoxy silane) has been applied in the literature[98] to form a conformal hydrophobic coating on metal surfaces and was adopted in the current study.

The details of the coating procedure are as follows. First, we cleaned the copper foam samples with acetone, ethanol, isopropanol, and water in sequence to remove potential hydrocarbon contaminants. Then, we dipped the sample in to an HCL solution (2 M) for 30 seconds to remove oxides. After the samples are rinsed with water and dried with nitrogen, we put them into a sealed bottle. Along with the porous copper samples, we also put 800 μL of FAS in toluene solution (5 V%) into a small beaker, which sat beside the samples to be coated. The sealed bottle was placed in an over at 100°C for 3 hours, during which the FAS was coated onto

the porous copper sample via vapor phase deposition. Finally, the samples were taken out of the furnace and cooled down to room temperature in the fume hood. A schematic of the coating process illustrated in Figure 22(a).

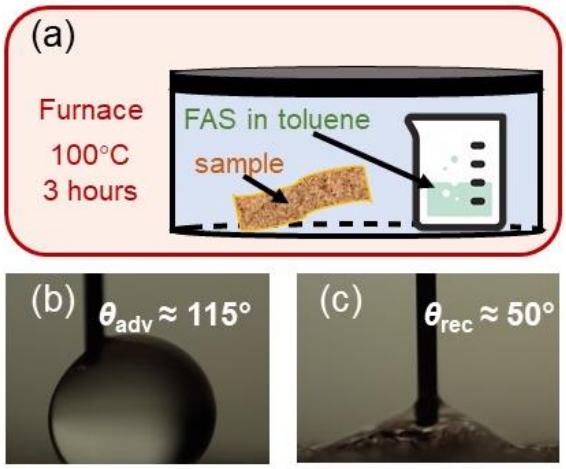

Figure 22: (a) Vapor deposition of FAS ((heptadecafluoro-1,1,2,2-tetrahydrodecyl) trimethoxy silane) in a furnace and (b) the resulting wetting performance on a flat copper sample. A high contact angle hysteresis was observed.

We characterized the wetting behavior of a coated flat copper piece using DI water with a goniometer in the lab. As shown in Figure 22 (b) and (c), after the vapor deposition of FAS, the copper became hydrophobic with an advancing contact angle of ~115°. However, the contact angle hysteresis was measured to be high with a receding contact angle of 50°. This may be caused by the residue from the protective peel-off film that was attached to the mirror-like polished copper piece that we chose to use. The material we used for making the hierarchical sample did not come with any protective films and should not have these residue concerns.

As we will discuss in section 3.4, a completely hydrophobic coating is proven to be undesired in a thin-film condenser, as water would not fill into the hydrophobic wick layer and instead burst out through the mesh pores. Therefore, we developed a method to selectively coat the diffusion bonded hierarchical copper to make the mesh layer hydrophobic, while maintaining the wick hydrophilic. The resultant surface is therefore biphilic.

Figure 23 shows the biphilic coating procedure conducted on a hierarchical copper sample and the SEM images of the sample prior and after the biphilic coating. To selectively coat the structure, we first cleaned the hierarchical copper with acetone, ethanol, isopropanol,

followed by 15 minutes of argon plasma cleaning. Right after the plasma cleaning, we protected the wick layer (copper foam) with a photoresist with low viscosity by dipping the edge of the sample into a photoresist reservoir. The photoresist was observed to climb up against gravity inside the porous copper foam up to ~0.5-inch-high over 2 minutes, as shown in Figure 23 (a)-(c). Rotating the circular surface while keeping its edge dipped into the photoresist allowed us to obtain complete wicking of the protective photoresist into the wick layer. Then, photoresist-covered hierarchical copper was baked in a 110 °C furnace for 10 minutes to remove the solvent in the photoresist and to solidify the photoresist.

An SEM image of a photoresist-protected hierarchical copper right after the curing step is shown in Figure 23 (d). As shown in the SEM image, the majority of the copper foam was successfully covered by the photoresist, with a portion of the copper foam unprotected. This should not be a concern as long as there were connected regimes on the coper foam surface that would stay hydrophilic. Note that as shown in Figure 23 (d), many of the copper mesh pores were coated with the photoresist as well, though the top surface of the mesh remained clean of photoresist. This is because the solvents in the photoresist evaporated before the photoresist reached the top of the mesh layer. To ensure the top surface of the mesh layer is coated as hydrophobic, this surface needs to be exposed rather than covered by the photoresist. Any additional photoresist that was deposited on top of the mesh layer should be removed. To do this, we plasma cleaned the photoresist-protected sample with oxygen for 20 minutes under a power of 20W. This step could help remove any photoresist residue on the top of the mesh layer. Post the O_2 plasma cleaning, the sample underwent the FAS coating procure, followed by 5 minutes of ultrasonic cleaning with acetone. After the ultrasonic cleaning, the photoresist that was protecting the wick layer surface got washed away, exposing the hydrophilic wick surface with the topmost mesh surface being hydrophobic. An SEM image of the same hierarchical copper after the last step of acetone ultrasonic cleaning is shown in Figure 23 (e), which confirms that there was no residue of photoresist on the surface.

Two types of photoresists with similar viscosities were used in the study (i.e., AZ 3312, and 1:1: volume ratio of SPR700-1 in isopropanol). Mixing the photoresist with isopropanol was found to help improve the photoresist's fluidity (thus the photoresist could wick further in the wick layer) while maintaining the protective functionality of the photoresist.

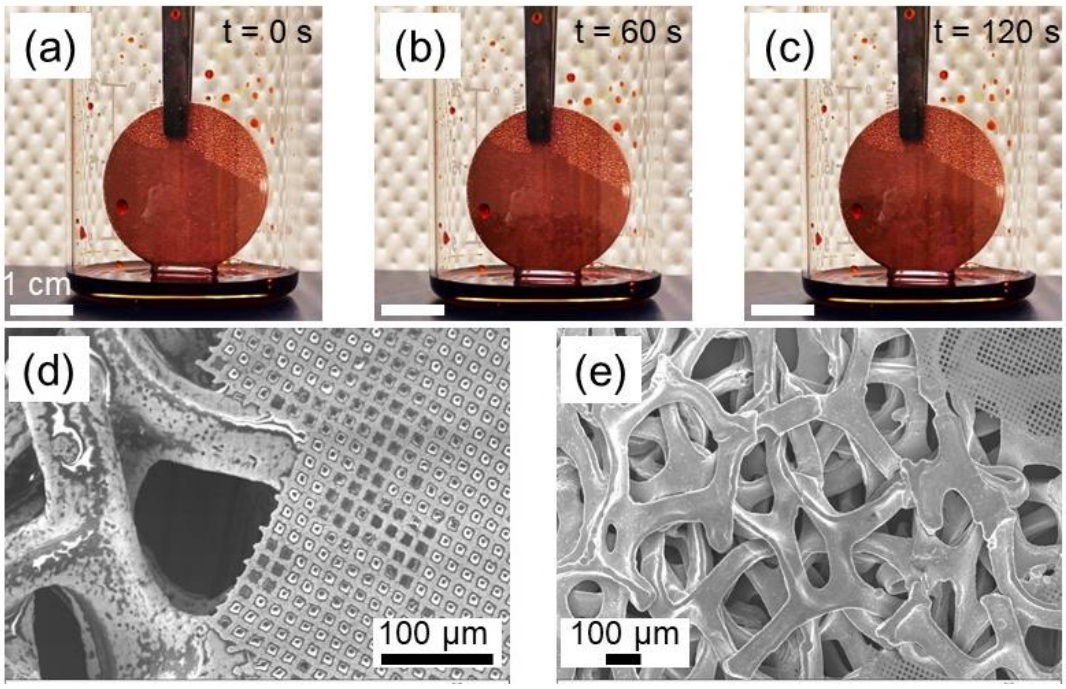

Figure 23: Biphilic coating procedure relies on a photoresist to protect the hydrophilic wick layer. (a)-(c): time lapse images of photoresist wicking into a hierarchical copper sample piece. Note that the top right portion of this sample piece was purposely left as copper foam (no mesh coverage) for comparing the photoresist coverage on the mesh and the wick layer under the SEM. (d) SEM image of the hierarchical copper right after the photoresist curing. (e) SEM image of the same hierarchical copper after the post-coating ultrasonic cleaning.

3.2 Simplified Modeling and Performance Prediction

Upon the selection of the membrane material and the wick material for the proof-of-concept experiment, we revisited the heat and mass transfer model for its application to the hierarchical copper sample that we fabricated. Due to the special geometry of the mesh layer, i.e., ultra-small thickness (5 µm) with a relatively large mesh pore size (11 µm), and considering the advancing contact angle of 115° given by the FAS coating, the mass transport resistance through the membrane (mesh) is negligible and the heat transfer modal can be significantly simplified. With the simplified heat transfer model, we predicted the heat transfer performance of the hierarchical copper samples we fabricated.

3.2.1 Heat Transfer Model for Hierarchical Copper Sample

During the condensation of the hierarchical copper samples, the pores of the copper mesh layer would be partially filled with condensed water due to the curvature of the liquid-vapor interface and the shallow geometry of the mesh layer. At the given advancing contact angle of 115°, the curvature height of a liquid-vapor interface pinned at the bottom of the 11 μm mesh pore can be estimated by $H_{\mathrm{curv}} = \frac{d_{\mathrm{p}}}{2}\tan(\theta_{\mathrm{adv}} - \frac{\pi}{2})$~2.6 μm. Depending on the depth of the deposition of the hydrophobic coating into the mesh pores, this curvature can be either inside the mesh pore (in the case of complete hydrophobic coating) or extruding out of the mesh pore (in the case of biphilic coating), with a total thickness of the water filled mesh layer to be no more than 7.6 μm, which is almost more than 20x smaller than the thickness of the copper foam layer, even though the copper mesh and the copper foam have similar porosity and their effective thermal conductivity should be similar on the order of magnitude. As a result, we simplified our analytical model for the heat and mass transfer process based on the following assumptions:

(1) The resistance for mass transfer and viscous pressure loss through the mesh pores is negligible due to the large pore size and the small mesh thickness;

(2) Any water condensed on top of the copper mesh would be merged into the liquid-filled membrane pores;

(3) Heat transfer through the membrane and the wick follows steady-state 1D conduction;

(4) The thermal resistances given by the mesh layer can be neglected and the thermal resistance of the wick layer can be calculated using its effective thermal conductivity.

A schematic of the simplified heat transfer model for the hierarchical copper and the corresponding thermal resistance network are shown in **Error! Reference source not found.**.

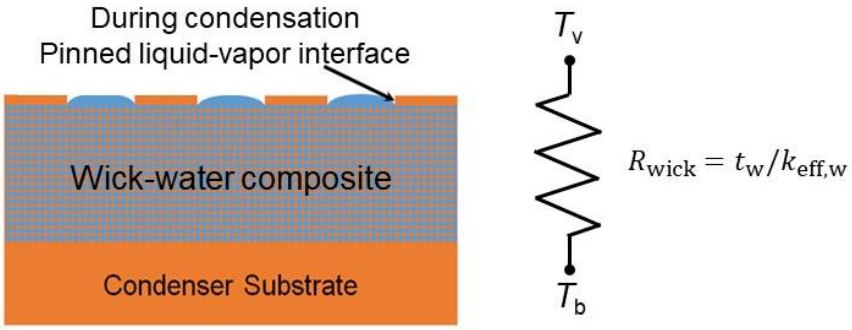

Figure 24: Schematic of the hierarchical copper surfaces during condensation and the correspondingly simplified thermal resistance network.

One key parameter in calculating the conduction heat transfer through the wick is its effective thermal conductivity. Due to the porous nature of the wick structure, conventional techniques for determining the thermal conductivity of a homogeneous material such as the laser flash method[99] could not be used. Direct measurements of a material's thermal conductivity through 1D conduction heat transfer such as in the guarded-hot-plate method[100] often rely on the substantial temperature drop across the materials. However, the small thickness and the high thermal conductivity of the copper in the copper foams that we chose would cause big uncertainties in the temperature drop measurement and the heat flux measurement if characterized with a 1D conduction heat transfer apparatus.

Many analytical or empirical models have been developed for predicting the effective thermal conductivity of porous metal wicks of different geometries[97,101-104]. Table 3 summarizes some of the commonly used models for estimating the effective thermal conductivity of various porous metal wicks.

Table 3: Commonly used models for estimating the k_{eff} of porous media.

Model	Expression for k_{eff}	Application
Maxwell	$k_{\text{eff,Maxwell}} = \dfrac{2 + k_l/k_s - 2\phi(1 - \frac{k_l}{k_s})}{2 + \frac{k_l}{k_s} + \phi(1 - k_l/k_s)}$	A continuous solid phase containing a random dispersion of randomly sized spheres of liquid. Assuming no interaction between liquid spheres.
Maxwell	$k_{\text{eff,Maxwell}} = \dfrac{2 + k_s/k_l - 2\phi(1 - \frac{k_s}{k_l})}{2 + \frac{k_s}{k_l} + \phi(1 - k_s/k_l)}$	A continuous phase of liquid surrounding a random dispersion of randomly sized spheres of solid. Assuming no interaction between solid spheres.

Bruggeman	$\phi\frac{k_s - k_{\text{eff,Bruggeman}}}{k_s + 2k_{\text{eff,Bruggeman}}} + (1-\phi)\frac{k_l - k_{\text{eff,Bruggeman}}}{k_l - k_{\text{eff,Bruggeman}}} = 0$	A random distribution of both phases with consideration of interactions among metal particles with a percolation threshold of ~33%
Rayleigh	$k_{\text{eff,Rayleigh}} = \frac{\beta - \varepsilon}{\beta + \varepsilon}k_l$ where $\beta = (1 + \frac{k_s}{k_l})/(1 - \frac{k_s}{k_l})$ $\varepsilon = 1 - \phi$	A dispersion consisting of a square array of uniform cylinders.
Effective medium theory modified [105]	$k_{\text{eff,EMT}} = \frac{1}{4}\left[(3\phi - 1)k_l + [3(1-\phi) - 1]k_s + \sqrt{[(3\phi - 1)k_l + (3(1-\phi) - 1)k_s]^2 + 8k_s k_l}\right]$ can be simplified to $k_{\text{eff,EMT}} = \frac{(2-3\phi)}{2}k_s$ when $k_s \gg k_l$	Isotropic, heterogeneous materials where both the phases form continuous media
Li and Peterson[106]	$k_{\text{eff,stag mesh}} = 1.42\frac{k_s(M \times d)^2}{t}2n_{layer}d$	Staggered copper screen mesh
Upper limit	$k_{\text{eff,max}} = (1-\phi)k_s + \phi k_l$	Parallel thermal resistance
Lower limit	$k_{eff,\text{min}} = \left[\frac{(1-\phi)}{k_s} + \frac{\phi}{k_l}\right]^{-1}$	Thermal resistance in series

Considering the anisotropic geometry of the copper foam we chose to use, and its similarity to the shape of staggered copper screen meshes, we adopted Li and Peterson's model to estimate the effective thermal conductivity of the copper foams[106]

$$k_{\text{eff,stag mesh}} = 1.42 \frac{k_s (M \times d)^2}{t} 2 n_{layer} d \tag{23}$$

where M in the mesh number (i.e., number of meshes per meter of distance), d is the diameter of the copper wire, t is the thickness of the overall material, k_s is the thermal conductivity of the solid phase (for copper, $k_s = 390$ W/mK), and n_{layer} is the number of layers of copper mesh that are staggered together.

With SEM images, we approximated the copper foam structures to staggered copper meshes with mesh number and copper wire diameter directly measured from the SEM images. n_{layer} was derived by dividing the total weight of the copper foam samples by the weight of a single-layer copper mesh with the approximated mesh number and copper wire diameter. With the measured M, d, and the derived n_{layer}, the effective thermal conductivities of the three copper foams we chose were calculated with equation (23). The results are compared to the effective thermal conductivities calculated by the Maxwell equation (upper bound and lower bound). All the effective thermal conductivities we calculated are within the upper and lower bounds given by the Maxwell model, as shown in **Error! Reference source not found.Error! Reference source not found.**

We experimentally characterized the permeability of these copper foams after a heating and compressing process under the same condition as the diffusion bonding process. The results for the measured permeability and the estimated effective thermal conductivity for the three copper foams are shown in Table 4.

Table 4: Geometric and thermal properties of the three copper foams.

Copper foam ID	Porosity	Thickness	Permeability after diffusion bonding	Effective thermal conductivity
1	70%	220 μm	2×10^{-11} m^2	42.3 W/mK
2	85%	180 μm	5×10^{-11} m^2	18.4 W/mK

3	50%	130 μm	1×10^{-11} m^2	95.7 W/mK

3.2.2 Model Prediction

Heat flux and fluid flow were analytically solved under an environmental condition with vapor temperature of 35°C and surface subcooling up to 5°C. This vapor condition is normally seen in steam power plant condensers and we aimed to achieve this condition during our experiments. Conventional filmwise condensation heat transfer predicted by the Nusselt model was used as the benchmark. Figure 25(a), (b), and (c) show the model-predicted heat transfer performance of the three hierarchical copper samples: (1) copper mesh covered copper foam #1, (2) copper mesh covered copper foam #2, and (3) copper mesh covered copper foam #3. All three hierarchical copper structures share the same type of copper mesh, which is a 1500 mesh size, 5 μm thick copper mesh as shown in Figure 16. The y-axis on the left shows heat flux, and

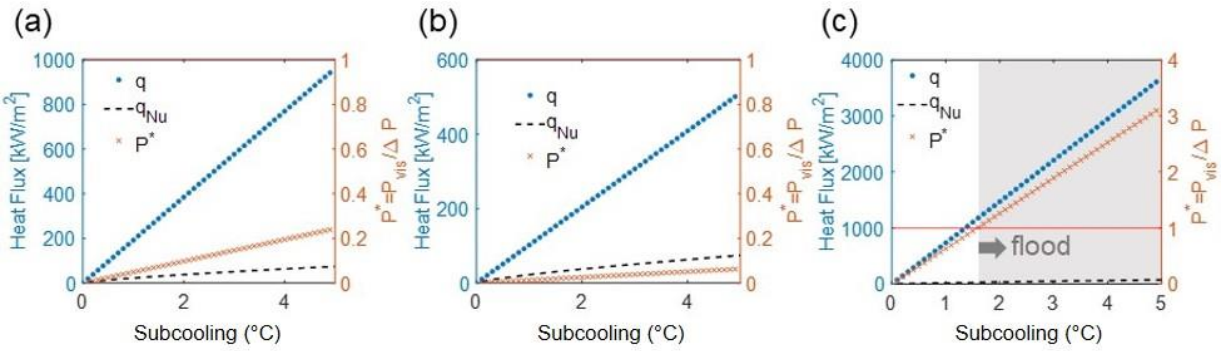

the y-axis on the right shows the flooding criteria P^*, which is the ratio of the viscous pressure loss for condensate to travel through the wick layer and the capillary pressure given by the hydrophobized mesh pores. In order to prevent flooding from happening, we should operate the experiments within the regime $0<P^*<1$. Otherwise, flooding would occur and greatly deteriorate the heat transfer performance of the condensing surface. The flooding regime is shown in gray.

All three hierarchical copper samples are expected to outperform the traditional filmwise condensation, as shown by the blue lines (representing heat transfer performance of the hierarchical copper surfaces) and the dashed black lines (representing filmwise condensation heat transfer predicted by the Nusselt model). In addition, for all three hierarchical copper

Figure 25: Heat transfer enhancement given by the three hierarchical copper surfaces predicted by the analytical model.

samples, the heat transfer enhancement as compared to the filmwise condensation is expected to get more significant as the subcooling increases, until the surface is flooded. This is because during the capillary-driven thin film condensation on a hierarchical copper surface, the major thermal resistance generated by the water-filled copper wick layer stays as constant as the wick-water composite film is confined at a fixed thickness by the hydrophobic copper mesh. Therefore, condensation heat flux increases linearly with the increasing surface subcooling, until the surface gets flooded. On the other hand, during a traditional filmwise condensation, condensate film gets thicker with increasing subcooling. The analytical model solved by Nusselt shows that film thickness in a filmwise condensation is proportional to the surface subcooling to the ¼ power. As a result, heat flux in a filmwise condensation only increases proportional to the surface subcooling to the power of ¾. Consequentially, with increasing subcooling, the enhancement over a filmwise condensation offered by the hierarchical copper thin-film condenser gets larger.

As shown in Figure 25(a) and (b), flooding would not occur for the range of subcooling considered (up to 5 °C). This is contributed to the relatively high permeabilities of these two copper foams as well as the relatively moderate heat flux given by these two hierarchical copper surfaces. The sample made of copper foam #1 has a slightly larger thickness, but has a much lower porosity. As a result, the effective thermal conductivity of the first hierarchical copper sample is higher than that of the second hierarchical copper sample, resulting in a better heat transfer performance. The higher heat flux and lower permeability of the first sample as compared to the second one induces a higher flooding criterion P^* in the first sample as compared to the P^* in the second sample. At the maximum subcooling considered (5 °C), the first hierarchical copper is expected to achieve a heat flux of 960 W/m^2, which is ~ 13x enhancement as compared to the conventional filmwise condensation predicted by the Nusselt model. At the same subcooling, the second hierarchical copper is expected to achieve 510 W/m^2, which is ~7x enhancement as compared to the conventional filmwise condensation.

In comparison, flooding is predicted to occur at subcooling of 1.6°C on the third hierarchical copper sample, as indicated by the out-of-range value for P^*. This is due to the ultra-high heat flux enabled by the high thermal conductivity of the copper foam and the low permeability of the third copper foam. As we can see in this case, the effective thermal conductivity and the permeability of the wick layer can be conflicting: a wick with a more

packed metal skeleton usually has a higher effective thermal conductivity but a lower permeability. Regardless of the early flooding predicted on the third hierarchical copper sample, it is predicted that this sample can achieve a heat transfer enhancement over 45x before flooding occurs.

3.3 Experimental Setup and Data Acquisition

We characterized the condensation heat transfer performance of the hierarchical copper samples under pure vapor conditions in a controlled environmental vacuum chamber in which the total pressure can be maintained at ~ 5.2 kPa, which corresponds to a saturated vapor temperature of 34 °C. A detailed description of the chamber setup and the data acquisition procedure is as follows.

3.3.1 Environmental Vacuum Chamber and Experimental Procedure

We experimentally characterized the heat transfer performance of the fabricated sample surfaces in a controlled environmental chamber. The front and back sides of the chamber are shown in Figure 26(a) and (b). A Pirani gauge was installed on the chamber to accurately monitor the chamber pressure under the pumping process. Another pressure transducer with a higher measurement range (Omega, MMA030V5B3MB0T3A5CE) was installed on the chamber for vapor pressure measurement. A vacuum-sealed stainless-steel canister was used as a water reservoir that was surrounded by a resistance heater controlled by a PID controller. During condensation experiments, the reservoir was set at a temperature that is slightly higher than the boiling point of water under 1 atm to prevent any leaking of non-condensable gases (NCGs) from the lab environment into the boiler. PID-controlled heaters were attached to each side of the chamber to maintain a constant chamber temperature. These heaters were covered by thick insulation materials to prevent heat loss to the lab environment. A thermal couple probe was installed at the vapor inlet port inside the chamber to monitor the inlet vapor temperature. This temperature was found to be 1-2 °C higher than the universal vapor temperature measured inside the chamber. This is due to the transient state of the hot vapor diffusing from the vapor inlet pipe into the chamber. Dry-bulb and wet-bulb temperatures inside the chamber were measured by an exposed thermocouple probe and a paper towel-covered thermocouple probe, as shown in the

schematic in Figure 26(d). These two temperatures should be close to each other when the chamber is operating under a steady-state, pure vapor environment.

The sample copper block was installed onto a test rig inside the chamber, as shown in Figure 26 (c) and (d). An array of five thermocouple probes were inserted into the Teflon-insulated copper block along its length to monitor the temperature distribution along the copper block. Assuming 1D (linear) conduction heat transfer, heat flux flowing through the copper block could be extracted from the temperature measurements by Fourier's law. The linear fit for the temperature measurements had an R^2 value of over 99% for each measurement throughout our experiments, indicating that the assumption of linear conduction was valid and heat transfer through the block walls was negligible. The back side of the copper block was cooled with chilled water provided by an external chiller (Fisher Scientific, Isotemp II), and the front side of the copper block, where the hierarchical copper surface was attached, was served as the condenser surface. The temperature at the condenser surface (right below the copper wick layer) was determined by extrapolating the linear temperature distribution along the copper block measured by the thermocouple array.

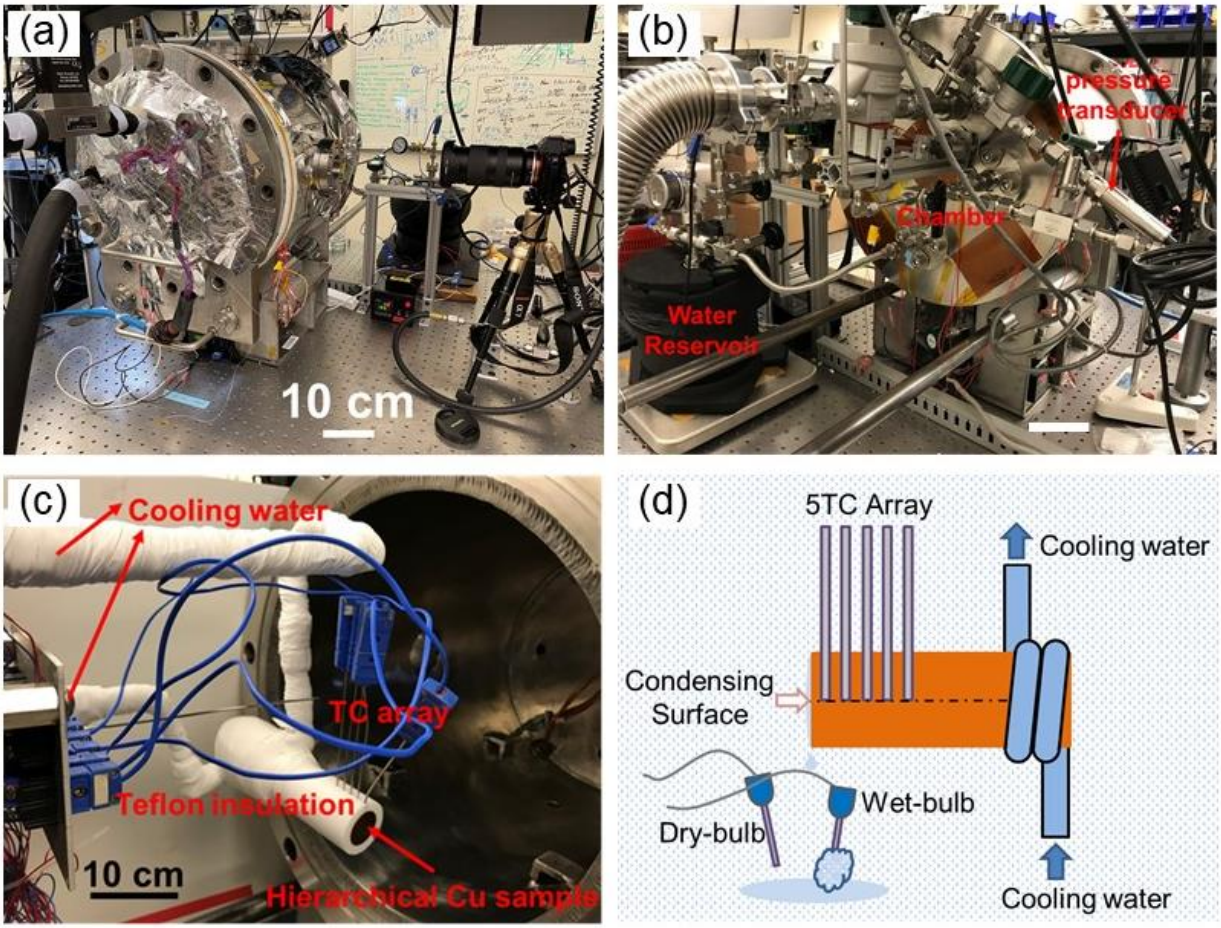

Figure 26: Experimental setup and the condensation test rig assembly. The front and the back sides of the environmental vacuum chamber are shown in (a) and (b). (c)-(d): Image and schematic of the condensation test rig assembly inside the chamber.

Non-condensable gases (NCGs) are known to degrade condensation heat transfer of vapor significantly even with a 0.5% concentration[107]. Therefore, careful procedures have been taken to eliminate the existence of NCGs in the vacuum chamber throughout the experiments. Before every experiment, we pre-pumped the chamber overnight with the condensation testing rig (except the sample) inside the chamber and with wall heaters on to maintain a chamber temperature of 32°C. This would allow the potential outgassing materials inside the chamber (e.g., the plastic connections of the thermocouple probes, the paper towel used for covering the wet bulb thermocouple, and the insulation materials) to outgas thoroughly overnight. Usually, chamber leak rate of 7Pa/hr at an absolute vapor pressure of 0.5Pa could be achieved after overnight pumping. After the overnight pre-pumping, a clean sample was mounted onto the condensation test rig and the chamber door was closed. The vacuum pump would pump the

chamber pressure below 0.5Pa to eliminate non-condensable gases (NCGs), before any experiments. Right before the experiments, the vapor reservoir was degassed thoroughly to eliminate any NCGs inside it.

3.3.2 Data Acquisition and Error Propagation

Following removal of NCGs, pure, degassed vapor was introduced into the chamber from a heated, temperature-controlled water reservoir (as shown in Figure 26 (b)), and allowed to condense on the condenser surface. The vapor pressure inside the chamber was manually maintained at a constant (~5.2 kPa) by opening the valve on the reservoir and measuring the pressure by the pressure transducer. When at steady state, dry bulb and wet bulb temperatures agreed with each other with a discrepancy falling under the uncertainty of the thermocouple readings (0.15 °C). Condensation heat flux flowing through the copper block and the surface temperature of the condensing surface were extracted from the temperature distribution measured by the five-thermocouple array using Fourier's law Then, surface subcooling was determined by subtracting the measured vapor temperature by the extracted surface temperature, and the experimentally measured condensation heat transfer coefficient was determined by dividing the heat flux by the surface subcooling.

The surface subcooling was controlled by tuning the chiller temperature while maintaining a constant vapor pressure inside the chamber. We typically collected 5 data points for each sample. We started with a chiller temperature of 5°C, and increased its temperature by 5°C at each data point until the chiller reached 25°C. For each data point, we waited for over 20 minutes to make sure steady state was reached, and the data point was collected by averaging measurements over a period of 5 minutes. Visualization of the condensation development was achieved through a viewing window on the chamber, where a camera was placed towards the viewing window outside the chamber.

Figure 27 shows a schematic of linear fitting of the five temperatures measured by the five-thermocouple array inserted into the sample side wall. The least square approximation of linear functions was used to linearize the temperature measurements from the five-thermocouple

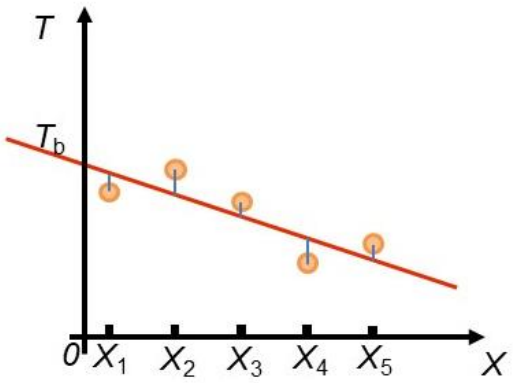

Figure 27: representation of the least square linear fitting for the five thermocouple readings as a function of their locations.

array. Setting the location of the front surface of the condenser as x = 1, using the five temperatures T_i $(i = 1, 2, 3, 4, 5)$ measured at the five locations $X_i (i = 1, 2, 3, 4, 5)$, the extracted slope and the temperature at the front surface ($T(X = 0)$) given by the least square method are

$$\frac{dT}{dX} = -\frac{5\sum_{i=1}^{5} X_i T_i - \sum_{i=1}^{5} X_i \sum_{i=1}^{5} T_i}{5\sum_{i=1}^{5} {X_i}^2 - (\sum_{i=1}^{5} X_i)^2} \tag{24}$$

$$T(X = 0) = \frac{(\sum_{i=1}^{5} T_i - A\sum_{i=1}^{5} X_i)}{5} \tag{25}$$

The condensation heat flux can be derived from Fourier's law:

$$q = -k\frac{5\sum_{i=1}^{5} X_i T_i - \sum_{i=1}^{5} X_i \sum_{i=1}^{5} T_i}{5\sum_{i=1}^{5} {X_i}^2 - (\sum_{i=1}^{5} X_i)^2} \tag{26}$$

The surface subcooling can be calculated by:

$$\Delta T = T_{v,dry-bulb} - \frac{(\sum_{i=1}^{5} T_i - A\sum_{i=1}^{5} X_i)}{5} \tag{27}$$

where $T_{v,dry-bulb}$ is the vapor temperature directly measured by the dry bulb thermocouple. This temperature was in great agreement with the wet bub temperature during the experiments.

For each variable U_i shown in equations (26) and (27), uncertainty was analyzed by accounting for both the precision error and the bias error:

$$U_i = \sqrt{(P^2 + B^2)} \tag{28}$$

where B is the precision error. All thermocouple probes were calibrated to a high-accuracy RTD prior to the experiments. The precision error for the temperature measurement was 0.15 °C. P is the bias error, which can be represented by the standard deviation of the measurements.

$$P = \sigma_Y = \left[\sum_{i=1}^{N}\left(\frac{\partial Y}{\partial X_i}\sigma_{X_i}\right)^2\right]^{1/2} \tag{29}$$

The overall uncertainty for the heat flux measurement and the subcooling measurement can be calculated by integrating the uncertainties of each variable in the expressions for the heat flux and for the surface subcooling

$$U_Y = \left[\sum_{i=1}^{N}\left(\frac{\partial Y}{\partial X_i}U_i\right)^2\right]^{1/2} \tag{30}$$

3.4 Experimental Results and Discussion

Condensation with hierarchical copper surfaces fabricated with different types of copper foams was conducted in the environmental vacuum chamber. We first observed surface flooding on a completely hydrophobic hierarchical sample and a biphilic hierarchical sample, but successfully proved the concept of thin-film condensation on a biphilic, microchannel-assisted hierarchical copper, which highlights the importance of surface permeability in flooding prevention. Next, we experimentally characterized the heat transfer performance of three biphilic, microchannel-assisted hierarchical copper surfaces. The discrepancy between the modeling result and the experimental data and strategies for flooding prevention will be discussed at the end of this session.

3.4.1 Visualization Study

As a proof-of-concept study, we fabricated hierarchical copper surfaces based on the first copper foam shown in Table 4. According to the model prediction shown in Figure 25(a), at surface subcooling up to 5 °C, this hierarchical copper sample would be able to generate up to 13x higher heat transfer performance as compared to the conventional filmwise condensation without flooding. A photo and an SEM image of this hierarchical copper surface are shown in Figure 28.

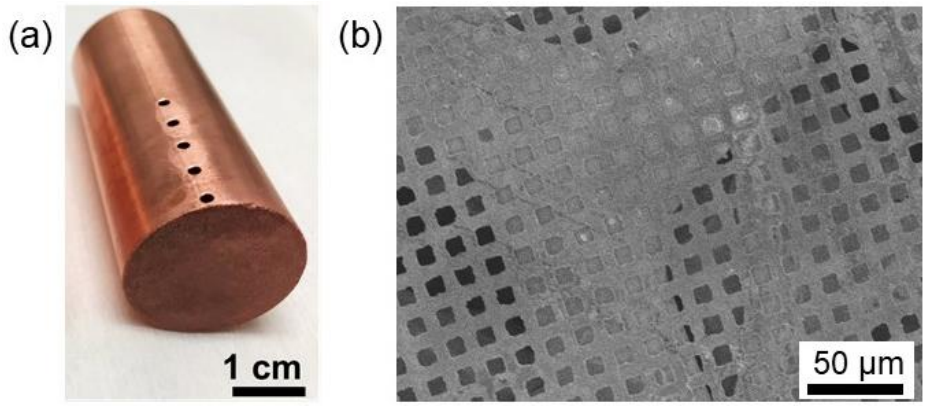

Figure 28: (a) a hierarchical copper surface made by diffusion bonding a 1500 mesh size copper mesh with a copper foam with a porosity of 70% is shown in photo (a). The top surface geometry of such a hierarchical copper structure was characterized through an SEM as shown in (b).

For the visualization study, we functionalized the sample surfaces completely by depositing a fluorinated silane (trichloro (1H,1H,2H,2H-perfluorooctyl)-silane, Sigma-Aldrich) following a well-developed procedure[108]. This hydrophobic coating gives an advancing contact angle of 120° of water on a smooth surface. The hydrophobic coating is not robust in a long term; however, its lifetime (~1-2 days) is long enough to be tested in a vacuum chamber and experimentally validate the model prediction. The resulted sample surfaces exhibit over 100° contact angle with water, demonstrating hydrophobicity. The sample was loaded into the chamber right after the coating procedure to avoid contamination from the air in the lab environment[109].

As a comparison to the completely hydrophobic sample, a biphilic hierarchical copper sample functionalized with the same hydrophobic coating but only with the mesh layer being coated was fabricated following the biphilic coating procedure described in section 3.1.4. The comparison between this and the previous samples indicates the significant impact of having a hydrophilic wick layer, as shown by the time-lapse images taken on the two samples during the condensation of pure vapor inside the chamber.

Figure 29 shows a series of time-lapse images of the completely hydrophobic hierarchical sample during the pure vapor condensation inside the environmental vacuum chamber at a chiller temperature of 5°C and a transient vapor temperature that eventually stabilized at ~34°C. Unexpectedly, we observed droplets shedding off the sample surface from various locations of

the sample throughout the condensation process. Figure 29(a) shows the dry sample surface right before we introduced water vapor into the chamber (T = 0 s). When we first introduced vapor into the chamber, condensation was initiated everywhere on the sample surface, as shown by the randomly distributed tiny droplets in Figure 29(b). As condensation continued on the sample surface, the individual droplets shown in the early stages grew, coalesced with each other, and finally shed off the surface due to gravity, as shown in Figure 29(c)-(d). We also observed that, unlike conventional dropwise condensation, the droplets atop the mesh layer not only grew by absorbing water vapor surrounding it, but also seemed to absorb water from the wick layer beneath the mesh layer. As a result, we did not observe thin-film condensation behavior on the completely hydrophobic hierarchical sample. One potential reason for the dropwise pattern we observed on this sample is that the homogeneous hydrophobic coating deposited on the copper foam could impede the transport of the condensed water inside the wick layer. Instead of confining a condensate-metal composite during condensation, the wick layer in the completely hydrophobic surface may have vapor trapped inside the pores of the hydrophobic wick layer, impeding condensate flow and heat transfer.

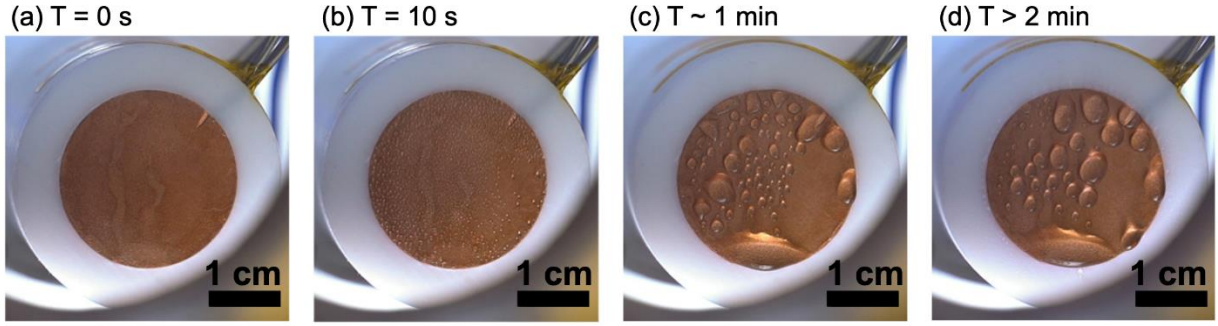

Figure 29: Time-lapse images of the completely hydrophobic hierarchical sample composed of the 1500 mesh size copper mesh and the 70% porosity copper foam during the pure vapor condensation at a chiller temperature of 5°C and a transient vapor temperature that eventually stabilized at ~34°C.

Maintaining a hydrophilic wick layer could address the concern of having a hydrophobic wick layer that repels condensate. An additional benefit of having a hydrophilic wick layer is that the condensation nucleation barrier for the hydrophilic surface is much lower than the hydrophobic surface[110]. Therefore, water would first condense and fill the pores of the hydrophilic wick layer in the case of a biphilic hierarchical copper structure.

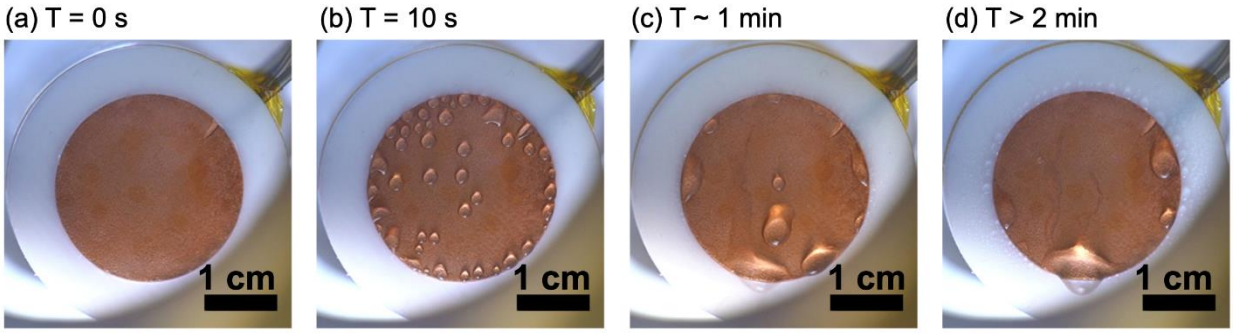

Figure 30: Time-lapse images of the biphilic hierarchical sample composed of the 1500 mesh size copper mesh and the 70% porosity copper foam during the pure vapor condensation at a chiller temperature of 5°C and a transient vapor temperature that eventually stabilized at ~34°C.

Error! Reference source not found. shows a series of time-lapse images of the biphilic hierarchical cooper sample during the pure vapor condensation inside the environmental vacuum chamber at a chiller temperature of 5°C and a transient vapor temperature that eventually stabilized at ~34°C. Note that the only difference between this and the previous sample is the wettability of the copper foam layer.

Interestingly, condensation behavior on the biphilic hierarchical copper was different from that on the completely hydrophobic hierarchical copper from the beginning. Here, time is set to zero right before vapor was introduced into the system, as shown in **Error! Reference source not found.**(a). Right after we introduced water vapor into the environmental chamber, as shown in **Error! Reference source not found.**(b), we observed scattered droplets emerging on the top of the mesh layer, with a much lower density than what we observed during the beginning of condensation on the completely hydrophobic hierarchical copper sample. The distribution of the droplets we observed on the biphilic hierarchical copper is different from the random distribution of condensed droplets we normally would see on a dropwise surface. As shown in **Error! Reference source not found.**(c), after droplets formed on the biphilic hierarchical copper surface, they grew up independently with minimal coalescence and shed off the surface from several fixed locations. These locally bursting droplets seem to be local flooding incidents on the biphilic hierarchical copper before a connected liquid film was formed inside the copper foam layer. As the condensation continued, the biphilic hierarchical copper surface eventually reached a steady-state condensation, as shown in **Error! Reference source**

not found.(d). At this stage, the majority of the top surface of the mesh layer became free of droplets, though a few bursting spots remained throughout the condensation.

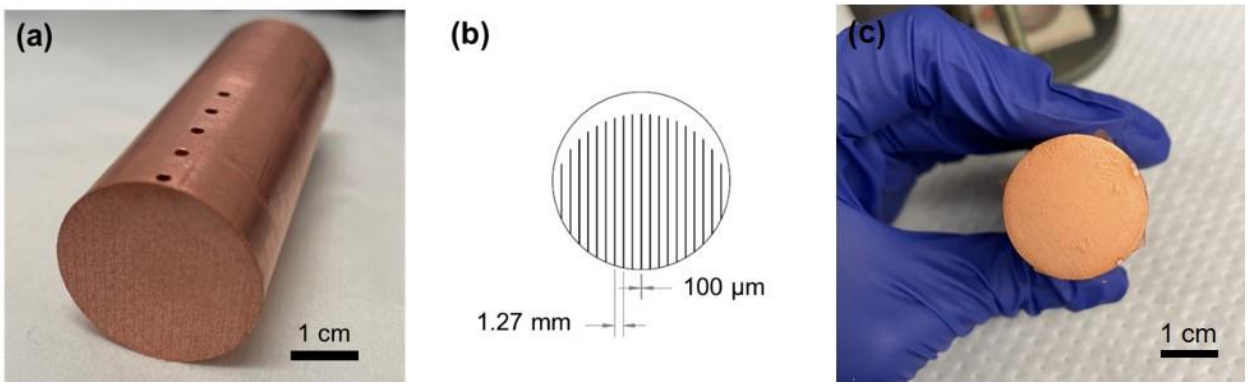

Figure 31: Fabrication of microchannel embedded, hierarchical copper. (a) 19 microchannels of 100 μm width and 100 μm height were machined into the copper foam layer at an evenly distributed spacing of 1.27mm. A schematic of the channel geometry is shown in (b). The top edge of the copper foam was intentionally left as channel-free to avoid potential drainage of condensed liquid from the top of the surface. (c) After the machining of the microchannels, the copper foam bonded sample went through another round of diffusion bonding under high temperature and pressure inside a forming gas furnace to bond the top layer 1500 mesh size copper mesh onto the foam layer.

Although the permeability of the first type copper foam ($2\times10^{-11}m^2$) was high enough to prevent flooding at low surface subcooling, flooding could potentially occur at local defects such as broken mesh pores, which were hardly evitable during the fabrication process. In order to further prevent flooding incidents, we machined microchannels on the copper foam layer to facilitate condensate drainage with a channel depth of 100 μm. as shown in Figure 31 (a). The microchannels were machined using a carbide slitting saw. Only one end of the microchannels was machined all the way to the edge of the sample to ensure directional condensate flow. The channel width, channel depth, and distance between the microchannels were selected as 100 μm, 100 μm, and 1.27 mm, respectively. These dimensions were chosen based on the tools available and were used for a test study. Further modeling for optimizing the design of the microchannels will be discussed as anti-flooding strategies at the end of this chapter.

Figure 32 shows the condensation of pure water vapor developed on a biphilic hierarchical copper sample with microchannels. Note that the only difference between this sample and the second sample discussed above is the existence of the 19 microchannels. Figure 32 (a) shows that the sample was completely dry and kept under a vacuum right before we

introduced water vapor into the chamber. The same experimental procedure as the previous experiments was repeated on this sample. Similar to the biphilic hierarchical copper sample, this biphilic hierarchical copper sample with microchannels also showed local flooding/bursting droplets with relatively low density at the very beginning of the experiments, as shown in Figure 32 (b). As condensation continued (after the first minute), the bursting droplets that we saw at the beginning of condensation grew and shed off the surface, with a decreasing density of the bursting droplets on the surface over time, as shown in Figure 32 (c). The decreasing density of bursting droplets on the surface over time can be explained by the development of interconnected water film formed inside the wick layer. During the very beginning of the condensation, the copper foam wick might be partially filled with water patches with voids in between, resulting in local bursting spots on top of the hydrophobic meshes. As condensation continued, an interconnected water film was formed inside the copper foam wick, which could absorb any condensed droplets that were forming on the hydrophobic mesh layer.

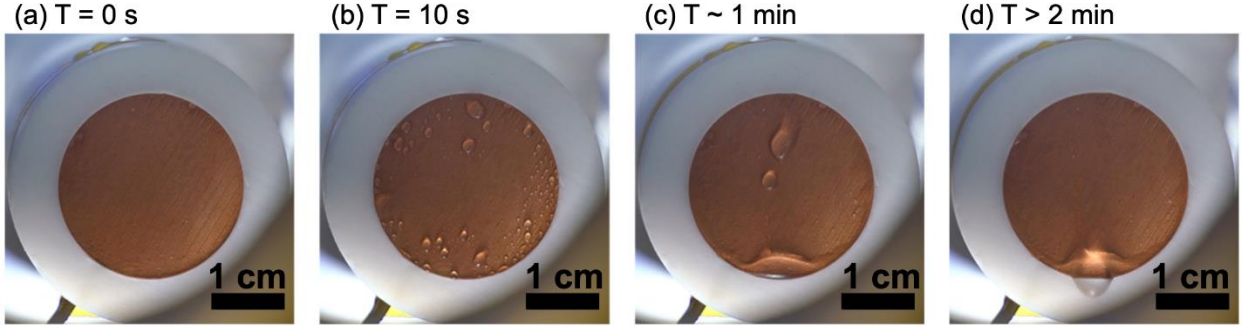

Figure 32: Time-lapse images of the microchannel-embedded, biphilic hierarchical sample composed of a 1500 mesh size copper mesh and a 70% porosity copper foam during the pure vapor condensation at a chiller temperature of 5°C and a transient vapor temperature that eventually stabilized at ~34°C.

Even more interestingly, across the surface of the hierarchical copper with microchannels, the capillary force generated at the hydrophobic copper mesh layer was able to keep most of the surface free of droplets, proving the concept of a thin-film condensation, as shown in Figure 32 (d). This was achieved by having the microchannels as additional exit ports. The flow resistance through the microchannels was less than the bursting pressure of most broken mesh pores. Therefore, even though there were local defects on the copper mesh layer, we did not observe many bursting droplets on the top of the surface. In addition, the condensed

water was found to exit from either the local bursting spots or the bottom of the channels, leaving the surface from the bottom regardless of the direction of the channels

One thing to note is that we found that the hierarchical surfaces hydrophobized by the trichloro(1H,1H,2H,2H-perfluorooctyl)-silane exhibited an ultra-high contact angle hysteresis, with a receding contact angle approaching zero, which can induce droplet pinning and impede shed-off of any bursting droplets on the surface. Therefore, we only used this type of hydrophobic coating for the visualization study, and for the rest of the study, we switched to another hydrophobic coating (FAS, as mentioned in section 3.1.4) that has been known in the literature to deliver a better surface modification with an easier approach.

3.4.2 Heat Transfer Measurements

Before testing the heat transfer on the hierarchical copper samples, a flat copper sample was tested inside the environmental vacuum chamber under an identical vapor condition and followed the same experimental procedure as we would do to the hierarchical copper samples. Prior to the experiment, the flat copper sample was cleaned as follows. First, the sample was ultrasonically cleaned in acetone, followed by ethanol and isopropanol rinse. After the isopropanol evaporated away, the sample was dipped into a 2M solution of hydrochloride acid (HCL) in water for at least a minute to remove copper oxides. Next, the sample was taken from the HCL solution into a beaker of DI water to rinse away the HCL residue, followed by a series of rinses with acetone, ethanol, and isopropanol. Finally, the sample was dried with pure nitrogen gas and plasma cleaned by argon plasma for 15 minutes to remove hydrocarbons.

Condensation experiments were conducted with a constant vapor condition (P_v ~5.2 kPa, T_v ~34 °C) that was manually controlled by a vapor inlet valve. Five data points were taken at five different subcools achieved by the following five chiller temperatures: 5°C, 10°C, 15°C, 20°C, and 25°C. At each subcool, we waited for at least 20 minutes to ensure a steady state before data collection. As shown in Figure 33(a), we observed a continuous liquid film on the flat copper surface during condensation, demonstrating filmwise condensation. The condensed water film accumulated at the bottom of the condensing surface and eventually shed off under gravity. Figure 33(b) shows the heat flux measured at the flat copper sample under different subcools as compared to the expected heat flux for filmwise condensation calculated by the Nusselt model. The red data points represent experimental data, and the blue curve represents the

Nusselt model prediction. A good agreement was achieved between the Nusselt model and the experimentally measured heat transfer data for filmwise condensation, validating the reliability of the chamber condition and the experimental procedure.

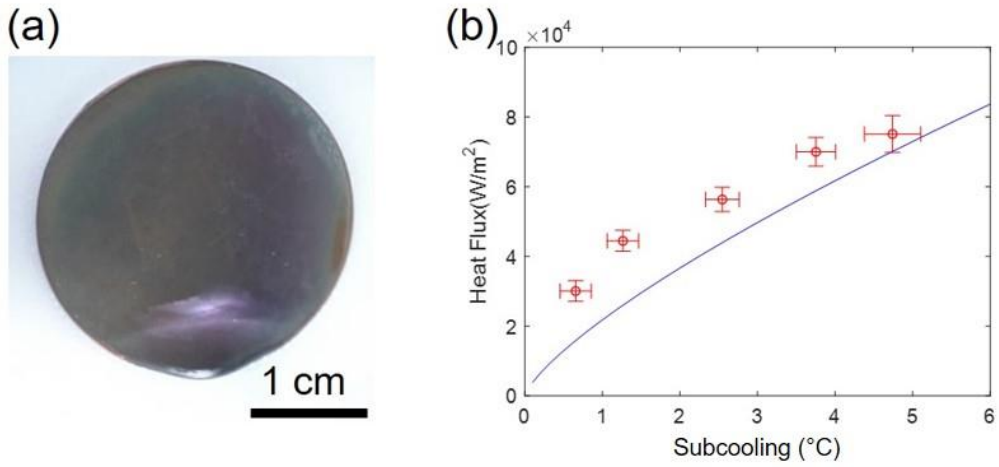

Figure 33: Filmwise condensation on a flat copper sample. (a) A continuous liquid film was observed on the flat copper surface during condensation. (b) Experimental data measured on the filmwise sample shown in red data points were in good agreement with the Nusselt model represented by the blue curve.

Following the validation of the chamber condition and the experimental procedure with filmwise condensation, we fabricated and experimentally characterized the heat transfer performance of three different hierarchical copper samples, as detailed in Table 5. Heat transfer coefficient, the ratio of heat flux over subcooling, which is a direct indicator of surface's heat transfer performance, is abbreviated as HTC in the remaining content of the thesis.

Table 5: Surface designs for biphilic, microchannel-assisted hierarchical copper.

Sample ID	Wick material	Membrane material	Coating	Microchannel (W×H)	Model prediction
HierCu-1	Copper foam #2: 0.85 porosity, $5\times10^{-11}m^2$ permeability, 180 μm thickness	1500 mesh size copper mesh: 5 μm thickness,	Biphilic coating with FAS: hydrophobic mesh	3 evenly spaced 100 μm ×150 μm microchannels	No flooding, 5-7x HTC enhancement in the 5°C

		48% porosity	+hydrophilic foam		subcooling range
HierCu-2	Copper foam #3: 0. 50 porosity, $1\times10^{-11}m^2$ permeability, 130 μm thickness			3 evenly spaced 100 μm ×100 μm microchannels	Flooding at 1.6°C subcool, over 30x HTC enhancement before flooding
HierCu-3				7 evenly spaced 100 μm ×100 μm microchannels	

Inspired by the visualization study, we incorporated microchannels into the surface designs for all three samples. Adding microchannels to the hierarchical copper has two major effects. First, as we demonstrated in the proof-of-concept study, microchannels can help prevent flooding incidents by improving the permeability of the copper foam. Second, as we mentioned in Figure 14, channels can decrease the thermal conductivity of the surface, as they can split the surface into disconnected islands and cause non-uniform temperature distribution across the x-y plane of the surface, inducing a thermal resistance network that is close to the in-series mode. In order to leverage the anti-flooding advantages of microchannels while minimizing their impacts on the effective thermal conductivity of the copper foam wick, we minimized the number of channels to 3 in the first sample, considering that model predicts this surface to have a pretty high flooding threshold (Figure 25 (b), P^*<0.2 at subcooling of 5°C). The second and the third sample were fabricated with the same copper foam with a high density. The model predicts that they would flood at subcooling of 1.6°C if there is no microchannel to improve the permeability of the copper foam (Figure 25 (c), P^* exceeds1 at subcooling of above 1.6 °C). Therefore, we fabricated two versions of the microchannels for the two samples made of the dense copper foam: one with 3 microchannels and the other with 7 microchannels. All the microchannels were engraved into the copper foam layer with even spacings. The smallest dimension we could make on the microchannels was 100 μm, which was limited by the size of the carbide slitting saw we used to machine the channels. We minimized the channel width to 100 μm to minimize its impact on the effective thermal conductivity of the surface. For the channel depth, we

approached the thickness of the copper foams to obtain the best permeability out of the channels. Considering the different thicknesses of the two copper foams, we machined microchannels with a depth of 100 μm in #2 copper foam and 150 μm in #3 copper foam. All three samples share the same membrane layer (the 1500 mesh size copper mesh) and the same coating method (biphilic coating with FAS), as detailed in Table 5. For simplicity, we name the three samples shown in Table 5 as HierCu-1, HierCu-2, and HierCu-3 for the rest of this section.

For the condensation experiments with all three samples, we followed the identical experimental procedure as what we did in the filmwise condensation experiment, except that rather than doing an argon plasma clean on the sample before the experiment, the hierarchical copper samples were installed onto the test rig right after the biphilic coating step. Following the experimental procedure, we constantly held a 5.2 kPa vapor pressure environment throughout the experiments and started with a 5°C chiller, and then moved the chiller temperature up to 25°C with a 5°C increase at each data point. The condensation heat flux and surface subcooling were extracted from temperature measurements at steady states. The maximum heat flux we could obtain was limited by the cooling capacity of the chiller. Therefore, with an enhanced condensation heat transfer, we would expect a lower surface subcool.

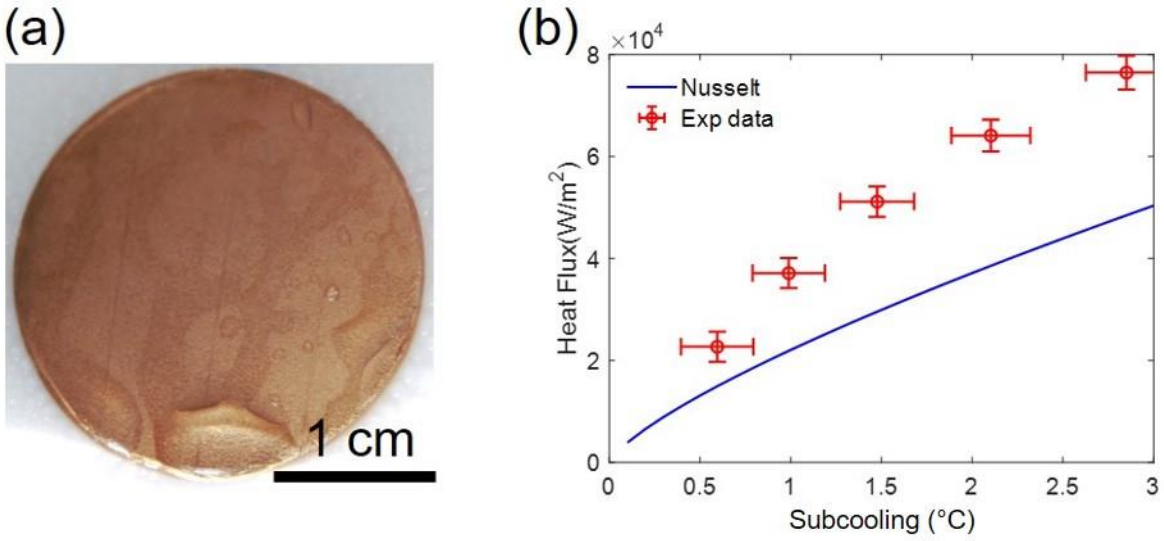

Figure 34: Condensation on the HierCu-1 sample. (a) We observed partial flooding on the surface during steady state condensation. (b) experimental data measured on the sample shown in red data points exceeds filmwise condensation by 51%-58%.

Figure 34 shows the experimental results of condensation heat transfer on the HierCu-1. Similar to what we observed in the visualization study, the surface was covered with scattered droplets when the vapor was first coming into the chamber; as condensation developed into a steady state, the condensation pattern on the sample surface became stabilized. As shown in Figure 34 (a), we observed partial flooding on the HierCu-1 surface during a steady state. Specifically, areas above the microchannels remained day while the space between these areas were covered by water patches. The flooding incident significantly degraded the heat transfer performance of the surface, as shown in Figure 34 (b). Although the model predicts a 5-7x heat transfer enhancement as compared to filmwise condensation, here we measured a roughly 1.5-1.6x heat transfer enhancement as compared to filmwise condensation predicted by the Nuseelt model. Note that with the same vapor condition and chiller temperature, subcooling measured on the hierarchical copper sample was lower than the subcooling measured on the flat copper sample shown in Figure 33(b), indicating a heat transfer enhancement. We also noticed that even though we switched the coating materials, the FAS coating also had a large contact angle hysteresis of water on the mesh layer, inducing serious pinning of the condensed water on top of the mesh layer which degraded heat transfer performance.

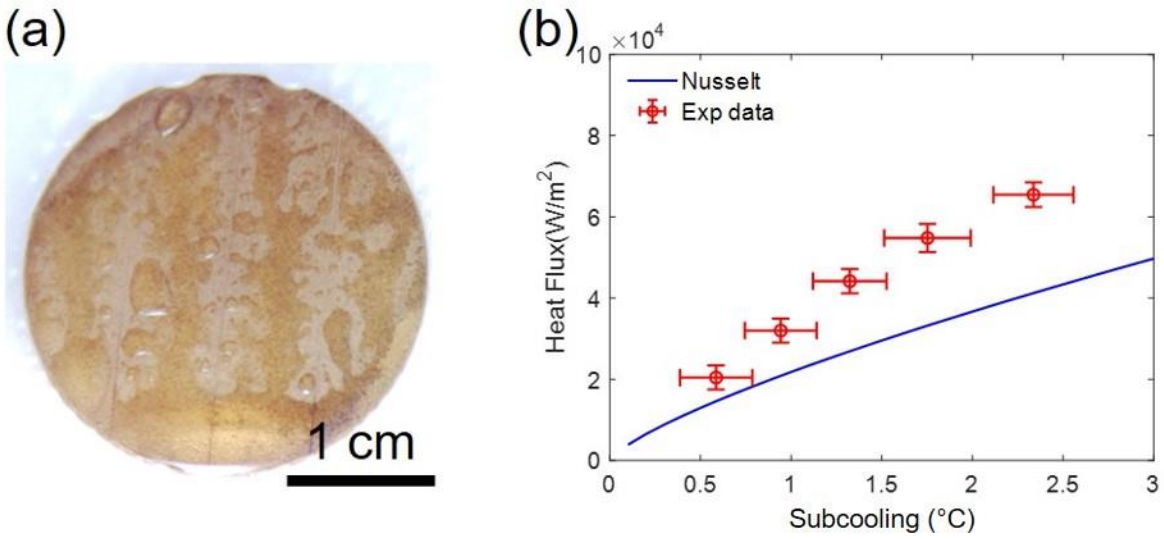

Figure 35: Condensation on the HierCu-2 sample. (a) Observed partial flooding on the surface during steady state condensation. (b) Experimental data measured on the sample shown in red data points exceeds filmwise condensation by 37%-56%.

Figure 35 shows the experimental results of condensation heat transfer on the HierCu-2. Similar to HierCu-1, condensed water first formed scattered droplets on top of the mesh surface and eventually formed a steady pattern as shown in Figure 35(a). HierCu-2 has the same number of microchannels as HierCu-1, although here a denser copper foam with a 5x lower permeability is used as the wick layer. Due to the high effective thermal conductivity and the ultra-thin wick layer, the model predicts that this surface could achieve a heat transfer enhancement of above 30x as compared to the filmwise condensation—before the flooding occurs at 1.6°C. During the experiment, we started with the highest subcooling around 2.5°C under the limitation of the chiller capacity. We observed severe flooding on the surface at this subcool. As shown in Figure 35 (a), while the surface area above the three microchannels remained dry, the majority of the rest of the surface was covered by water patches, which significantly degrades heat transfer performance. Not surprisingly, we obtained a heat transfer enhancement that was much lower than what the model predicted. As shown in Figure 35 (b), the heat transfer performance measured on the HierCu-2 sample was roughly 37%-56% better than the filmwise condensation predicted by the Nusselt model. Note that even though HierCu-2 has a much higher effective thermal conductivity and a thinner structure than HierCu-1, it did not achieve a heat transfer performance that was better than HierCu-1. This is mainly due to the more severe flooding that

occurred on HierCu-2, where the flooded water patches dominated the thermal resistance and significantly degraded heat transfer.

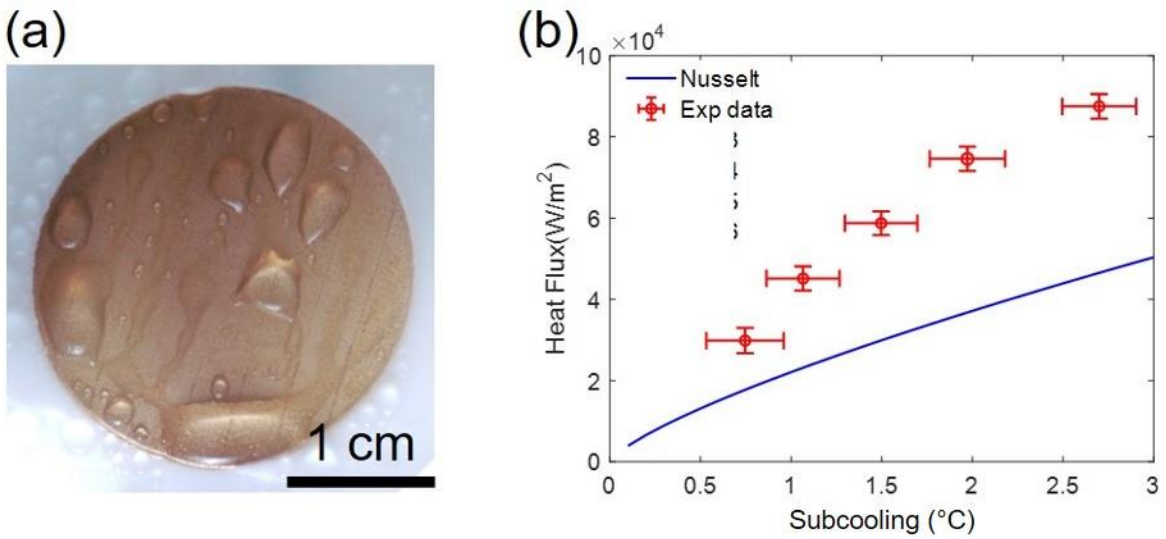

Figure 36: Condensation on the HierCu-3 sample. (a) We observed partial flooding on the surface during steady state condensation with a slightly less flooding coverage than HierCu-2. (b) experimental data measured on the sample shown in red data points exceeds filmwise condensation by 68%-88%.

Error! Reference source not found. shows the experimental results of condensation heat transfer on the HierCu-3. Similar to the previous two samples, condensed water first formed scattered droplets on top of the mesh surface and eventually formed a steady pattern as shown in Error! Reference source not found.(a). HierCu-3 uses the same copper foam as Hier-2 with the only difference being having 7 microchannels instead of 3 microchannels in HierCu-2. With the increased number of microchannels, we expect a high permeability and higher flooding threshold for the HierCu-3. Starting with a 5°C chiller and a 5.2kPa vapor pressure, the HierCu-3 surface arrived at surface subcooling of ~2.7°C, which is within the flooding regime predicted by the model for the same hierarchical copper structure without microchannels. As shown in Error! Reference source not found.(a), we observed partial flooding on the surface during steady state condensation with a slightly less flooding coverage than HierCu-2. This is contributed by the additional microchannels that improved the permeability of the copper foam layer and consequently elevated the flooding threshold. However, with the local flooding on top of the mesh surface, heat transfer enhancement given by this surface was significantly reduced. As shown in Figure 36(b), we measured a heat transfer enhancement over filmwise condensation by

roughly 70-90%. The improved heat transfer performance as compared to that of HierCu-2 highlights the importance of microchannels in flooding prevention on these capillary-driven thin-film condensers.

3.4.3 Discussion and Strategies for Flooding Prevention

As we observed in the condensation heat transfer experiments, all three samples were impeded by surface flooding to obtain great heat transfer enhancement. When flooding occurs on a hierarchical copper sample, the water patches pinning on top of the flooded areas, forming thick water patches with film thickness up to the capillary length of water (2.7mm). The flooded water patch dominates the thermal resistance and significantly degrades heat transfer. Here, we developed a simple heat transfer model to understand the impact of surface flooding on the heat transfer performance of hierarchical copper surfaces. Assuming a parallel pathway for the heat to go through either the flooded area or the unflooded area, the thermal resistance network of the overall system can be represented in the schematic shown in Figure 37. Note that the parallel thermal resistance assumption gives the theoretical upper bound for the effective thermal conductivity of the composite surface. Therefore, this model provides an upper bound of the heat transfer performance of a flooded hierarchical copper surface.

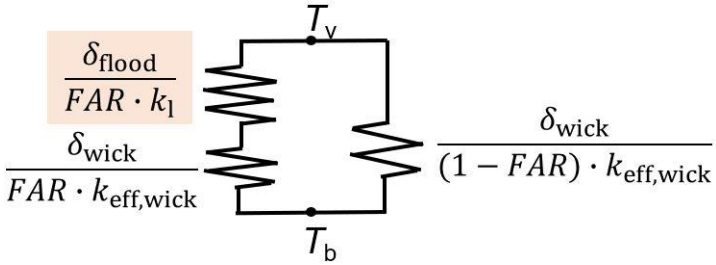

Figure 37: Thermal resistance network of a flooded hierarchical copper surface based on a parallel thermal resistance assumption. The resistance highlighted in the light orange box is the term associated with the flooded water patch. FAR: flooded area ratio, which is the ratio of flooded area to the total surface area.

Figure 38 shows the modeling result for the heat transfer performance and the effective thermal conductivity of hierarchical copper as a function of flooded area ratio and flooded film

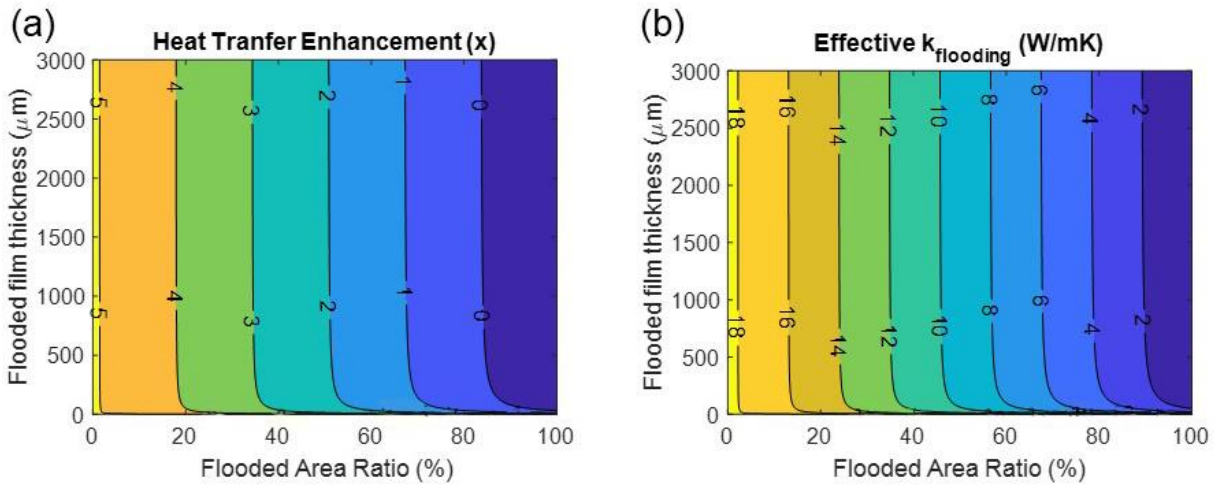

Figure 38: Modeling results for (a) the heat transfer performance and (b) the effective thermal conductivity of a flooded HierCu-1 as a function of flooded area ratio and flooded film thickness.

thickness, with HierCu-1. Although the hierarchical copper surface is hydrophobized, its large contact angle hysteresis induces pinned water patches with a film thickness of up to the capillary length of water. Here, we swept the flooded film thickness up to the capillary length of water and the flooded area ratio from 0 to 100%. Figure 38(a) shows the heat transfer enhancement as compared to filmwise condensation as a function of the flooded area ratio and the flooded film thickness. The flooded area ratio has a dominant effect on the heat transfer performance of the flooded HierCu-1 except in the case when the flooded film is ultra-thin (below 100 μm). This is due to the extremely low thermal conductivity of water (0.6 W/mK) as compared to the copper foam wick (18.4 W/mK for HierCu-1). When more than half of the surface is covered with flooded water, the heat transfer enhancement provided by the HierCu-1 sample drops below 2x. For the same reason, the effective thermal conductivity of the flooded hierarchical copper drops significantly as the flooded area ratio increases from zero to one, as shown in Figure 38 (b).

To prevent flooding from occurring, we need to understand the cause of it. Although our model predicts that HierCu-1 should be free of flooding under the given experimental conditions, we still observed flooding on it. We suspect two major reasons for the flooding incident to occur before the model predicted threshold, as shown in Figure 39.

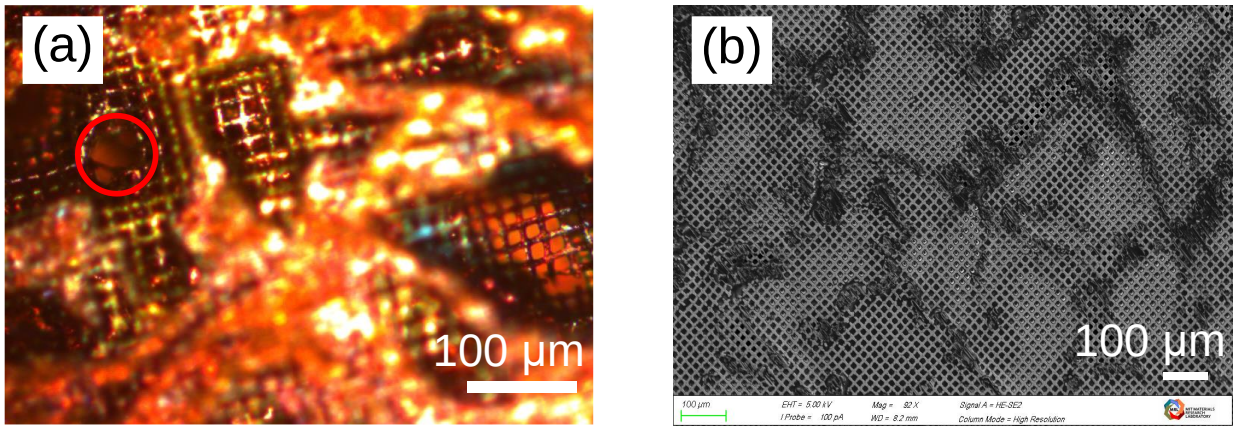

Figure 39: Optical image and SEM image showing defects on the hierarchical surface: (a) broken mesh pore highlighted in the red circle; (b) overfilled photoresist as shown by the dark regions.

Figure 39(a) shows a broken mesh pore found on a hierarchical copper sample. Due to the fragility of the ultra-thin copper mesh, it is almost inevitable that some mesh pores got damaged during the diffusion bonding prosses where a pressure of 14 MPa was applied to the surface. Broken mesh pores would result in a larger effective pore size at the damaged area, which remarkably shifts the flooding regime, as the capillary pressure driving force provided by the mesh layer scales with $1/d_p$.

Figure 39(b) shows the overfilled photoresist after the photoresist wicking step in the biphilic coating process. Due to the rough surface of the copper foam and the small thickness (5 µm) of the copper mesh, the photoresist was deposited unevenly across the hierarchical surface. Although the oxygen plasma has been proven to be a reliable method to remove photoresists, there might still be some photoresist residue staying on the top of the mesh layer after the oxygen plasma cleaning. These photoresist residues could protect the local mesh wire from being hydrophobized, and result in local coating defects that would not be able to generate capillary pressure driving force and would induce severe liquid pinning on the surface.

Figure 40 shows the model prediction for the flooding criterion P^* as a function of surface subcooling and the number of connected broken mesh pores for (a) HierCu-1 and (b)HierCu-2/HierCu-3, neglecting the effects of microchannels on the permeability and the effective thermal conductivity of the copper foam. With increasing numbers of connected broken pores, P^* increases and induces earlier flooding. The impact of broken pores on the P^* gets more

significant with surfaces with lower thermal resistances, as the condensation heat flux are higher on these surfaces, challenging the surfaces' resistance to flooding.

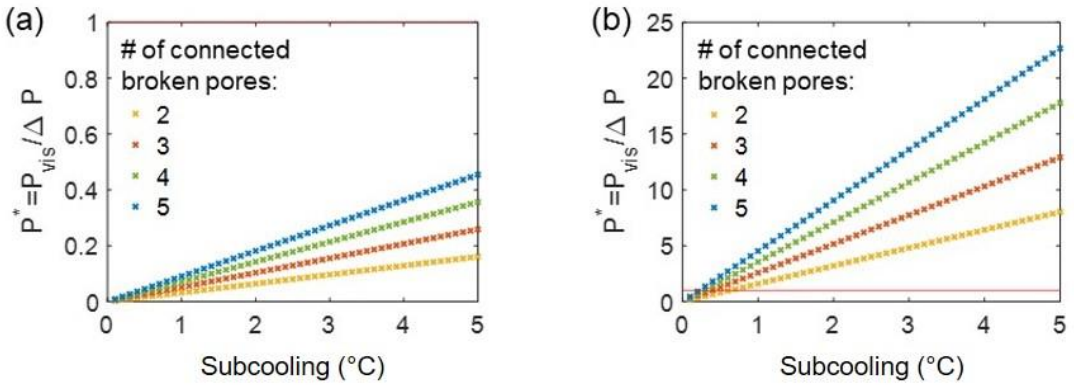

Figure 40: Flooding criterion P^* as a function of surface subcooling and the number of connected broken mesh pores for (a) HierCu-1 and (b)HierCu-2/HierCu-3, neglecting the effects of microchannels on the permeability and the effective thermal conductivity of the copper foam.

There are two direct ways to improve the capillary-driven thin-film condenser surfaces to be more resilient against flooding: (1) improving the permeability of the wick layer, and (2) increasing the capillary pressure driving force generated by the membrane layer.

As we have observed in the condensation experiment with the hierarchical copper sample, microchannels can help with fast drainage of the condensate, especially in the case where the hydrophobic membrane has defected pores which could cause local flooding/bursting out of the membrane. A few considerations should be taken when adding microchannels to the capillary-driven condenser design. First and foremost, microchannels can decrease the effective thermal conductivity of the metal wick layer as it would break the continuous connection of metal network for efficient thermal transport. Therefore, the addition of microchannels should be just enough to prevent the membrane from flooding. When designing the geometry of the microchannels, the viscous pressure loss associated with the process of the condensed water traveling through the porous wick and finally exiting through the microchannel (the route is shown as the blue arrow in Figure 41) should be less than the viscous pressure loss the same amount of condensed water would experience if it exits directly through the metal wick layer without traveling through the microchannel (route as shown in the red arrow in Figure 41).

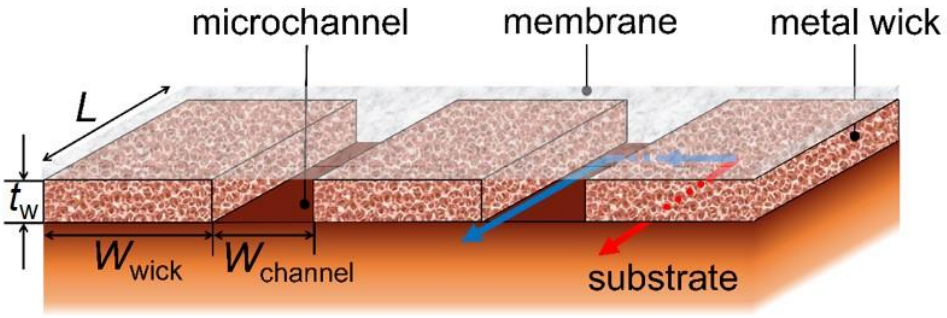

Figure 41: Schematic of capillary-driven condenser composed of a substrate, a porous metal wick layer with microchannels, and a top-layer hydrophobic membrane. The blue arrow shows the route through which the condensed water can exit from the microchannel. The red arrow shows the route through which the condensed water can exit directly from the metal wick. The key dimensions involved in this structure are the width of the wick layer W_{wick}, the width of the microchannel $W_{channel}$, and the thickness of the wick layer t_w.

Taking one microchannel and its neighboring metal wick block as a unit of interest. The viscous pressure loss that occurred inside the porous metal wick can be described by 1D Darcy's law:

$$u_{\mathrm{m,wick}} = \frac{\dot{V}(x)}{A_{\mathrm{c}}} = -\frac{\kappa \mathrm{d}P_{wick}}{\mu \mathrm{d}x} \tag{31}$$

where $u_{\mathrm{m,wick}}$ is the average flow velocity in the direction of flow, x is the direction of condensate flow, κ is the permeability of the metal wick, μ is the viscosity of the condensed water, $\dot{V}(x)$ is the volumetric flow rate of the condensate in the direction of x, A_{c} is the surface area of the cross-section of the metal wick layer perpendicular to the x direction. In the case of the condensed water traveling across the wick layer into the microchannel (as shown in the blue arrow), $A_{\mathrm{c}} = Lt_{\mathrm{w}}$; in the case of the condensed water exiting directly from the wick layer (as shown in the red arrow), $A_{\mathrm{c}} = W_{\mathrm{wick}}t_{\mathrm{w}}$.

For laminar flow (Re<2300), which is usually the case for the capillary-driven thin-film condensation, the viscous pressure drop that occurred inside a rectangular microchannel can be calculated by

$$\frac{\mathrm{d}P_{\mathrm{channel}}}{\mathrm{d}x} = -\frac{2f\rho_l {u_{\mathrm{m,channel}}}^2}{D_{\mathrm{H}}} \tag{32}$$

where D_{H} is the hydraulic diameter of the rectangular channel:

$$D_{\mathrm{H}} = \frac{4A_{\mathrm{c}}}{P_{\mathrm{w}}} = \frac{4(t_{\mathrm{w}} * W_{\mathrm{channel}})}{2(t_{\mathrm{w}} + W_{\mathrm{channel}})} \tag{33}$$

ρ_l is the density of the fluid, u_{m} is the mean flow velocity, and the Fanning friction factor f for a rectangular channel can be derived from the following equation:

$$fRe = 24(1 - 1.3553\alpha_{\mathrm{c}} + 1.9467{\alpha_{\mathrm{c}}}^2 - 1.7012{\alpha_{\mathrm{c}}}^3 + 0.9564{\alpha_{\mathrm{c}}}^4 - 0.2537{\alpha_{\mathrm{c}}}^5) \tag{34}$$

where $\alpha_{\mathrm{c}} = 1/\alpha = W_{\mathrm{channel}}/t_{\mathrm{w}}$ is the ratio of channel width to channel width.

Substituting equations (33) and (34) into (32), we can obtain

$$\frac{\mathrm{d}P_{\mathrm{channel}}}{\mathrm{d}x} = C f_n(t_{\mathrm{w}}, W_{\mathrm{channel}})\, u_{\mathrm{m,channel}} \tag{35}$$

where C is a constant related to fluid's physical properties, and $f_n(t_{\mathrm{w}}, W_{\mathrm{channel}})$ is a function of the channel geometry.

Due to the different permeability of the wick and the microchannel, a fluid with the same flow rate would experience a different pressure gradient inside the two regions. There exists a sweet spot where there is a certain amount of condensed water joining the microchannel from the wick layer such that the pressure drop across the wick material along the direction of the microchannel is the same as the pressure drop across the microchannel. At steady state, the pressure gradient along the direction of flow inside the channel and inside the wick materials achieve the same. Otherwise, there will be condensate flowing from the higher-pressure region to the lower-pressure region to balance the pressure difference, in which case the pressure gradient in the two regions will become the same at each x location eventually. Equaling $\frac{\mathrm{d}P_{\mathrm{channel}}}{\mathrm{d}x}$ to $\frac{\mathrm{d}P_{\mathrm{wick}}}{\mathrm{d}x}$ in equations (31) and (35), we can derive that

$$u_{\mathrm{m,channel}} = C_{12} u_{\mathrm{m,wick}} \tag{36}$$

where C_{12} is a function of channel geometry and wick's permeability:

$$C_{12} = \frac{{D_H}^2}{48(1 - 1.3553\alpha_c + 1.9467{\alpha_c}^2 - 1.7012{\alpha_c}^3 + 0.9564{\alpha_c}^4 - 0.2537{\alpha_c}^5)\kappa} \tag{37}$$

According to the mass conservation of condensed water, $\dot{V}(x)$ across a surface width of W can be expressed as a function of the condensation heat flux q as

$$\mathrm{d}\dot{V}(x) = \mathrm{d}(u_{\mathrm{m}}(x)t_{\mathrm{w}}W) = \frac{qW\mathrm{d}x}{\rho_l h_{\mathrm{fg}}} \tag{38}$$

where $u_{\mathrm{m}}(x)$ is the mean flow velocity at the cross-section of the microchannel-embedded wick at location x, and can be expressed as

$$u_{\mathrm{m}}(\mathrm{x}) = \frac{u_{\mathrm{m,wick}}(x)W_{\mathrm{wick}} + C_{12}u_{\mathrm{m,wick}}(x)W_{\mathrm{channel}}}{W_{\mathrm{channel}} + W_{\mathrm{wick}}} \tag{39}$$

Substituting equation (38) into (37), we can derive the expression of $u_{\mathrm{m,wick}}$

$$u_{\mathrm{m,wick}}(\mathrm{x}) = \frac{q(W_{\mathrm{wick}} + W_{\mathrm{channel}})}{\rho_l h_{\mathrm{fg}} t_{\mathrm{w}}(C_{12}W_{\mathrm{channel}} + W_{\mathrm{wick}})}x \tag{40}$$

Substituting equation (39) into (35), we can derive the expression of $\Delta P_{\mathrm{channel-wick}}(x)$ which is the viscous pressure drop that the condensed liquid would experience after flowing inside the microchannel-embedded wick over a distance of x:

$$\Delta P_{\mathrm{channel-wick}}(x) = -\frac{\mu q(W_{\mathrm{wick}} + W_{\mathrm{channel}})}{2\kappa\rho_l h_{\mathrm{fg}} t_{\mathrm{w}}(C_{12}W_{\mathrm{channel}} + W_{\mathrm{wick}})}x^2 \tag{41}$$

where the expression for C_{12} is shown by equation (37).

For a pure wick material with permeability κ and thickness t_{w} , we derive the expression of $\Delta P_{\mathrm{wick}}(x)$ as follows

$$\Delta P_{\mathrm{wick}}(x) = -\frac{\mu q}{2\kappa\rho_l h_{\mathrm{fg}} t_{\mathrm{w}}}x^2 \tag{42}$$

Comparing $\Delta P_{\mathrm{channel-wick}}(x)$ to $\Delta P_{\mathrm{wick}}(x)$, we can derive the following relationship:

$$\frac{\Delta P_{\mathrm{channel-wick}}(x)}{\Delta P_{\mathrm{wick}}(x)} = \frac{(W_{\mathrm{wick}} + W_{\mathrm{channel}})}{(C_{12}W_{\mathrm{channel}} + W_{\mathrm{wick}})} \tag{43}$$

where C_{12} is simply a function of the channel geometry as shown by equation (37).

Equation (43) shows that, assuming a uniform heat flux across the microchannel-embedded wick layer (which is a valid assumption in cases where the microchannels only occupy negligible surface area of the wick), the ratio of the pressure drop of fluid flow through

the microchannel-embedded wick layer to the pressure drop of fluid flow through a pure wick layer with the same wick permeability and thickness can be expressed by simply the geometry of the wick and the channel. With this understanding, we revisited the design of microchannels in the hierarchical copper sample.

We use the microchannel-embedded sample HierCu-1 as a case study. For simplicity, we fix the geometry of the microchannel height as the same as the wick thickness 180 μm. We assume the microchannels are evenly distributed on a surface of 2.54 cm by 2.54 cm (here for simplicity, we approximate the 1-inch circle surface to be a 1-inch by 1-inch square). The only two variables are the width of the channel and the number of microchannels to be engraved into the copper foam of HierCu-1.

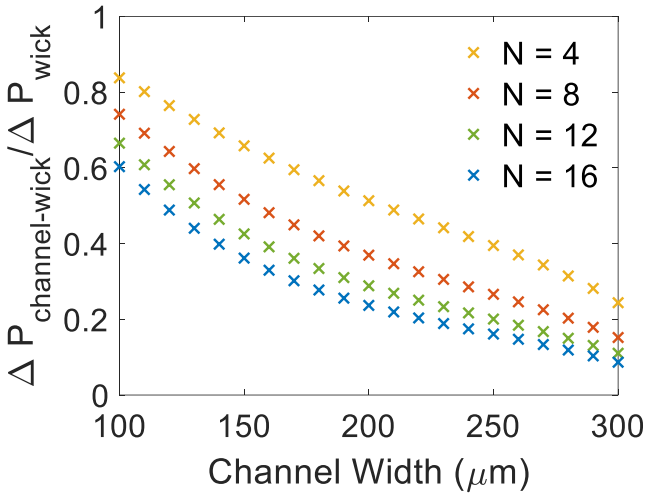

Figure 42: Pressure drop ratio $\frac{\Delta P_{channel-wick}}{\Delta P_{wick}}$ as a function of channel width and number of channels engraved into the copper foam wick of 180 μm thickness.

Figure 42 shows the ratio of the pressure drop of a fluid flowing through a microchannel-embedded wick layer to the pressure drop of a fluid flowing through the same wick layer without microchannels as a function of the channel width and the number of channels being machined. The properties of the copper foam in the HierCu-1 sample is used as a case study. A closer-to-zero pressure drop ratio indicates a great improvement in the wick permeability of the sample, while a closer-to-one pressure drop ratio indicates a small improvement in the wick permeability. Both increasing the channel width and increasing the number of channels can reduce the viscous pressure drop occurring in the wick layer. At the same area ratio of the channeled area over the un-channeled surface area, increasing the channel width is a more efficient strategy to decrease

the pressure drop ratio. For example, by increasing the number of 100 μm wide microchannels from 4 to 8, the pressure drop ratio only decreases from 84% to 74%. However, at the same channel area ratio, having 4 of the microchannels with doubled width could decrease the pressure drop ratio to 50%. Note that this model assumes a uniform condensation heat flux across the microchannel-embedded hierarchical copper surface. When the channel width or the number of channels becomes large, this assumption may not be valid anymore. With the developed model, a more permeable hierarchical copper sample can be designed for better anti-flooding properties by integrating the microchannel designs.

For the second strategy to prevent flooding, i.e., increasing the capillary pressure generated by the membrane pores, we come up with a completely different solution other than dealing with the fragile mesh pores and the unrobust hydrophobic coatings, which is to customize an intrinsically hydrophobic membrane with robust materials and tunable pore sizes. We will explore this topic in the next chapter.

3.5 Conclusions

In this chapter, we experimentally demonstrated the concept of capillary-driven thin-film condensation with commercially available copper meshes and foams. Using a biphilic, microchannel-embedded hierarchical copper sample, we measured an up to 2x condensation heat transfer as compared to the filmwise condensation even when the surface was flooded. Flooding was observed to occur before model predicted flooding thresholds, with the major causes being broken mesh pores and coating defects. Strategies to improve the thin-film condenser surfaces' robustness against flooding were discussed, including improving the wick-layer's permeability and improving the membrane layer's robustness. We developed a model to design microchannel as a strategy to improve wick permeability and prevent flooding. We will discuss the fabrication of a robust membrane layer in the next chapter.

4. Scalable Fabrication of Hydrophobic Membranes using Eletrospinning

In this chapter, we proposed to use electrospinning as a low-cost and scalable way to fabricate intrinsically hydrophobic and robust membrane layers for the capillary-driven thin-film condensers. During electrospinning process, many parameters could influence the morphology of the electrospun membranes. A parametric study was conducted to determine the most impactful parameter and thus the most efficient way to optimize the membrane morphology.

4.1 Motivation

In an effort to fabricate a scalable, robust, and cost-effective capillary-driven condenser, we fabricated intrinsically hydrophobic membranes based on electrospinning. Electrospinning is a sophisticated technique for fabricating nano- and microfiber membranes, which has been applied to various industries such as water desalination[111], oil-water separation[112], microfiltration[113], batteries[114], biomedical devices[115], and water harvesting[116]. We see the potential of using electrospinning to directly deposit fibers atop porous metal wick to fabricate capillary-driven condensers in a scalable way.

4.1.1 Electrospinning

Electrospinning, an easily tunable technique that utilizes the force balance between the electrostatic force and the solution surface tension to fabricate nanofibrous membrane, is promising for a wide range of applications. Compared to traditional phase inversion techniques for membrane fabrication, electrospinning enables the formation of interconnected pores with porosity exceeding 90%[117], which makes it a promising technique for fabricating the hydrophobic membrane layer in the capillary-driven thin-film condensers.

Morphology of the electrospun membrane is directly related to its performance. During an electrospinning process, many factors can affect the morphology of the products, such as properties of the solution, voltage supply, needle distance, feeding rate of the solution, and the electrospinning time. The wide range of tunable parameters allows a design space for optimizing the morphology of the electrospun membrane for any given application. In the capillary-driven thin-film condensers, membrane pore size is the most important morphological character to be optimized, followed by membrane thickness and membrane porosity. Effective parametric study

is needed to optimize the fabrication of electrospun membrane such that the ideal morphology of the electrospun membrane can be achieved by optimizing the most important parameters.

Many polymer materials exist for electrospinning hydrophobic membranes, such as polytetrafluoroethylene (PTFE), polypropylene (PP), and poly(vinylidenefluor-ide) (PVDF). In addition, Poly (vinylidene fluoride-co-hexafluoropropylene) (PVDF-HFP), a type of copolymer of PVDF, possess superior hydrophobicity, uniform pore distribution, and high porosity[78]. Therefore, we selected PVDF-HFP as our membrane materials for electrospinning.

4.1.2 Fractional Factorial Design (FFD)

Investigating the effects of each independent parameter (full factorial design) tends to be laborious and redundant. In statistics, fractional factorial design (FFD) is a powerful tool for reducing the experimental burden while recognizing the major effects[118].

FFD consists of a carefully chosen subset (fraction) of the experimental runs of a full factorial design, identifying the most important parameter to the response of interest. Figure 43 shows a schematic representation of a fractional factorial design[118]. When we know that the edges are orthogonal to each other in a cube, we only need 4 points instead of 8 points to determine the cube. Similarly, a full 8-run factorial design with three parameters can be reduced to a 4-run fractional factorial design. + or – in the figure indicates if the parameter is being maximized or minimized.

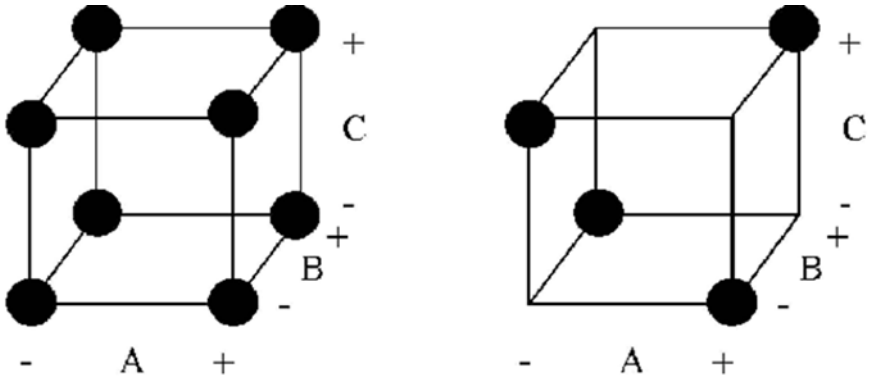

Figure 43: Schematic representation of a full 8-run factorial design with three parameters in comparison to a reduced 4-run fractional factorial design.

During an electrospinning process, many factors could affect the morphology of the products, such as viscosity of the solution, voltage supply, discharge distance, feed rate of the solution, and electrospinning time. In this work, we investigated the impacts of three of the most

important parameters on the morphology of electrospun fibrous membrane based on the fractional factorial design: voltage supply, discharge distance, and feeding rate of the solution.

4.2 Experimental Setup

We built a customized electrospinning set up, as shown in Figure 44. Two major components of the electrospinning setup are the high voltage power supply and the syringe pump. A polymer solution (PVDF-HFP in our current test) is loaded onto the syringe and extruded from the needle tip where a positive charge is applied. An aluminium foil covered copper plate is used as the fiber collector and is connected to a ground wire. The high voltage difference across the needle and the collector drives the polymer solution to spin onto the collector in a form of nano- or microfibers, under the counteractions of electrostatic force and surface tension experienced by the solution. The electrospinning process involves many operation parameters, some of which are critical to the fiber/membrane fabricated by the process. Some key parameters include voltage being applied, the distance between the needle and the collector, the concentration of the polymer solution, and the time the electrospinning process lasts. We focus on electrospinning PVDF-HFP since this polymer is intrinsically hydrophobic and is known to form uniform membrane pores.

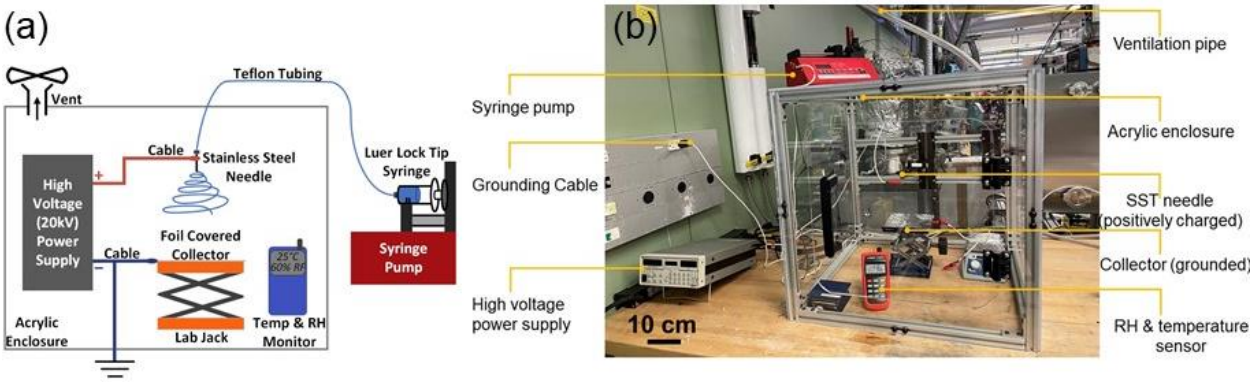

Figure 44: Schematic (a) and photo (b) of the custom-built electrospinning setup. The setup is composed of an acrylic enclosure with a vent line to the fume hood, a high voltage supply (20kV), a syringe pump that extends into the enclosure through a Teflon tube, a moving stage that is grounded, and a temperature and humidity sensor.

In the current study, we fixed the concentration of the electrospun fiber sample to be 15 wt% PVDF-HFP solutions in a 3:7 vol ratio of N,N-dimethylacetamide/acetone. This concentration was chosen based on trial and error to ensure that a continuous, bead-free fiber could be produced. The solution was prepared the night before the electrospinning and stirred on a hot plate of 80 °C for about12 hours before the electrospinning.

4.3 Sample Characterization

Three properties of the membrane are critical to vapor transport and heat transfer through the membrane layer: pore size, thickness, and porosity. For electrospun fibrous membranes, the pore size is usually proportional to the fiber diameter. In order to characterize these important properties, several techniques were used as detailed below.

Scanning electron microscopy (SEM) images were taken to help us characterize the morphology of the electrospun fibers, as shown in

Figure **45**. SEM images could clearly show important information of independent fibers (e.g., fiber diameter, presence of beads) and how the fibers are being aligned into a membrane. However, due to the random alignment of the electrospun fibers, it was hard to characterize pore size of the membrane using SEM.

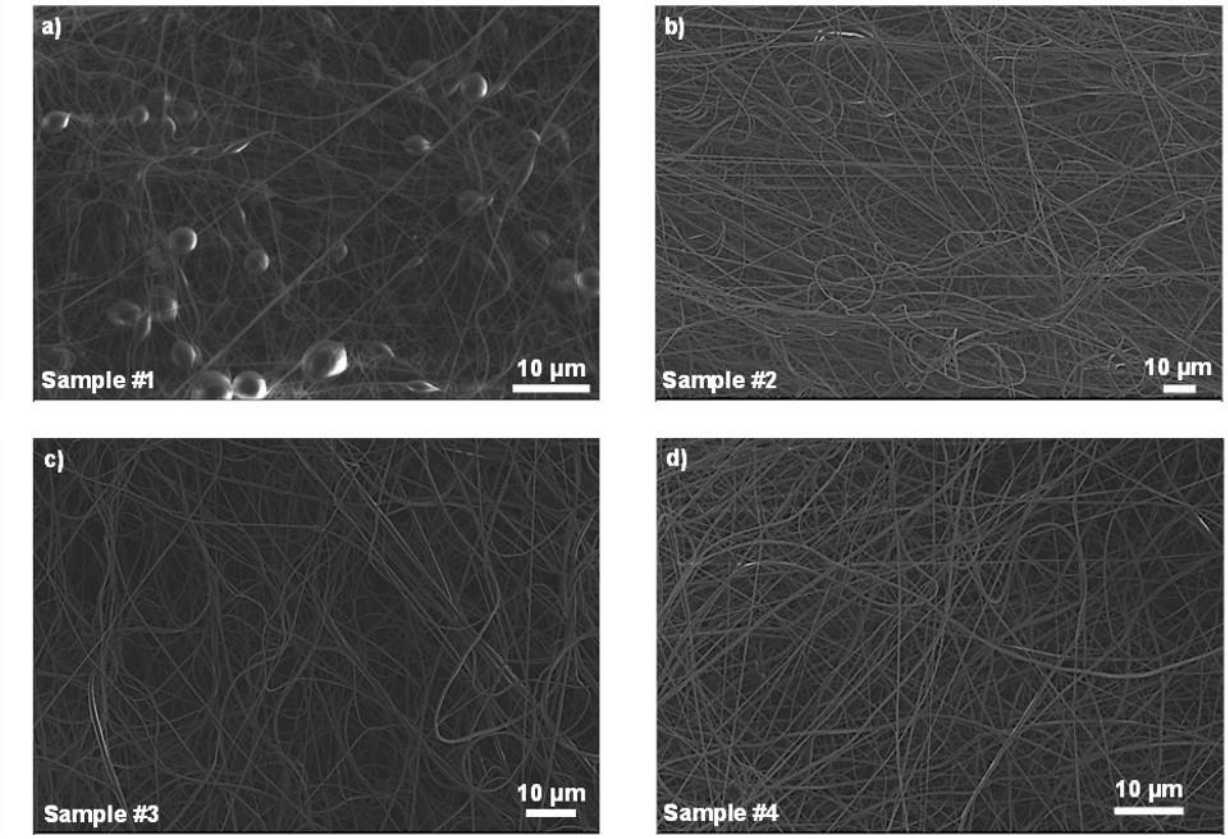

Figure 45: SEM images of electrospun membrane samples. Fiber diameter and morphology can be characterized accurately using SEM. However, pore size distribution is hard to define due to the random alignment of the fibers.

However, pore size distribution is an important information we need in order to predict the capillary pressure that the membrane can generate and the vapor transport resistance through the membrane. Therefore, in addition to the SEM, we used a capillary flow porometry (POROLUX™ 1000) to characterize pore size distribution of the electrospun membrane.

Figure 46 shows how a capillary flow porosity works to get the pore size distribution. We first wetted our sample membrane with a known fluid (Galpore, surface tension 15.6 mN/m) and put it into the porometer for the wet curve measurement. During the measurement, a nitrogen flow was applied to the membrane sample with incremental pressure difference across the membrane. At each pressure, flow rate of nitrogen gas was recorded. At the beginning of the measurement, flow rate stayed at zero since all the pores were blocked by the liquid. At one point, nitrogen started to flow through the membrane, which denoted that the biggest pore inside the membrane (i.e., bobble point pore size) was opened up by the gas flow. After this point, the nitrogen gas flow rate would keep increasing until a point when the smallest pore inside the membrane was open, i.e., the membrane became completely dry. Following the wet curve measurement, another round of gas flow rate measurement was repeated on the dry sample with the same incremental pressure being applied, resulted in a dry curve. A curve with 50% of the dry curve slope was plotted as “half-dry curve”, as shown in Figure 46. Pore size at which 50 % of the total gas flow can be accounted (half the flow is through pores larger than this diameter) is defined as the mean flow pore (MFP) diameter. Pore size distribution could be extracted from the wet curve and dry curve measurements, as shown in Figure 47. Electrospun PVDF-HFP has been known for its uniform pore size. The pore size distribution measured by the porometer validated the uniform pore sizes of our electrospun PVDF-HFP membranes.

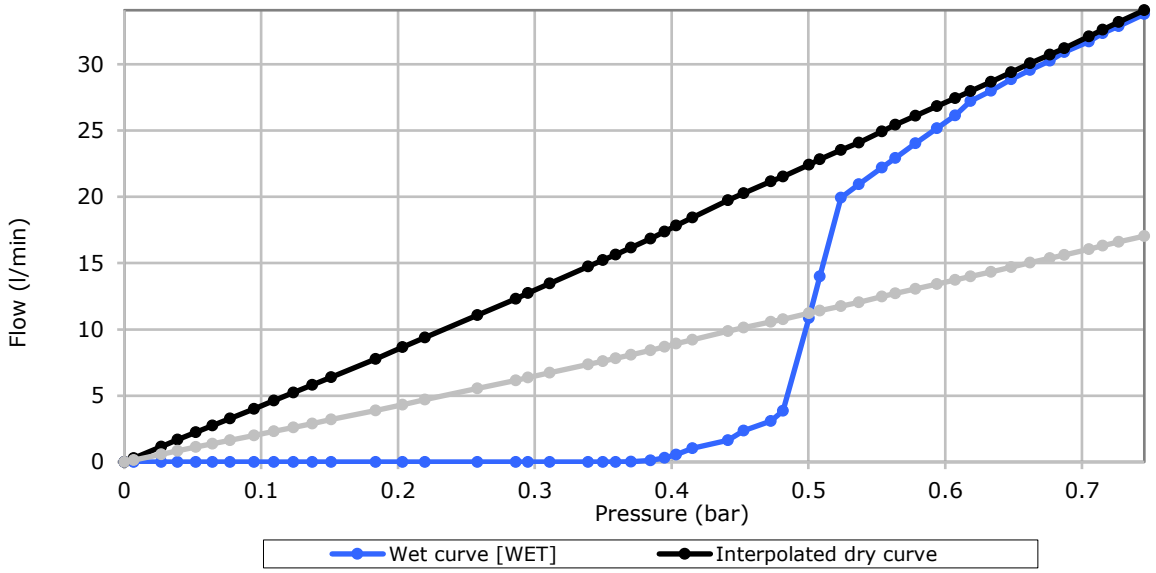

Figure 46: Wet curve and dry curve of an electrospun membrane sample given by the capillary flow porometer (POROLUX™ 1000).

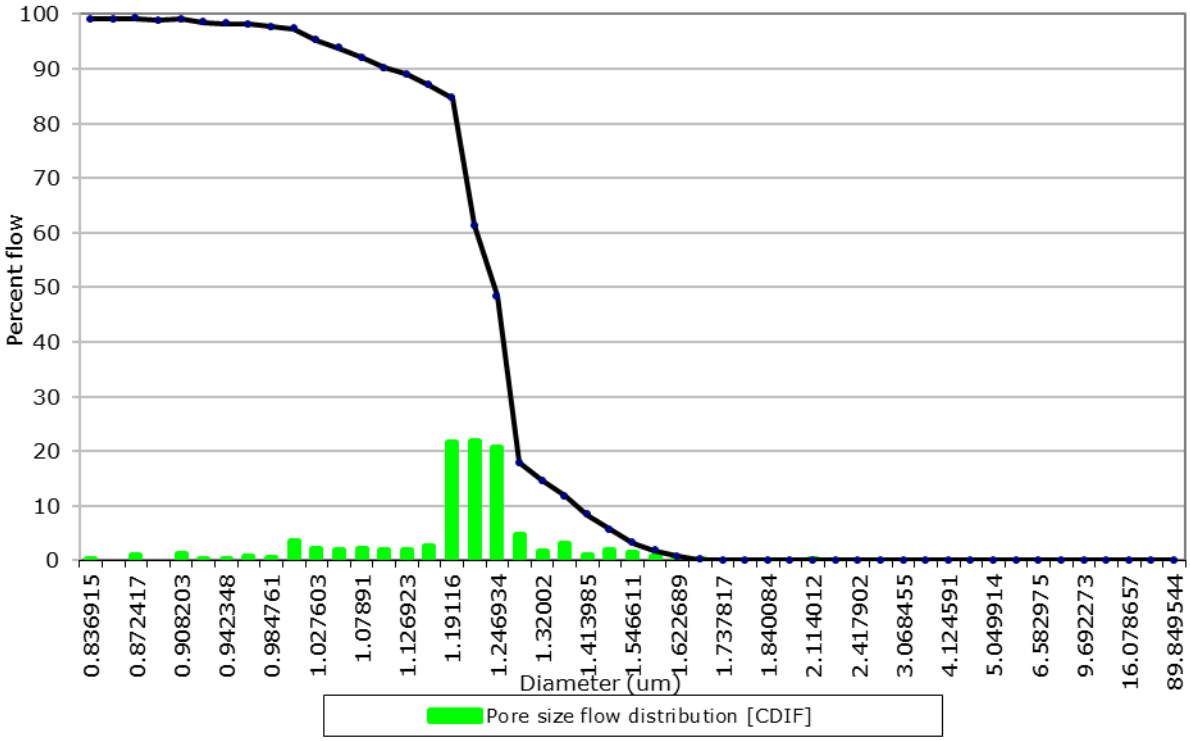

Figure 47: Pore size distribution of an electrospun membrane sample given by the capillary flow porometer (POROLUX™ 1000).

Typically, the fiber diameter of an eletrospun fibrous membrane is positively related to the pore size of the membrane, although the arrangement of the fibers and the shape of the fibers

(i.e., bead-free or not) can also impact the pore size. Here, two electrospun fibrous membranes of different morphologies were made with different fabrication parameters. We characterized the fiber size distribution on these two samples by analyzing their fiber diameters in SEM images using Image J. Pore size distribution on the same samples was characterized using a capillary flow porometer. The characterization results are shown in Figure 48. (a)-(c) shows the SEM image, the fiber size distribution, and the pore size distribution of the first electrospun membrane. (d)-(f) shows the SEM image, the fiber size distribution, and the pore size distribution of the second electrospun membrane. As shown in the SEM images, it is visually distinguishable that the first electrospun membrane has a smaller fiber diameter than the second one. This is confirmed by the fiber diameter distribution shown in (b) and (e). Pore size distribution was found to follow the same trend as the fiber diameter distribution.

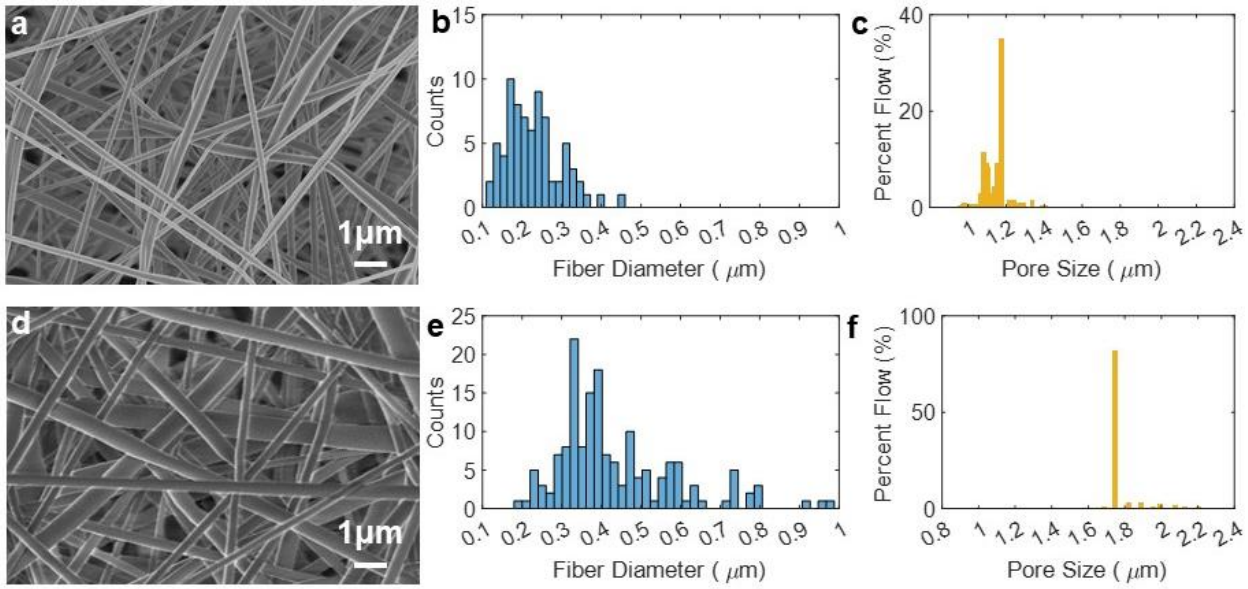

Figure 48: SEM images of two electrospun PVDF-HFP samples (top, bottom) and their corresponding fiber diameter distribution and pore size distribution. Fiber diameter is positively correlated to membrane pore size.

We chose to use fiber diameter as an indicator for pore size of the membrane for the parametric study. This is mainly because the porometer was not as accessible as the SEM during the course of this study. In addition, it is slightly more time-consuming to characterize the pore size using a porometer, and we had many samples to characterize. After the completion of a parametric study based on fiber diameter measurements, we ran a quick round of pore size

characterization and confirmed that the conclusion we obtained with the pore size information was the same as what we got from the parametric study based on fiber diameter measurements.

4.4 Parametric Study Guided by Fractional Factorial Design (FFD)

The thickness of the electrospun membrane was easily tunable by increasing or decreasing the electrospinning time. Membrane porosity of the electrospun PVDF-HFP is known to be high and has been measured to be within the range of 80% to 90% for all the samples we made. Therefore, for the parametric study, we focus on studying the impact on the membrane pore size (represented by fiber size) from three important fabrication parameters: needle-collecter distance, voltage supply, and the solution feeding rate.

We experimentally determined the variation boundaries for the three parameters mentioned above to ensure that a bead-free fiber could be continuously generated at the given conditions. Key parameters studied and their variation range are listed in Table 6.

Table 6: Key parameters studied and their variation range.

Parameter	Lower Bound (-)	Upper Bound (+)
Needle Distance (cm)	15	20
Voltage Supply (kV)	10	20
Feeding Rate (mL/hr)	0.1	1

By using the JMP software, we conducted a design of experiment via fractional factorial design (FFD). Table 7 shows the Subset of the experimental runs guided by the fractional factorial design. The fractional factorial design simplified a full 8-run parametric study into 4 runs. Each set of parameters was run for at least 2 times under similar environmental conditions and the morphology of the resulted membranes was characterized with SEM.

Table 7: Subset of the experimental runs guided by the fractional factorial design.

Patten	Needle Distance (cm)	Voltage Supply (kV)	Feeding Rate (mL/hr)	Solution Concentration (wt%)	Electrospinning Time (min)
+−−	20	15	0.1	15	60

−−+	10	15	1	15	60
+++	20	20	1	15	60
−+−	10	20	0.1	15	60

Figure 49 shows the fiber diameter as a function of needle distance, voltage supply, and solution feeding rate predicted with experimental data obtained by the FFD. Least squares method was used to find the best fit. Confidence intervals are shown in grey. Solution feeding rate has the most significant impact on the fiber diameter of the electrospun PVDF-HFP membrane. Fiber diameter increases with decreasing solution feeding rate. We expect the membrane pore size to also increase with decreasing solution feeding rate.

In comparison, needle distance and voltage supply only have minimal impact on the fiber diameter throughout the variation range we explored. Therefore, to optimize the membrane morphology (i.e., fiber diameter), more focus should be put on tuning the feeding rate over the other two parameters.

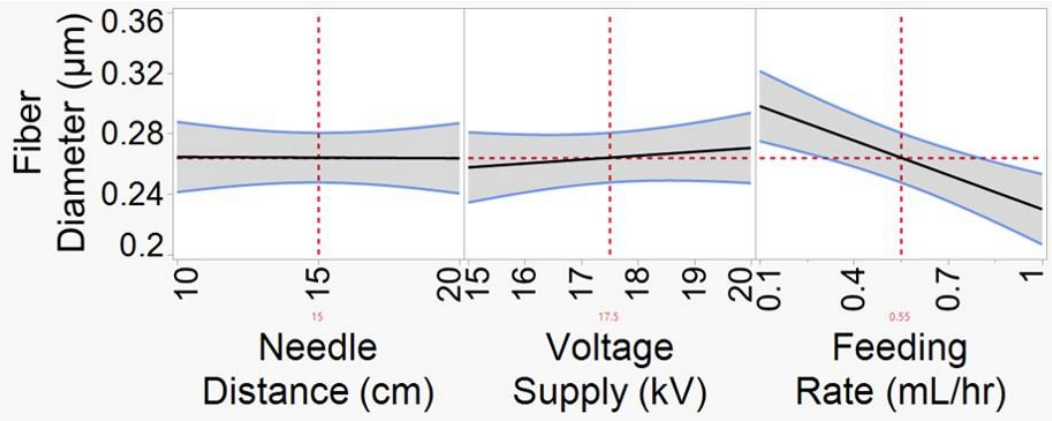

Figure 49: Fiber diameter as a function of needle distance, voltage supply, and solution feeding rate predicted with experimental data obtained by the FFD. Least squares method was used to find the best fit. Confidence intervals are shown in grey.

In order to validate that the same conclusions obtained from the fiber diameter characterization are applicable to the pore size of the membranes, we characterized the pore size of a set of electrospun membranes fabricated with the parameters shown in Table 7. Using membrane mean flow pore (MFP) size as the result for the parametric study, we plotted

membrane MFP size as a function of needle distance, voltage supply, and solution feeding rate predicted with experimental data obtained. The results about feeding rate shown in Figure 50 are in great agreement with the result in Figure 49, validating the importance of solution feeding rate in tuning the membrane morphology.

Note that the impact of voltage supply and needle distance on the membrane pore size as shown in Figure 50 were found to be more significant than their impact on fiber diameter as shown in Figure 49. This difference can be explained by two factors. First, membrane pore size and membrane fiber diameter are not always positively corelated, as membrane pore size is not only affected by the fiber diameter but also affected by how the fibers are aligned with each other. Therefore, the impact of one fabrication parameter on fiber diameter could be different from its impact on membrane pore size. Second, FFD considers a subset of the experimental run to be representative for the full factorial run. When analyzing pore size, for simplicity, we only fabricated one electrospun membrane for each set of parameters provided by FFD, which might introduce statistical errors and might not be representative enough. Fabricating a few more membranes for each set of parameters and averaging the measurements would reduce the statistical errors.

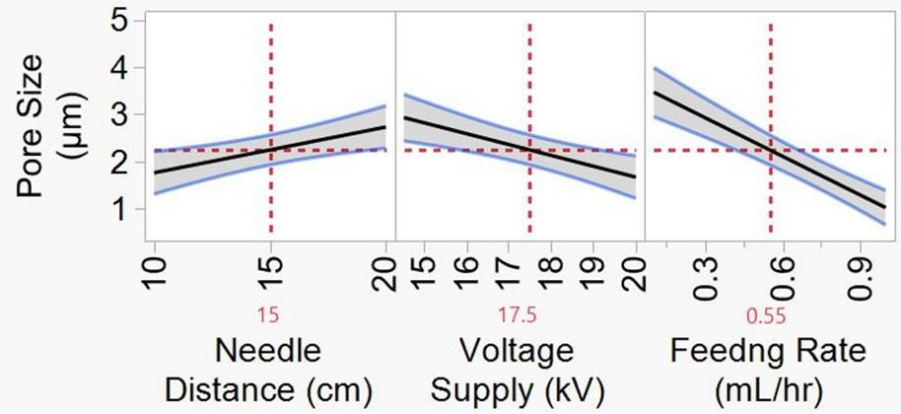

Figure 50: Membrane mean flow pore size as a function of needle distance, voltage supply, and solution feeding rate predicted with experimental data.

Furthermore, we experimentally verified that membrane thickness can be adjusted easily by increasing or decreasing the electrospinning time without making much difference in the membrane morphology. Four sets of different fabrication parameters were tested as shown in A, B, C, and D. Fiber diameters after 20 minutes and 60 minutes of electrospinning were compared. The effect of electrospinning time on the fiber diameter is negligible, as shown in **Error!**

Reference source not found.. As a result, when optimizing membrane properties for the capillary-driven thin-film condenser, we can focus on optimizing the membrane pore size first,

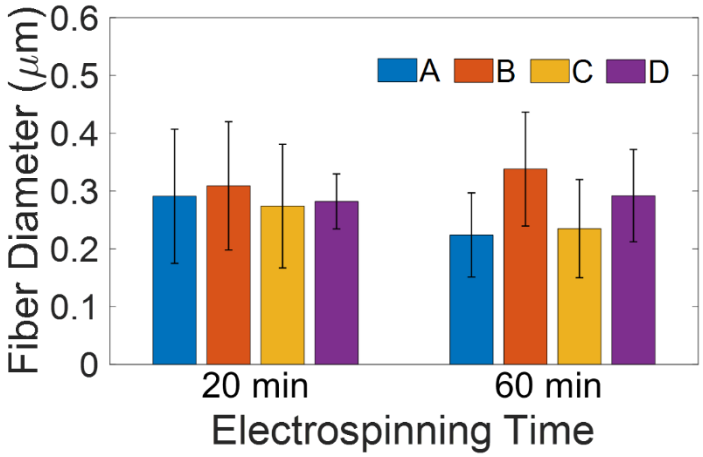

Figure 51: Effects of electrospinning time on the fiber diameter of the electrospun PVDF-HFP membrane.

knowing that membrane thickness can be easily adjusted by changing the electrospinning time.

Lastly, we report the effects of aging of the PVDF-HFP solution on the fiber morphology of the electrospun membrane. The solution was kept stirring on an 80℃ hot plate. Two sets of parameters were tested on Day 1, 2, and 3 after the solution was prepared. Fiber diameter consistently decreases with time, indicating the aging of the solution, as shown in Figure 52. The mechanism of the aging is to be further explored. For the current study, we always prepare a fresh solution before the electrospinning experiment to prevent solution aging.

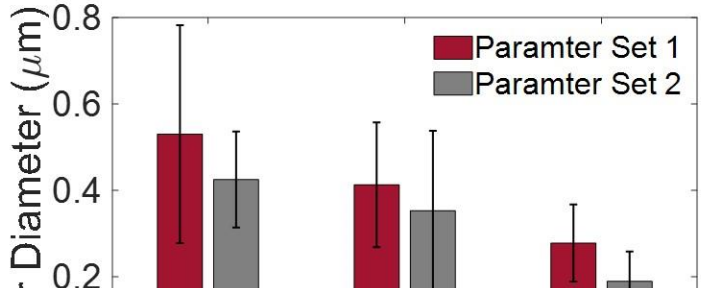

Figure 52: Effects of the aging of the PVDF-HFP solution on the fiber diameter of the electrospun membrane. The solution was kept stirring on an 80℃ hot plate. Two sets of parameters were tested on Day 1, 2, and 3 after the solution was prepared. Fiber diameter consistently decreases with time, indicating the aging of the solution.

4.5 Combining Electospun Membrane with Porous Metal Wick

Combining electrospun membrane with porous metal wick is a scalable way to fabricate capillary-driven thin-film condensers. Here, we preliminarily tried combining these two components together experimentally, and developed a model that predicts the heat transfer performance of the electrospun fiber covered porous copper at large scale.

4.5.1 Preliminary Fabrication and Visualization Study

We preliminary fabricated an electrospun PVDF-HFP membrane directly on a porous copper foam, as shown in Figure 53. A circle piece of copper foam with a diameter of 1 inch was directly used as the collector of the fiber, as shown in Figure 53(a). The porous copper foam was sitting on a ceramic plate with a 1-inch diameter circle dent in the middle. A thin aluminum foil with 1-inch diameter was put in between the porous copper and the ceramic for conducting electricity. The aluminum foil has two aluminum legs that were protected by electrical tapes. Only the tips of the foil legs were exposed and connected to the ground.

Figure 53(b) shows the SEM image of the resultant fiber covered porous copper. The copper foam has a characteristic pore size that is on the order of 100 μm. Interestingly, the membrane fibers were accumulated on top of the copper islands during the beginning of the electrospinning, leaving big voids in between the solid islands. This is because at the beginning of electrospinning, the voltage potential between the needle and the collector was strongest at the top of the metal islands; as a result, fibers were attracted to be deposited onto the metal islands. As electrospinning continues, these voids can be covered by fibers that are deposited later. However, it is important to guarantee a uniformly thin membrane, as the model predicts that heat and mass transfer performance would degrade with increasing membrane thickness.

We characterized pure vapor condensation on an electrospun fiber-covered porous copper foam using ESEM (Zeiss EVO 50 scanning electron microscope), as shown by the time-lapse images shown in Figure 54. As expected, water vapor travelled through the PVDF-HFP fibers, nucleating and growing on the hydrophilic copper surfaces, with no condensate found on top of the membrane. Due to the large voids in between copper islands, we were not able to show thin film condensation confined by the membrane. However, if we can evenly spin the hydrophobic fiber on top of the porous metal wick, we expect thin-film condensation to occur.

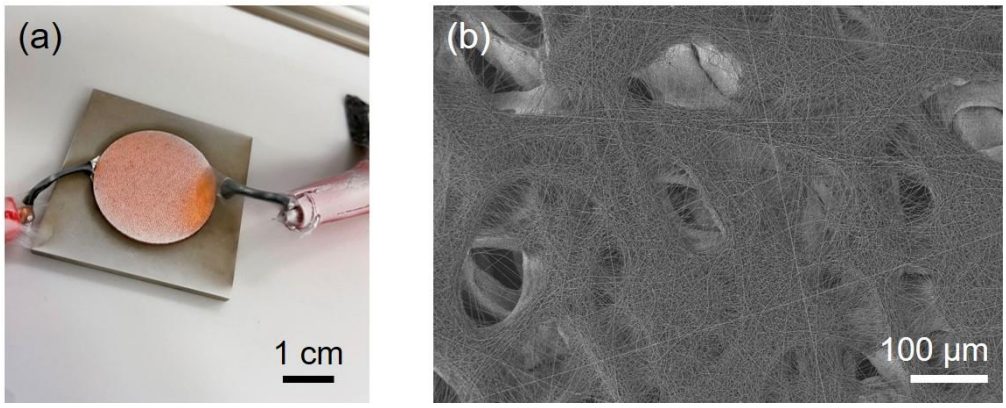

Figure 53: Preliminary fabrication of electrospun PVDF-HFP membrane on top of a porous copper foam substrate. (a) A circle piece of copper foam with diameter of 1 inch was directly used as the collector of the fiber. The porous copper foam was sitting on top of a thin aluminum foil that was kept on a ceramic plate with a 1-inch diameter circle dent in the middle. The dent on the ceramic place was used to support the aluminum foil. The aluminum foil has two aluminum legs that were protected by electrical tapes. Only the tips of the foil legs were exposed and connected to the ground. (b) SEM of the resulted sample shows that the membrane fibers were accumulated on top of the copper islands during the beginning of the electrospinning, leaving big voids in between the solid islands.

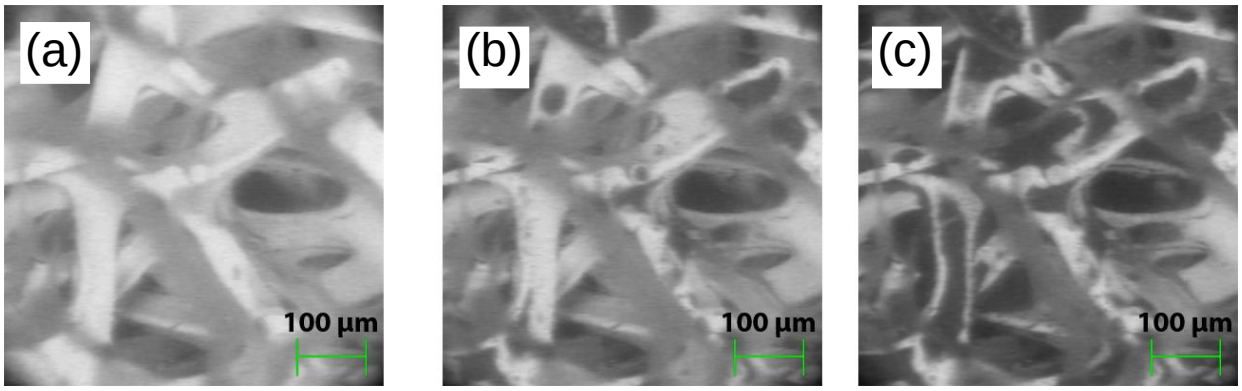

Figure 54: Time lapse ESEM images showing the electrospun fiber covered copper foam before condensation (a), during condensation nucleation on the copper (b), and during continuous growing of the liquid film on the copper (c).

4.5.2 Modeling Prediction for Thin-Film Condensation with Electrospun Fiber Covered Porous Copper

We used the heat and mass transfer model described in Chapter 2 for predicting the heat transfer performance of the electrospun-fiber covered porous copper based on vapor transport through the membrane pores and heat conduction through the condensate-filled porous copper. To simplify, a parallel model was used to calculate the effective thermal conductivities of the

porous copper wicks. This may overestimate the heat transfer performance of the wick layer, depending on how close the thermal resistance in the copper wick is to a parallel mode. Figure 55 shows the model prediction for condensation heat transfer performance of different capillary-driven condensers made of electrospun membrane covered porous copper. Three different porous copper are used as the wick layer in the model:

(a) Copper foam with 200 μm thickness, 65% porosity, and 1×10^{-11} m^2 permeability.

(b) Inverse opal copper with 5 μm thickness, 65% porosity, and 5×10^{-11} m^2 permeability.

(c) Sintered copper spheres with 200 μm thickness, 50% porosity, and $1.7\times10^{-11}m^2$ permeability.

Sample (a) is what we have in lab and is commercially available. Sample (b) is a structure that we are fabricating in lab. Sample (c) is a common structure in heat pipe industries and we are considering fabricating. All three plots shown in Figure 55 were obtained at a given vapor temperature (T_v = 35°C) and subcooling of 5°C. X-axis is pore size of the electrospun membrane and y-axis is the corresponding heat flux predicted by the model. Red, blue, and green lines correspond to three different membrane porosity: 0.9, 0.8, and 0.7. Different thickness of lines means different membrane thickness. The black dash line denotes filmwise condensation predicted by the Nusselt model. In our model, heat flux would drop to zero when "flooding" occurs; this is not true in reality but is used as an indicator for "flooding" in the modelling results.

Figure 55 (a) and (c) are similar: with higher membrane pore size (increasing x-axis), higher porosity (red line), and smaller membrane thickness (10 μm thick denoted by the thinnest line), heat transfer gets much enhancement and no flooding occurs throughout the sweep. The similarity between these two plots is because we prescribe similar properties for the copper foam (corresponding to the Figure 55 (a)) and the sintered copper (corresponding to Figure 55 (c)).

The lines in Figure 55 (b) (corresponding to inverse opal copper) are not smooth due to the incremental sweep other than a continuous sweep we performed. Heat flux given by the same membrane increases faster in Figure 55 (b) as compared to the other two plots, but also induces flooding easier, which is because the ultra-thin inverse opal (5 μm thick) could greatly reduce the thermal resistance of the water-filled porous copper but on the other hand, these thin structures

are easier to flood (condenser liquid cannot be completely drained from the edge of the thin wick).

Overall, the model guided us to fabricate a membrane that is thin (on the order of 10 μm), highly porous (90%), and has large pore size (on the order of 1 μm). This geometry is achievable by electrospinning. A full parametric study is needed for the optimization of the membrane structures with a focus on the solution feeding rate as the key parameter to manipulate. As a conservative estimation, we expect to see over 5x enhancement on the electrospun membrane covered sintered copper powder without flooding under subcooling of 5 °C, as predicted by the model.

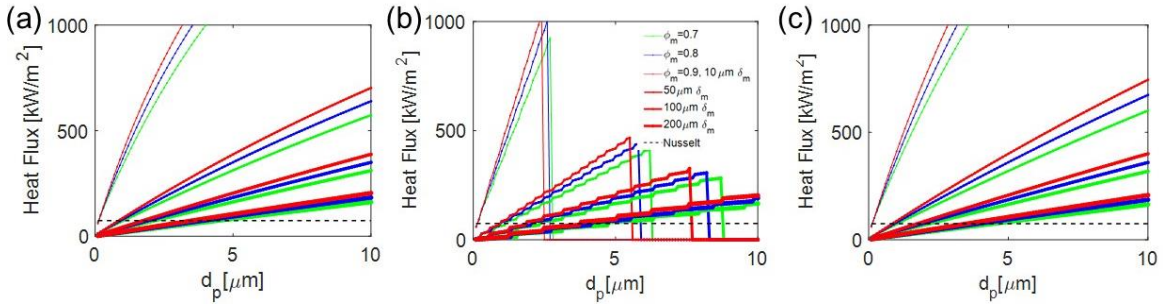

Figure 55: Condensation heat transfer performance of different types of porous copper covered by electrospun fibers, as predicted by heat and mass transfer model. (a) Electrospun fibers in combination with a copper foam with 200 μm thickness, 65% porosity, and 1×10^{-11} m^2 permeability. (b) Electrospun fibers in combination with inverse opal copper with 5 μm thickness, 65% porosity, and 5×10^{-11} m^2 permeability. (c) Electrospun fibers in combination with sintered copper spheres with 50 μm sphere diameter, 200 μm thickness, 50% porosity, and 1.7×10^{-11}m^2 permeability.

4.6 Conclusion

A parametric study on the effect of three key fabrication parameters (needle distance, voltage supply, and solution feeding rate) on the morphology of the electrospun PVDF-HFP membrane were conducted using FFD.

Solution feeding rate was found to be the most impactful parameter among all three parameters on the fiber diameter and the pore size of the membrane. A higher feeding rate would produce a smaller fiber diameter and a smaller membrane pore size.

The duration of electrospinning was found to be irrelevant to the membrane morphology, providing an opportunity to optimize membrane thickness without worrying about changes in membrane pore sizes.

Preliminary fabrication of electrospun membrane covered porous coppers shows promises to realize thin-film condensation if a uniformly thin membrane could be obtained. Bonding of the eletcrospun membrane to the porous metal wick is a major challenge that needs to be solved.

We conducted a multiparametric analysis on the heat transfer performance of electrospun membrane-covered porous metals. A conservative estimation of 5x HTC enhancement is predicted for electrospun fiber covered porous copper powders.

5. Techno-economic Evaluation for Thin-film Condensers

5.1 Market Segment

The economics and operating conditions vary widely by the type of power plants, Therefore, we segmented the market into the following three types: nuclear, geothermal, and fossil plants. According to the 2020 Annual Technology Baseline (ATB) Cost and Performance Data for Electricity Generation Technologies released by the National Renewable Energy Laboratory of the U.S. Department of Energy[119], the overnight capital cost for different types of power plants vary a lot, with the highest value for geothermal power plants being $6,397,000/MW and the lowest value for the natural gas steam power plants being $903,000/MW. Detailed information about the overnight capital cost and the total capacity in the US and internationally of each type of power plant can be found in Table 8.

Table 8: Market segmentation of steam power plants.

Plant Type	Value $/Incremental MW	US Capacity (MW)	International Capacity (MW)	Global Capacity (MW)
Nuclear	6,031,000	100,899	303,679	404,578
Natural Gas Steam	903,000	81,515	139,961.9568	221,477
Natural Gas Combined Cycle	1,044,000	310,758	533,577	844335
Conventional Coal	4,150,000	233,129	1,716,392	1,949,521
Geothermal	6,397,000	3,865	8,799	12,664

5.2 Value Proposition for Different Market Segments

Before we discuss the value proposition, we should first consider the cost of manufacturing a thin-film condenser at scale. Based on existing cost data for a steam condenser in a 950 MW nuclear power plant[120], we estimated material costs to modify an existing condenser with PVDF polymer membrane and a porous copper powder wick of 70% porosity and 0.1mm thickness. The 950 MW condenser has 23,150 tubes made of 90/10 cupronickel alloy with dimensions D_o=28.6 mm and L=13.4 m. These plain tubes cost 4.63 Million USD.

The raw materials needed to modify plain copper tubes are copper powder ($135/kg) and polymer PVDF materials ($1.5/m^2). We calculated material costs based on the dimensions of condenser tubes in the 950 MW nuclear power plant, with the only modification being the tube surface. Assuming the fabrication cost to be 1/3 of the material cost, we estimated $1.5k/MW in total modification costs for a condenser. This in addition to the cost of plain condenser tubes ($4.9k/MW) and shipping (10% of product cost) totals $7k/MW in manufacturing and shipping costs for the condenser tubes. Conventional shell and tube condensers cost around $22k/MW to manufacture and ship. With the incremental $2.1k/MW in cost from the thin-film condenser tubes, we are effectively adding 10% to the manufacturing cost of a shell and tube condenser.

According to conversations with power plant engineers, power plants almost never operate at nameplate capacity – a more efficient condenser could help get closer to the nameplate capacity. To quantify the value proposition for different market segments, we developed a thermodynamic model to predict the overall capacity improvement that a thin-film condenser can provide with each type of power plant. A conservative assumption of 5x steam side heat transfer enhancement as compared to filmwise condensation is applied. Assuming using the same condenser inlet water temperature and flow rate, an enhanced condenser results in a much lower condenser saturation temperature, which enables the working fluid (water) to absorb more heat from the given heat source and to generate more power output at the turbine. As shown in Table 9, Table 10, and Table 11, by replacing a plain condenser with a PVDF-porous copper coated thin-film condenser, the output capacity of the nuclear power plant, the geothermal power plant, and the coal power plant are roughly 4%, 6%, and 2% respectively. Note that even 1% of capacity improvement is regarded as huge in the power plant industry and that we assumed only 5x steam side heat transfer, which is a conservative assumption for what a thin-film condenser can achieve.

Table 9: Thermodynamic Evaluation for a 950 MW Nuclear Power Plant.

Item	**Plain Condenser**	**Thin-film Condenser**	**Unit**
Boiler heat input Q_h	3,125	3,156	MW
Condenser water T_{in}	20	20	^oC

Condenser water T_{out}	35.58	35.55	^{o}C
Condenser saturation temperature	46.11	39.74	^{o}C
Condenser external HTC	8.778	43.891	kW/m^{2}K
Condenser overall HTC	4.548	7.767	kW/m^{2}K
Condenser heat rejection/MW	2,175	2,172	MW
Condenser water volume flow rate	33.394	33.394	m^3/s
Turbine output W_t	950	984	MW
Increased power output	-	34.36	MW
Capacity improvement	-	**3.62%**	-

Table 10: Thermodynamic Evaluation for a 100 MW Geothermal Power Plant.

Item	**Plain Condenser**	**Thin-film Condenser**	**Unit**
Geothermal heat input Q_h	512.8	517.5	MW
Condenser water T_{in}	20	20	^{o}C
Condenser water T_{out}	31.00	30.97	^{o}C
Condenser saturation temperature	40.04	34.40	^{o}C
Condenser external HTC	8.951	44.754	kW/m^{2}K
Condenser overall HTC	4.966	8.928	kW/m^{2}K
Condenser heat rejection/MW	412.79	411.41	MW
Condenser water volume flow rate	8.97	8.97	m^3/s
Turbine output W_t	950	984	MW

Increased power output	-	6.08	MW
Capacity improvement	-	**6.08%**	-

Table 11: Thermodynamic Evaluation for a 950 MW Coal Power Plant.

Item	**Plain Condenser**	**Thin-film Condenser**	**Unit**
Boiler heat input Q_h	2657.5	2674.5	MW
Condenser water T_{in}	20	20	^oC
Condenser water T_{out}	36.89	36.86	^oC
Condenser saturation temperature	46.12	41.26	^oC
Condenser external HTC	8.899	44.495	kW/m^2K
Condenser overall HTC	3.776	5.715	kW/m^2K
Condenser heat rejection/MW	1707.5	1707.4	MW
Condenser water volume flow rate	24.18	24.18	m^3/s
Turbine output W_t	950	970.03	MW
Increased power output	-	20.03	MW
Capacity improvement	-	**2.11%**	-

5.3 Total Addressable Market

To quantify the capacity improvement we have shown in Table 9, Table 10, and Table 11 in terms of economic value, we estimated the total addressable market across the globe. Assuming a condenser lifetime of 15 years with a 5% plant weighted average cost of capital (WACC) and a 20% targeted plant internal rate of return (IRR), we obtained an adjustment factor of 0.45. Applying this adjustment factor and assuming a 10% annual turnover rate, we estimated

the market value of thin-film condensers for each market segment, and added them to into a total addressable market worth ~$13 B. Detailed calculation is shown in Table 12.

Table 12: Total addressable market estimation for thin-film condensers.

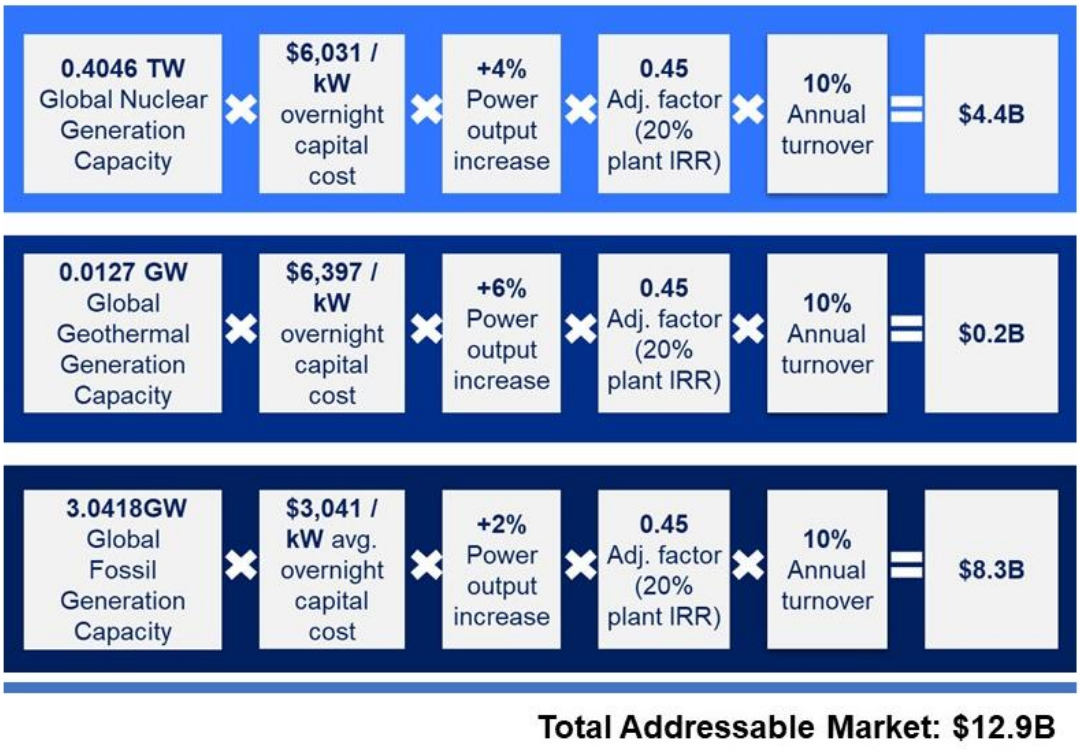

5.4 Discussion

By incorporating thin-film condensers into the steam power plants, we can improve power plants' capacity by 2-6% based on the conservative assumption that thin-film condensers are capable of enhancing steam side condensation heat transfer by 5x as compared to a conventional filmwise condensation. At this capacity improvement, thin-film condensers provide $13B annual value to the global market.

The condenser's heat transfer improvement makes a more significant impact in power plants that are operating at relatively low efficiencies, such as geothermal power plants.

A rough estimation on the fabrication and material cost for condenser tube modification results in a less than 10% cost increase in manufacturing a condenser. However, scaling up a

thin-film condensing surface still needs further development. The key concerns remaining to be addressed are:

- Scaling up highly permeable and thermally conductive porous metal wicks ideally with a thickness on the order of tens of microns.
- Bonding the hydrophobic membrane onto the porous metal substrate remains challenging. Having a robust bonding between the membrane and the wick in the thin-film condenser is crucial for the reliability of the condenser.
- The longevity of the condenser surface coatings is critical for its application in power plants. Ideally, the lifetime of the thin-film condenser needs to at least match the plant's major maintenance cycle, which occurs every 2-5 years depending on the type of the power plant.
- Although we assumed a perfectly clean condenser surface in the thermodynamic model, this is usually not the case in the real world. Scaling, fouling, and corrosion can be even more important problems than the steam side heat transfer in certain cases.

6. Summary and Perspectives

Enhancing condensation heat transfer of water vapor can significantly improve the energy efficiency of a steam power plant, producing more electricity while reducing the carbon footprint and freshwater withdrawal. Research in hydrophobic coatings has shown up to an order of magnitude better condensation heat transfer of water on hydrophobic surfaces as compared to condensation heat transfer of water on bare metal surfaces. However, the durability or scalability of these hydrophobic coatings remains challenging, which prevents them from being applied in industry. In the current thesis, we proposed a new concept which we termed thin-film condensation. This mode of condensation is achieved by stacking a thermally conductive, porous metal wick in between a hydrophobic membrane and the condenser substrate. The capillary pressure generated by the hydrophobic membrane keeps the condensed water inside the porous metal wick, achieving a thin, thermally-conductive condensate film, which can greatly enhance the condensation heat transfer of water vapor. By choosing scalable approach and robust materials, thin-film condensation shows great promise for application in enhancing condensation heat transfer in steam power plants.

In Chapter 2, we developed a heat and mass transfer model which guides the design of the two-layer structures of the thin-film condenser. For simplicity, we assumed that the parameters we investigated were independent with each other, and the parametric study shows that membrane pore size and wick permeability are the most impactful parameters for enhancing the heat transfer performance of the thin-film condenser while preventing surface flooding. Followed by the model guideline, in Chapter 3, we fabricated biphilic, hierarchical copper samples for the proof of concept of thin-film condensation using commercially available materials. Although the model predicts an over 7x heat transfer, an up to 2x condensation heat transfer enhancement was experimentally measured on the hierarchical copper sample due to surface flooding. Strategies for preventing surface flooding from occurring were discussed, including microchannel designs and the use of robust membrane materials. In Chapter 4, we proposed to use electrospinning as a scalable approach to make robust membranes for the thin-film condensers. Fractional factorial design was used to simplify the parametric study and solution feeding rate was found to be the most impactful parameters on the pore size and fiber size of the electrospun PVDF-HFP membrane. Preliminary test of combining electrospun membrane with porous copper wick shows that electrospun fibers would preferably deposit onto

the solid regions of the porous metal wick, posing a challenge to obtain a uniformly thin hydrophobic membrane. Assuming a uniformly thin membrane can be obtained, a thin-film condenser made of electrospun membranes and porous metal wicks can achieve over 5x condensation heat transfer enhancement as predicted by the model. In Chapter 5, we conducted a techno-economic evaluation on the thin-film condenser made of electrospun membranes and porous copper wicks. Thin-film condenser only adds less than 10% cost increase as compared to a conventional shell and tube condenser, but can enable power plants to generate 2-6% more power capacity, which is equivalent to a $13B value gain across all types of steam power plants in this world.

Although we demonstrated that the concept of thin-film condensation using commercially available materials is feasible, several challenges remain to be solved in order to apply this concept in an industrial scale setting. Perspectives, challenges, and future directions for the development of the thin-film condensers are presented here.

6.1 Customization of Porous Metal Wicks

Throughout the current study, we used commercially available copper foams as the porous wick layer for thin-film condensers. These copper foams came with limited options of thickness, pore size, permeability, and effective thermal conductivity. To further improve the performance of the thin-film condensers, the porous metal wick layer can be customized in a scalable way such as electrochemistry or sintering. For example[121], Figure 56 shows the SEM images of a group of copper foams with 3D interconnected pores obtained by electrodeposition.

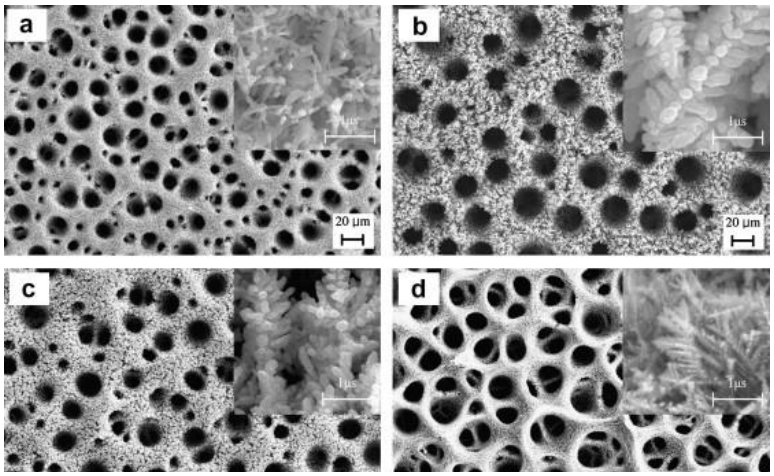

Figure 56: Electrodeposited copper foam with 3-dimensionally interconnected spherical pore network[121].

6.2 Bonding Between Porous Metal Wicks and Hydrophobic Membranes

Two major challenges remain in bonding the hydrophobic membranes to the porous metal wicks. First, the bonding needs to be strong enough to hold the membrane in place. On a tubular surface, this bonding could be strengthened by the self-limiting effect of the fibers. On a flat porous metal substrate, we noticed that the electrospun membrane could be easily peeled off after being directly electrospun onto the porous metal substrate. Our preliminary testing with heat treatment suggests that preheating and heating the porous metal substrate during the first few seconds of electrospinning could allow the electrospun polymer to melt onto the metal structures, which could then enable better bonding between the polymer-coated metal substrate and the upcoming electrospun fibers. We also noticed that the bonding between the porous metal wicks and the membrane layer varies with the geometry of the porous metal wicks. As shown in Figure 57, electrospun PVDF-HFP membrane was found to form stronger bonds with a 200 µm-pore-size copper foam than with a 100-mesh-size copper mesh after electrospinning on the heated substrate.

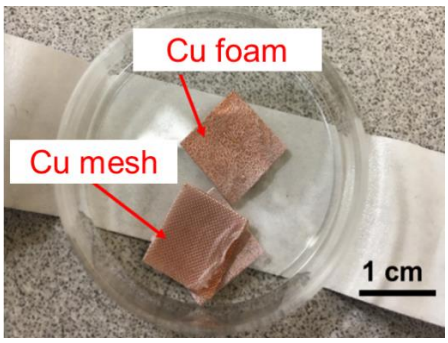

Figure 57: Electrospun PVDF-HFP membrane formed stronger bonds with a 200 µm-pore-size copper foam than with a 100-mesh-size copper mesh after electrospinning PVDF-HFP on a heated substrate.

Second challenge, as we have discussed in Chapter 4, is to form a uniformly thin electrospun membrane on a porous metal wick. Multi-needle electrospinning or electrospinning on a rotating/moving collector could potentially help with obtaining a membrane with uniform thickness on a porous metal. Alternatively, one can first fabricate a thin sheet of electrospun membrane before bonding it onto a porous metal wick, although bonding these two independent layers could be more challenging than directly electrospinning fibers on to a porous metal wick.

6.3 Design of Condensate Drainage Ports

When implementing thin-film condensation on a large-scale condenser tube, careful considerations need to be made about condensate drainage. Since the viscous pressure loss increases with the travel distance of the condensed water, it is important to design drainage ports along the length of the condenser tube to ensure that condensed water exits from drainage ports instead of bursting out of membrane pores.

Figure 58 shows two different condensate drainage designs for a thin-film condenser tube. Figure 58(a) shows the schematic of a thin-film condenser tube composed of a bottom layer of porous metal wick and a top layer of hydrophobic membrane with condensate drainage channel across the wick and the membrane at the bottom of the tube. With this design, condensed water needs to travel half of the perimeter of the tube to exit from the drainage channel at the bottom. Here, the continuous drainage channel at the bottom of the condenser tube may pose challenges for the bonding of the membrane on the wick layer. Figure 58(b) shows another design for the drainage ports, where the thin-film condenser tube is designed with microchannels for fast drainage and with spotted drainage pores located at the bottom of the each microchannel. The microchannels help direct the condensed water to exit from the designated exit ports on the bottom of the membrane layer. Here, the exit ports are designed as independent open ports throughout the membrane layer and located at the bottom of each microchannel rings. Having the exit ports as independent holes instead of a straight channel at the bottom of the condenser tube would allow the hydrophobic membrane to keep stronger attachment to the condenser tube during the condensation process.

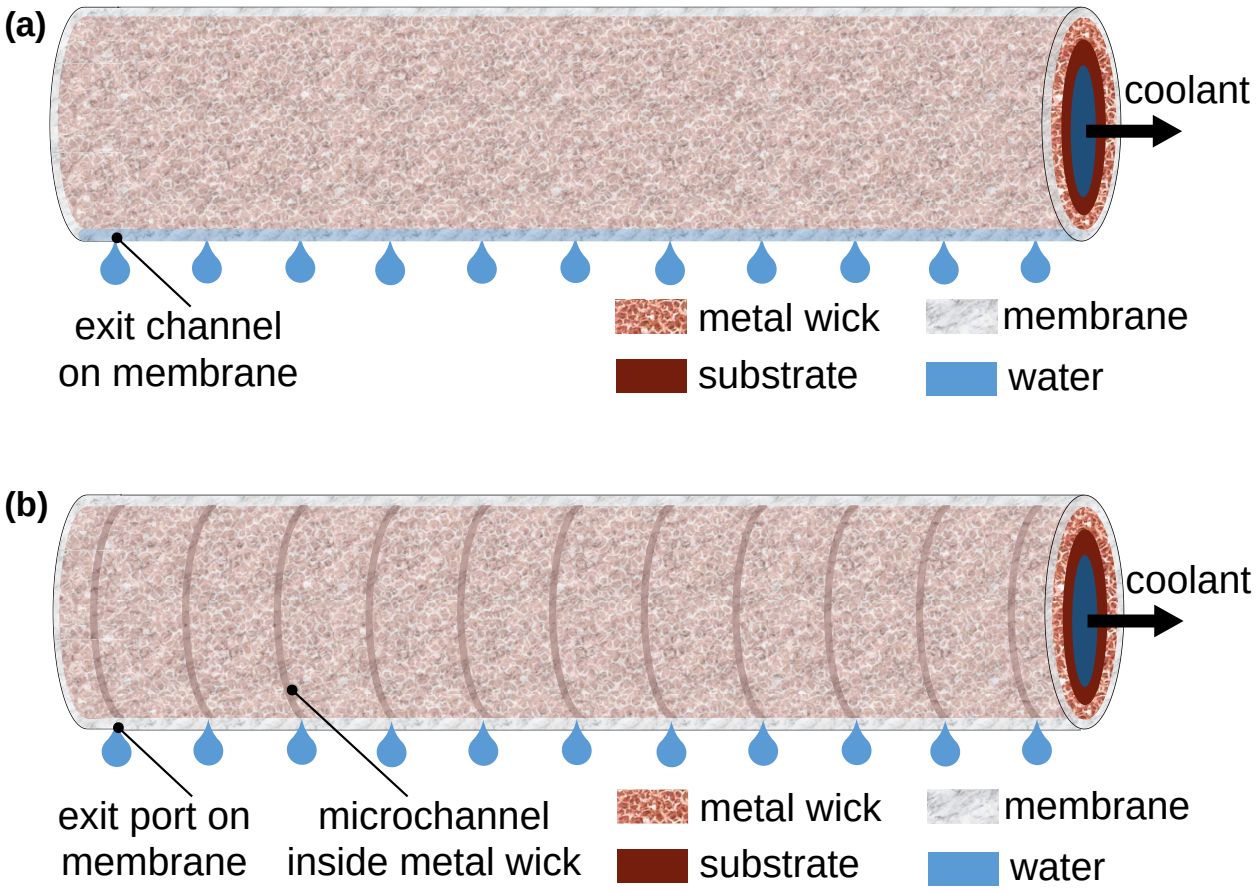

Figure 58: Schematics of two different condensate drainage designs for a thin-film condenser tube. (a) Thin-film condenser tube composed of a bottom layer of porous metal wick and a top layer of hydrophobic membrane with condensate drainage channel across the wick and the membrane at the bottom of the tube. (2) Thin-film condenser tube with microchannels for fast drainage and with spotted drainage pores located at the bottom of the each microchannel.

6.4 Other Challenges with Power Plant Condensers

In this thesis, we only focused on steam condensation and the impact of its enhancement to the energy efficiency of steam power plants. In reality, steam power plants are facing multiple challenges, such as low heat transfer efficiency, fouling or scaling caused by the cooling water, and corrosion of the condenser tubes. Depending on the operation condition of the power plant, enhancing the steam-side condensation may or may not be sufficient for improving the overall energy efficiency of the power plants. Strategies to overcome these other issues in addition to the application of thin-film condensation would allow steam power plants to achieve an even higher energy efficiency.

Bibliography

1 LaRose, S. N. A. International Energy Outlook 2021 (IEO2021). (Washington, DC, 2021).

2 Form EIA-923 Power Plant Operations Report. (2020).

3 Dieter, C. A. *et al.* Estimated use of water in the United States in 2015. Report No. 1441, 76 (Reston, VA, 2018).

4 Inventory of U.S. Greenhouse Gas Emissions and Sinkss: 1990-2020. (2022).

5 Grol, E. 2020 Water Technologies Project Review Meeting. (2020).

6 Schmidt, E., Schurig, W. & Sellschopp, W. Versuche über die Kondensation von Wasserdampf in Film- und Tropfenform. *Technische Mechanik und Thermodynamik* **1**, 53-63 (1930).

7 Rose, J. W. dropwise condensation theory and experiment: a review. *Proceedings of the Institution of Mechanical Engineering* **216**, 115-128 (2002).

8 Cho, H. J., Preston, D. J., Zhu, Y. & Wang, E. N. Nanoengineered materials for liquid–vapour phase-change heat transfer. *Nature Reviews Materials* **2**, 16092, doi:10.1038/natrevmats.2016.92 (2016).

9 Vemuri, S., Kim, K. J., Wood, B. D., Govindaraju, S. & Bell, T. W. Long term testing for dropwise condensation using self-assembled monolayer coatings of n-octadecyl mercaptan. *Applied Thermal Engineering* **26**, 421-429, doi:https://doi.org/10.1016/j.applthermaleng.2005.05.022 (2006).

10 Das, A. K., Kilty , H. P., Marto, P. J., Andeen, G. B. & Kumar, A. The Use of an Organic Self-Assembled Monolayer Coating to Promote Dropwise Condensation of Steam on Horizontal Tubes. *Journal of Heat Transfer* **122**, 278-286, doi:10.1115/1.521465 (1999).

11 Chen, L. *et al.* n-Octadecanethiol self-assembled monolayer coating with microscopic roughness for dropwise condensation of steam. *Journal of Thermal Science* **18**, 160-165, doi:10.1007/s11630-009-0160-z (2009).

12 Love, J. C., Estroff, L. A., Kriebel, J. K., Nuzzo, R. G. & Whitesides, G. M. Self-Assembled Monolayers of Thiolates on Metals as a Form of Nanotechnology. *Chemical Reviews* **105**, 1103-1170, doi:10.1021/cr0300789 (2005).

13 Tanner, D. W., Pope, D., Potter, C. J. & West, D. The promotion of dropwise condensation by monolayers of radioactive fatty acids I. Stearic acid on copper surfaces. *Journal of Applied Chemistry* **14**, 361-369, doi:https://doi.org/10.1002/jctb.5010140901 (1964).

14 Das, A., Kilty, H. P., Marto, P. J., Kumar, A. & Andeen, G. B. Dropwise Condensation of Steam on Horizontal Corrugated Tubes Using an Organic Self-Assembled Monolayer Coating. **7**, 109-123, doi:10.1615/JEnhHeatTransf.v7.i2.40 (2000).

15 Talesh Bahrami, H. R., Azizi, A. & Saffari, H. Influence of different parameters of preparing self-assembled monolayers on copper surfaces in the dropwise condensation heat transfer: an experimental study. *Journal of the Brazilian Society of Mechanical Sciences and Engineering* **41**, 1-11 (2019).

16 UÇAR, İ. O. & ERBİL, H. Y. Droplet condensation on polymer surfaces: A review. *Turkish Journal of Chemistry* **37**, 643-674 (2013).

17 Ma, X. *et al.* Influence of processing conditions of polymer film on dropwise condensation heat transfer. *International Journal of Heat and Mass Transfer* **45**, 3405-3411, doi:https://doi.org/10.1016/S0017-9310(02)00059-5 (2002).
18 Stylianou, S. A. & Rose, J. W. Dropwise Condensation on Surfaces Having Different Thermal Conductivities. *Journal of Heat Transfer* **102**, 477-482, doi:10.1115/1.3244326 (1980).
19 Nagle, W. u., Bays, G., Blenderman, L. & Drew, T. Heat-transfer coefficients during dropwise condensation of steam. *Trans. Am. Inst. Chem. Eng* **31**, 593-621 (1935).
20 Fitzpatrick, J., Baum, S. & McAdams, W. Dropwise condensation of steam on vertical tubes. *Trans. AIChE* **35**, 97-107 (1939).
21 Le Fevre, E. & Rose, J. Heat-transfer measurements during dropwise condensation of steam. *International Journal of Heat and Mass Transfer* **7**, 272-273 (1964).
22 Le Fevre, E. J. & Rose, J. W. An experimental study of heat transfer by dropwise condensation. *International Journal of Heat and Mass Transfer* **8**, 1117-1133, doi:https://doi.org/10.1016/0017-9310(65)90139-0 (1965).
23 Wang, R., Jakhar, K., Ahmed, S. & Antao, D. S. Elucidating the Mechanism of Condensation-Mediated Degradation of Organofunctional Silane Self-Assembled Monolayer Coatings. *ACS Applied Materials & Interfaces* **13**, 34923-34934, doi:10.1021/acsami.1c08496 (2021).
24 El Fil, B., Kini, G. & Garimella, S. A review of dropwise condensation: Theory, modeling, experiments, and applications. *International Journal of Heat and Mass Transfer* **160**, 120172, doi:https://doi.org/10.1016/j.ijheatmasstransfer.2020.120172 (2020).
25 Goswami, A., Pillai, S. C. & McGranaghan, G. Surface modifications to enhance dropwise condensation. *Surfaces and Interfaces* **25**, 101143, doi:https://doi.org/10.1016/j.surfin.2021.101143 (2021).
26 Ahlers, M., Buck-Emden, A. & Bart, H.-J. Is dropwise condensation feasible? A review on surface modifications for continuous dropwise condensation and a profitability analysis. *Journal of Advanced Research* **16**, 1-13, doi:https://doi.org/10.1016/j.jare.2018.11.004 (2019).
27 Bonner III, R. W. in *International Heat Transfer Conference.* 221-226.
28 Tang, Y., Yang, X., Li, Y., Lu, Y. & Zhu, D. Robust Micro-Nanostructured Superhydrophobic Surfaces for Long-Term Dropwise Condensation. *Nano Letters* **21**, 9824-9833, doi:10.1021/acs.nanolett.1c01584 (2021).
29 Ho, J. Y. *et al.* Ultrascalable Surface Structuring Strategy of Metal Additively Manufactured Materials for Enhanced Condensation. *Advanced Science* **n/a**, 2104454, doi:https://doi.org/10.1002/advs.202104454.
30 Lee, J. & Won, Y. Enhancing Recurrent Droplet Jumping Phenomena on Heterogeneous Surface Designs. *Advanced Materials Interfaces* **n/a**, 2200573, doi:https://doi.org/10.1002/admi.202200573.
31 Yan, X. *et al.* Hierarchical Condensation. *ACS Nano* **13**, 8169-8184, doi:10.1021/acsnano.9b03275 (2019).
32 Miljkovic, N. *et al.* Jumping-Droplet-Enhanced Condensation on Scalable Superhydrophobic Nanostructured Surfaces. *Nano Letters* **13**, 179-187, doi:10.1021/nl303835d (2013).

33 Chu, F., Yan, X. & Miljkovic, N. How Superhydrophobic Grooves Drive Single-Droplet Jumping. *Langmuir* **38**, 4452-4460, doi:10.1021/acs.langmuir.2c00373 (2022).
34 Miljkovic, N., Preston, D. J., Enright, R. & Wang, E. N. Electric-Field-Enhanced Condensation on Superhydrophobic Nanostructured Surfaces. *ACS Nano* **7**, 11043-11054, doi:10.1021/nn404707j (2013).
35 Youhua, J. Droplet depinning on superhydrophobic surfaces: from simple rigid wetting to complex soft wetting. *Surface Innovations* **0**, 1-6, doi:10.1680/jsuin.22.01010.
36 Seo, D. *et al.* Passive Anti-Flooding Superhydrophobic Surfaces. *ACS Applied Materials & Interfaces* **12**, 4068-4080, doi:10.1021/acsami.9b17943 (2020).
37 Ölçeroğlu, E. & McCarthy, M. Self-Organization of Microscale Condensate for Delayed Flooding of Nanostructured Superhydrophobic Surfaces. *ACS Applied Materials & Interfaces* **8**, 5729-5736, doi:10.1021/acsami.6b00852 (2016).
38 Ji, D.-Y., Lee, J.-W., Hwang, W. & Lee, K.-Y. Experimental study of condensation heat transfer on a horizontal aluminum tube with superhydrophobic characteristic. *International Journal of Heat and Mass Transfer* **134**, 286-295, doi:https://doi.org/10.1016/j.ijheatmasstransfer.2019.01.040 (2019).
39 Wang, R., Guo, J., Muckleroy, E. A. & Antao, D. S. Robust silane self-assembled monolayer coatings on plasma-engineered copper surfaces promoting dropwise condensation. *International Journal of Heat and Mass Transfer* **194**, 123028, doi:https://doi.org/10.1016/j.ijheatmasstransfer.2022.123028 (2022).
40 Paxson, A. T., Yagüe, J. L., Gleason, K. K. & Varanasi, K. K. Stable Dropwise Condensation for Enhancing Heat Transfer via the Initiated Chemical Vapor Deposition (iCVD) of Grafted Polymer Films. *Advanced materials* **26**, 418-423, doi:https://doi.org/10.1002/adma.201303065 (2014).
41 Ma, J. *et al.* A Lipid-Inspired Highly Adhesive Interface for Durable Superhydrophobicity in Wet Environments and Stable Jumping Droplet Condensation. *ACS Nano* **16**, 4251-4262, doi:10.1021/acsnano.1c10250 (2022).
42 Bayani Ahangar, S., Lee, K.-B. & Choi, C. K. Dropwise Condensation Mechanism on Smooth Hydrophilic Surfaces. *Applied sciences* **11**, 9184, doi:10.3390/app11199184 (2021).
43 Cha, H. *et al.* Dropwise condensation on solid hydrophilic surfaces. *Science Advances* **6**, eaax0746, doi:doi:10.1126/sciadv.aax0746 (2020).
44 Tuteja, A. *et al.* Designing Superoleophobic Surfaces. *Science* **318**, 1618-1622, doi:doi:10.1126/science.1148326 (2007).
45 Han, Z., Tay, B., Tan, C., Shakerzadeh, M. & Ostrikov, K. Electrowetting Control of Cassie-to-Wenzel Transitions in Superhydrophobic Carbon Nanotube-Based Nanocomposites. *ACS Nano* **3**, 3031-3036, doi:10.1021/nn900846p (2009).
46 Lee, S. E., Kim, H.-J., Lee, S.-H. & Choi, D.-G. Superamphiphobic Surface by Nanotransfer Molding and Isotropic Etching. *Langmuir* **29**, 8070-8075, doi:10.1021/la4011086 (2013).
47 Liu, T. L. & Kim, C.-J. C. Turning a surface superrepellent even to completely wetting liquids. *Science* **346**, 1096-1100, doi:doi:10.1126/science.1254787 (2014).
48 Domingues, E. M., Arunachalam, S., Nauruzbayeva, J. & Mishra, H. Biomimetic coating-free surfaces for long-term entrapment of air under wetting liquids. *Nature Communications* **9**, 3606, doi:10.1038/s41467-018-05895-x (2018).

49 Arunachalam, S., Das, R., Nauruzbayeva, J., Domingues, E. M. & Mishra, H. Assessing omniphobicity by immersion. *Journal of Colloid and Interface Science* **534**, 156-162, doi:https://doi.org/10.1016/j.jcis.2018.08.059 (2019).
50 Yao, X. *et al.* Omniphobic ZIF-8@Hydrogel Membrane by Microfluidic-Emulsion-Templating Method for Wound Healing. *Advanced Functional Materials* **30**, 1909389, doi:https://doi.org/10.1002/adfm.201909389 (2020).
51 Zhang, L. *et al.* Nucleation Site Distribution Probed by Phase-Enhanced Environmental Scanning Electron Microscopy. *Cell Reports Physical Science* **1**, 100262, doi:https://doi.org/10.1016/j.xcrp.2020.100262 (2020).
52 Enright, R., Miljkovic, N., Al-Obeidi, A., Thompson, C. V. & Wang, E. N. Condensation on Superhydrophobic Surfaces: The Role of Local Energy Barriers and Structure Length Scale. *Langmuir* **28**, 14424-14432, doi:10.1021/la302599n (2012).
53 Wilke, K. L., Preston, D. J., Lu, Z. & Wang, E. N. Toward Condensation-Resistant Omniphobic Surfaces. *ACS Nano* **12**, 11013-11021, doi:10.1021/acsnano.8b05099 (2018).
54 Wong, T.-S. *et al.* Bioinspired self-repairing slippery surfaces with pressure-stable omniphobicity. *Nature* **477**, 443-447, doi:10.1038/nature10447 (2011).
55 Villegas, M., Zhang, Y., Abu Jarad, N., Soleymani, L. & Didar, T. F. Liquid-Infused Surfaces: A Review of Theory, Design, and Applications. *ACS Nano* **13**, 8517-8536, doi:10.1021/acsnano.9b04129 (2019).
56 Weisensee, P. B. *et al.* Condensate droplet size distribution on lubricant-infused surfaces. *International Journal of Heat and Mass Transfer* **109**, 187-199, doi:https://doi.org/10.1016/j.ijheatmasstransfer.2017.01.119 (2017).
57 Sun, J. & Weisensee, P. B. Microdroplet self-propulsion during dropwise condensation on lubricant-infused surfaces. *Soft Matter* **15**, 4808-4817, doi:10.1039/C9SM00493A (2019).
58 Park, K.-C. *et al.* Condensation on slippery asymmetric bumps. *Nature* **531**, 78-82, doi:10.1038/nature16956 (2016).
59 Preston, D. J., Song, Y., Lu, Z., Antao, D. S. & Wang, E. N. Design of Lubricant Infused Surfaces. *ACS Applied Materials & Interfaces* **9**, 42383-42392, doi:10.1021/acsami.7b14311 (2017).
60 Xiao, R., Miljkovic, N., Enright, R. & Wang, E. N. Immersion Condensation on Oil-Infused Heterogeneous Surfaces for Enhanced Heat Transfer. *Scientific Reports* **3**, 1988, doi:10.1038/srep01988 (2013).
61 NyeokKim, H. & JoonLee, S. Shear-driven drainage of lubricant in a spherical cavity of lubricant-infused surface. *Physics of Fluids* **33**, 122011, doi:10.1063/5.0074107 (2021).
62 Baumli, P. *et al.* The challenge of lubricant-replenishment on lubricant-impregnated surfaces. *Advances in Colloid and Interface Science* **287**, 102329, doi:https://doi.org/10.1016/j.cis.2020.102329 (2021).
63 Laney, S. K. *et al.* Delayed Lubricant Depletion of Slippery Liquid Infused Porous Surfaces Using Precision Nanostructures. *Langmuir* **37**, 10071-10078, doi:10.1021/acs.langmuir.1c01310 (2021).
64 Adera, S. *et al.* Depletion of Lubricant from Nanostructured Oil-Infused Surfaces by Pendant Condensate Droplets. *ACS Nano* **14**, 8024-8035, doi:10.1021/acsnano.9b10184 (2020).

65 Wexler, J. S., Jacobi, I. & Stone, H. A. Shear-Driven Failure of Liquid-Infused Surfaces. *Physical Review Letters* **114**, 168301, doi:10.1103/PhysRevLett.114.168301 (2015).
66 Peppou-Chapman, S. & Neto, C. Mapping Depletion of Lubricant Films on Antibiofouling Wrinkled Slippery Surfaces. *ACS Applied Materials & Interfaces* **10**, 33669-33677, doi:10.1021/acsami.8b11768 (2018).
67 Wilke, K. L. *et al.* Polymer Infused Porous Surfaces for Robust, Thermally Conductive, Self-Healing Coatings for Dropwise Condensation. *ACS Nano* **14**, 14878-14886, doi:10.1021/acsnano.0c03961 (2020).
68 Zhang, W., Fan, S., Wang, Y., Lang, X. & Li, G. Development of a composite structured surface for durable anti-hydrate and enhancing thermal conductivity. *International Journal of Heat and Mass Transfer* **192**, 122909, doi:https://doi.org/10.1016/j.ijheatmasstransfer.2022.122909 (2022).
69 Chang, H. C. *et al.* Composite Structured Surfaces for Durable Dropwise Condensation. *International Journal of Heat and Mass Transfer* **156**, 119890, doi:https://doi.org/10.1016/j.ijheatmasstransfer.2020.119890 (2020).
70 Preston, D. J. *et al.* Gravitationally Driven Wicking for Enhanced Condensation Heat Transfer. *Langmuir* **34**, 4658-4664, doi:10.1021/acs.langmuir.7b04203 (2018).
71 Renken, K. J. & Mueller, C. D. Measurements of enhanced film condensation utilizing a porous metallic coating. *Journal of Thermophysics and Heat Transfer* **7**, 148-152, doi:10.2514/3.11582 (1993).
72 Wang, R. & Antao, D. S. Capillary-Enhanced Filmwise Condensation in Porous Media. *Langmuir* **34**, 13855-13863, doi:10.1021/acs.langmuir.8b02611 (2018).
73 Wen, R. *et al.* Sustaining enhanced condensation on hierarchical mesh-covered surfaces. *National Science Review* **2018 v.5 no.6**, pp. 878-887, doi:10.1093/nsr/nwy098 (2018).
74 Oh, J. *et al.* Thin Film Condensation on Nanostructured Surfaces. *Advanced Functional Materials* **28**, 1707000, doi:https://doi.org/10.1002/adfm.201707000 (2018).
75 Ölçeroğlu, E., Hsieh, C.-Y., Lau, K. K. S. & McCarthy, M. Thin Film Condensation Supported on Ambiphilic Microstructures. *Journal of Heat Transfer* **139**, doi:10.1115/1.4035580 (2017).
76 Liu, K. *et al.* Self-Cleaning Porous Surfaces for Dry Condensation. *ACS Applied Materials & Interfaces* **10**, 26759-26764, doi:10.1021/acsami.8b07261 (2018).
77 Warsinger, D. M. *et al.* A review of polymeric membranes and processes for potable water reuse. *Prog Polym Sci* **81**, 209-237, doi:10.1016/j.progpolymsci.2018.01.004 (2016).
78 Lalia, B. S., Guillen-Burrieza, E., Arafat, H. A. & Hashaikeh, R. Fabrication and characterization of polyvinylidenefluoride-co-hexafluoropropylene (PVDF-HFP) electrospun membranes for direct contact membrane distillation. *Journal of Membrane Science* **428**, 104-115, doi:10.1016/j.memsci.2012.10.061 (2013).
79 Boo, C., Lee, J. & Elimelech, M. Omniphobic Polyvinylidene Fluoride (PVDF) Membrane for Desalination of Shale Gas Produced Water by Membrane Distillation. *Environmental Science & Technology* **50**, 12275-12282, doi:10.1021/acs.est.6b03882 (2016).
80 Camacho, L. M. *et al.* Advances in Membrane Distillation for Water Desalination and Purification Applications. *Water* **5**, doi:10.3390/w5010094 (2013).

81 Feng, S., Zhong, Z., Wang, Y., Xing, W. & Drioli, E. Progress and perspectives in PTFE membrane: Preparation, modification, and applications. *Journal of Membrane Science* **549**, 332-349, doi:https://doi.org/10.1016/j.memsci.2017.12.032 (2018).
82 *https://www.wieland-thermalsolutions.com/en/products/finned-tubes/enhanced-surface-tubes*.
83 Mochizuki, M. *et al.* A REVIEW OF HEAT PIPE APPLICATION INCLUDING NEW OPPORTUNITIES. *Frontiers in Heat Pipes* **2** (2011).
84 Lee, H. *Thermal design heat sinks, thermoelectrics, heat pipes, compact heat exchangers, and solar cells*. (Wiley, 2010).
85 Leong, K. C., Liu, C. Y. & Lu, G. Q. Characterization of Sintered Copper Wicks Used in Heat Pipes. *Journal of Porous Materials* **4**, 303-308, doi:10.1023/A:1009685508557 (1997).
86 Summers, E. K., Arafat, H. A. & Lienhard, J. H. Energy efficiency comparison of single-stage membrane distillation (MD) desalination cycles in different configurations. *Desalination* **290**, 54-66, doi:10.1016/j.desal.2012.01.004 (2012).
87 S P Sutera, a. & Skalak, R. The History of Poiseuille's Law. *Annual Review of Fluid Mechanics* **25**, 1-20, doi:10.1146/annurev.fl.25.010193.000245 (1993).
88 Schofield, R. W., Fane, A. G. & Fell, C. J. D. Gas and vapour transport through microporous membranes. I. Knudsen-Poiseuille transition. *Journal of Membrane Science* **53**, 159-171, doi:https://doi.org/10.1016/0376-7388(90)80011-A (1990).
89 Kara, V., Yakhot, V. & Ekinci, K. L. Generalized Knudsen Number for Unsteady Fluid Flow. *Physical review letters* **118**, 074505-074505, doi:10.1103/PhysRevLett.118.074505 (2017).
90 Mason, E. A. M. A. P. Gas transport in porous media : the dusty-gas model. (1983).
91 Zhao, Y. & Wang, J. Exergoeconomic analysis and optimization of a flash-binary geothermal power system. *Applied Energy* **179**, 159-170, doi:https://doi.org/10.1016/j.apenergy.2016.06.108 (2016).
92 Roy, R., Ratisher, M. & Gokhale, V. A computational model of a power plant steam condenser. *J. Energy Resour. Technol.* **123**, 81-91 (2001).
93 Martínez, L., Florido-Díaz, F. J., Hernández, A. & Prádanos, P. Characterisation of three hydrophobic porous membranes used in membrane distillation: Modelling and evaluation of their water vapour permeabilities. *Journal of Membrane Science* **203**, 15-27, doi:https://doi.org/10.1016/S0376-7388(01)00719-0 (2002).
94 Whitaker, S. Flow in porous media I: A theoretical derivation of Darcy's law. *Transport in Porous Media* **1**, 3-25, doi:10.1007/BF01036523 (1986).
95 Vanneste, J. *et al.* Novel thermal efficiency-based model for determination of thermal conductivity of membrane distillation membranes. *Journal of Membrane Science* **548**, 298-308, doi:https://doi.org/10.1016/j.memsci.2017.11.028 (2018).
96 Jacobi, X.-H. H. Q. W. Y.-G. P. C. T. J. U. A. S. A. A review of metal foam and metal matrix composites for heat exchangers and heat Sinks. *HEAT TRANSFER ENGINEERING.* **33**, 991-1009 (2012).
97 Li, C. & Peterson, G. P. The effective thermal conductivity of wire screen. *International Journal of Heat and Mass Transfer* **49**, 4095-4105, doi:https://doi.org/10.1016/j.ijheatmasstransfer.2006.03.031 (2006).

98 Chavan, S. *et al.* Heat Transfer through a Condensate Droplet on Hydrophobic and Nanostructured Superhydrophobic Surfaces. *Langmuir* **32**, 7774-7787, doi:10.1021/acs.langmuir.6b01903 (2016).
99 Parker, W. J., Jenkins, R. J., Butler, C. P. & Abbott, G. L. Flash Method of Determining Thermal Diffusivity, Heat Capacity, and Thermal Conductivity. *Journal of Applied Physics* **32**, 1679-1684, doi:10.1063/1.1728417 (1961).
100 Leroy, A., Bhatia, B., Sircar, J. & Wang, E. N. Thermal transport in solar-reflecting and infrared-transparent polyethylene aerogels. *International Journal of Heat and Mass Transfer* **184**, 122307, doi:https://doi.org/10.1016/j.ijheatmasstransfer.2021.122307 (2022).
101 Singh, B. S., Dybbs, A. & Lyman, F. A. Experimental study of the effective thermal conductivity of liquid saturated sintered fiber metal wicks. *International Journal of Heat and Mass Transfer* **16**, 145-155, doi:https://doi.org/10.1016/0017-9310(73)90258-5 (1973).
102 Koh, J. C. Y. & Fortini, A. Prediction of thermal conductivity and electrical resistivity of porous metallic materials. *International Journal of Heat and Mass Transfer* **16**, 2013-2022, doi:https://doi.org/10.1016/0017-9310(73)90104-X (1973).
103 Reay, D., Kew, P. & McGlen, R. Heat Pipes: Theory, Design and Applications: Sixth Edition. *Heat Pipes: Theory, Design and Applications: Sixth Edition*, 1-251 (2013).
104 Bodla, K. K., Murthy, J. Y. & Garimella, S. V. Direct Simulation of Thermal Transport Through Sintered Wick Microstructures. *Journal of Heat Transfer* **134**, doi:10.1115/1.4004804 (2011).
105 Carson, J. K., Lovatt, S. J., Tanner, D. J. & Cleland, A. C. Thermal conductivity bounds for isotropic, porous materials. *International Journal of Heat and Mass Transfer* **48**, 2150-2158, doi:https://doi.org/10.1016/j.ijheatmasstransfer.2004.12.032 (2005).
106 Sudhakar, S., Weibel, J. A. & Garimella, S. V. A semi-empirical model for thermal resistance and dryout during boiling in thin porous evaporators fed by capillary action. *International Journal of Heat and Mass Transfer* **181**, 121887, doi:https://doi.org/10.1016/j.ijheatmasstransfer.2021.121887 (2021).
107 Minkowycz, W. J. & Sparrow, E. M. Condensation heat transfer in the presence of noncondensables, interfacial resistance, superheating, variable properties, and diffusion. *Int. J. Heat Mass Transfer* **9**, 1125-1144 (1966).
108 Zhao, Y. *et al.* Effects of millimetric geometric features on dropwise condensation under different vapor conditions. *International Journal of Heat and Mass Transfer* **119**, 931-938, doi:https://doi.org/10.1016/j.ijheatmasstransfer.2017.11.139 (2018).
109 Preston, D. J. *et al.* Effect of hydrocarbon adsorption on the wettability of rare earth oxide ceramics. *Applied Physics Letters* **105**, 011601, doi:10.1063/1.4886410 (2014).
110 Varanasi, K. K., Hsu, M., Bhate, N., Yang, W. & Deng, T. Spatial control in the heterogeneous nucleation of water. *Applied Physics Letters* **95**, 094101, doi:10.1063/1.3200951 (2009).
111 Li, K., Hou, D., Fu, C., Wang, K. & Wang, J. Fabrication of PVDF nanofibrous hydrophobic composite membranes reinforced with fabric substrates via electrospinning for membrane distillation desalination. *Journal of Environmental Sciences* **75**, 277-288, doi:https://doi.org/10.1016/j.jes.2018.04.002 (2019).

112 Song, C. & Rutledge, G. C. Electrospun Liquid-Infused Membranes for Emulsified Oil/Water Separation. *Langmuir* **38**, 2301-2313, doi:10.1021/acs.langmuir.1c03016 (2022).
113 Gopal, R. *et al.* Electrospun nanofibrous filtration membrane. *Journal of Membrane Science* **281**, 581-586, doi:https://doi.org/10.1016/j.memsci.2006.04.026 (2006).
114 Li, X. *et al.* Electrospinning-Based Strategies for Battery Materials. *Advanced Energy Materials* **11**, 2000845, doi:https://doi.org/10.1002/aenm.202000845 (2021).
115 Agarwal, S., Wendorff, J. H. & Greiner, A. Use of electrospinning technique for biomedical applications. *Polymer* **49**, 5603-5621, doi:https://doi.org/10.1016/j.polymer.2008.09.014 (2008).
116 Ura, D. P. *et al.* Surface Potential Driven Water Harvesting from Fog. *ACS Nano* **15**, 8848-8859, doi:10.1021/acsnano.1c01437 (2021).
117 Ahmed, F. E., Lalia, B. S. & Hashaikeh, R. A review on electrospinning for membrane fabrication: Challenges and applications. *Desalination* **356**, 15-30, doi:https://doi.org/10.1016/j.desal.2014.09.033 (2015).
118 Berling, T. & Runeson, P. Efficient evaluation of multifactor dependent system performance using fractional factorial design. *IEEE Transactions on Software Engineering* **29**, 769-781, doi:10.1109/TSE.2003.1232283 (2003).
119 *https://atb.nrel.gov/*.
120 https://www.powermag.com/enhanced-condenser-tube-designs-improve-plant-performance/.
121 Kim, J.-H., Kim, R.-H. & Kwon, H.-S. Preparation of copper foam with 3-dimensionally interconnected spherical pore network by electrodeposition. *Electrochemistry Communications* **10**, 1148-1151, doi:https://doi.org/10.1016/j.elecom.2008.05.035 (2008).